COMPUTATIONAL AEROACOUSTIC-STRUCTURAL INTERACTION IN INTERNAL FLOW WITH CE/SE METHOD

FAN KA HENG

PhD

The Hong Kong Polytechnic University

2018

The Hong Kong Polytechnic University

Department of Mechanical Engineering

Computational Aeroacoustic-Structural Interaction in Internal Flow with CE/SE Method

FAN Ka Heng

A thesis submitted in partial fulfilment of the requirements for the degree of Doctor of Philosophy

August 2017

CERTIFICATE OF ORIGINALITY

I hereby declare that this thesis is my own work and that, to the best of my knowledge and belief, it reproduces no material previously published or written, nor material that has been accepted for the award of any other degree or diploma, except where due acknowledgement has been made in the text.

_____

FAN Ka Heng

Abstract

In many engineering applications, such as ventilation systems and aircraft bodies, flexible thin structures in contact with the unsteady flow are used. Acoustic radiation will be generated if the structural vibration is excited by flow disturbances or acoustic waves. It can propagate back and in turn modify the flow process or vibration that generated it. Such kinds of problem involve a complex interaction between acoustics, flow and structural dynamics, known as aeroacoustic-structural interaction, and it is a major consideration in engineering design. Therefore, accurate prediction of the interaction is an important task. Motivated by the needs for better understanding of the aeroacoustic-structural interaction in advance silencer design, an effective yet accurate numerical methodology has been developed to study the interaction in both inviscid and viscous internal flows. Two fluid-structure coupling approaches are presented and validated theoretically and experimentally for different problems in this thesis.

The partitioned approach is used for the inviscid problem due to its satisfactory accuracy and flexibility in development. The aeroacoustic model is governed by the two-dimensional compressible Euler equations together with equation of state and solved by a direct aeroacoustic simulation solver based on the conservation element and solution element (CE/SE) method. The panel dynamic model is governed by the nonlinear one-dimension plate equation and solved by standard finite-difference procedure with an iterative coupling scheme to achieve

the communication between two media. The numerical methodology is validated with a theoretical study of a single frequency grazing incident acoustic excited flexible panel vibration problem in a duct. The acoustic and structural responses are discussed in detail. To study the effect of a mean flow, a uniform flow is introduced to the duct. A subsonic flow results in the suppression of transmission loss significantly. Higher-order modes and oblique shock waves emerge in the sonic and the supersonic flow. Besides, the bimodal pattern of panel response is observed that incompressible theory is not able to predict. The phase speed of both upstream and downstream travelling bending wave are changed by the effect of fluid inertia. The subsonic and supersonic panel responses and nearfield fluid response with broadband excitation are observed and discussed.

The monolithic approach is applied for the viscous problem because of the failure of the partitioned one in a flow-induced structural instability problem. The governing equations of both fluid (Navier-Stokes equations) and flexible panel are combined and solved through the Newton iteration procedure. It shows higher accuracy and better time efficiency than the partitioned approach. The numerical methodology is validated with two experimental studies on a broadband grazing incident acoustic excited flexible panel with a low subsonic flow problem and a grazing flow-induced structural instability problem. Both aeroacoustic and structural responses are captured correctly by the numerical methodology in these two cases. The importance of including the viscous effect is demonstrated. The effect of cavities is also discussed. In the acoustic-induced vibration problem, it can amplify and attenuate the upstream and downstream travelling bending waves and changes the effective silencing frequency range. In the flow-induced vibration problem, it is independent of the occurrence of structural instability but can modify the dominant vibration mode and the amount of energy radiation and induce higher fluid inertia loading.

Publications Arising from the Thesis

Some ideas and figures have appeared previously in the following publications.

Book chapters

Fan, H. K. H., Lam, G. C. Y., and Leung, R. C. K. (2019), "Numerical Study of Nonlinear Fluid-Structure Interaction of an Excited Panel in Viscous Flow," *Flinovia—Flow Induced Noise and Vibration Issues and Aspects-II: A Focus on Measurement, Modeling, Simulation and Reproduction of the Flow Excitation and Flow Induced Response*, Springer, Cham, pp. 253–269.

Leung, R. C. K., Fan, H. K. H., and Lam, G. C. Y. (2015), "A Numerical Methodology for Resolving Aeroacoustic-Structural Response of Flexible Panel," *Flinovia - Flow Induced Noise and Vibration Issues and Aspects: A Focus on Measurement, Modeling, Simulation and Reproduction of the Flow Excitation and Flow Induced Response*, Springer, Cham, Heidelberg, New York, Dordrecht, London, pp. 321–342.

Journal articles

Fan, H. K. H., Leung, R. C. K., and Lam, G. C. Y. (2015), "Numerical Analysis of Aeroacoustic-Structural Interaction of a Flexible Panel in Uniform Duct Flow," *Journal of the Acoustical Society of America*, Vol. 137, No. 6, pp. 3115–3126.

Fan, H. K. H., Leung, R. C. K., Lam, G. C. Y., Aurégan, Y., and Dai, X. (2018), "Coupling Strategy for Resolving In-duct Elastic Panel Aeroacoustic-Structural Interaction with CE/SE Method," *AIAA Journal* (accepted).

Conference proceedings

Fan, H. K. H. and Leung, R. C. K. (2015), "Aeroacoustic-Structural Interaction of Cavity-Backed Flexible Duct Segment Carrying a Low Speed Flow," *The 12th International Conference on Theoretical and Computational Acoustics*, Hangzhou, Zhejiang, China, Paper No. ICTCA2015-1315.

Fan, H. K. H., Leung, R. C. K., and Lam, G. C. Y. (2013), "A Time-Domain Analysis for Aeroacoustics-Structure Interaction of Flexible Panel," *19th AIAA/CEAS Aeroacoustics Conference*, Berlin, Germany, Paper No. AIAA 2013-2133.

Fan, H. K. H., Leung, R. C. K., Lam, G. C. Y., and Li, K. H. (2014), "Acoustic-Structural Interaction of Flexible Walls in a Flow Duct," *The 21st International Congress on Sound and Vibration*, Beijing, China, Paper No. 917.

Fan, H. K. H., Li, K. H., Leung, R. C. K., and Lam, G. C. Y. (2015), "A Study of the Aeroacoustic-Structural Responses of a Flexible Duct Segment Exposed to Broadband Excitation," *The 22nd International Congress on Sound and Vibration*, Florence, Italy, Paper No. 475.

Shen, C., Fan, H. K. H., and Leung, R. C. K. (2017), "Duct Flow Noise Control by

Excited Vibrating Membranes," *The 17th Asian Pacific Vibration Conference*, Nanjing, China, Paper No. 024.

Acknowledgements

I would like to express my gratitude to my supervisor, Dr Randolph Chi Kin Leung, for his continued inspiration, patient guidance and tough training. Indeed the incredible experience under his supervision is very beneficial to my academic life.

I also greatly appreciated my research colleagues, Dr Garret Chi Yan Lam, Dr Ka Him Seid, Mr Horus Yui Ho Chan and other members in our research team, Computational Aeroacoustic-Structural Interaction Laboratory, for their academic advisement, technical support, encouragement and friendship. I have benefited greatly from the cooperation and daily conversations with them.

Besides, I would like to acknowledge my family for their love and supports, especially my mother who take care my daily life. Without their supports, this thesis would not have been possible.

Last but not least, I gratefully acknowledge the stipend given by the Department of Mechanical Engineering, the Hong Kong Polytechnic University through funding support from Research Grants Council of HKSAR Government under Grant Nos. PolyU 5230/09E and PolyU 5199/11E.

Contents

Abstract ii

Publications Arising from the Thesis iv

Acknowledgements vii

List of Figures xi

List of Tables xvii

Abbreviations xviii

Nomenclature xix

1 Introduction 1

1.1 Literature survey 3

1.1.1 Interaction of flow and structure 3

1.1.2 Interaction of acoustics and structure 6

1.1.3 Aeroacoustic-structural interaction 8

1.2 Fluid-structure coupling 10

1.2.1 Partitioned approach 11

1.2.2 Monolithic approach 13

1.3 Research scopes 14

1.4 Outline 15

2 Physical Models and Numerical Methods 17

2.1 Aeroacoustic model 18

2.1.1 The conservation element and solution element method . . 20

2.2 Panel dynamic model 24

2.3 Boundary conditions 27

2.3.1 Fluid domain 27

2.3.2 Flexible panel 32

2.4 Partitioned fluid-panel coupling scheme 34

2.4.1 Staggered coupling scheme 34

2.4.2 Iterative coupling scheme 35

2.5 Validation for in-vacuo and fluid loaded panel vibration 36

3 Aeroacoustic-Structural Interaction in Duct Carrying Inviscid Flow 42

3.1 Single frequency excitation 42

3.1.1 Acoustic-structural interaction 42

3.1.2 Aeroacoustic-structural interaction 58

3.2 Broadband excitation 71

3.2.1 Dispersion characteristic of structural response 73

3.2.2 Near field fluid response 77

4 Formulation and Numerical Methods for Viscous Problem 81

4.1 Problem of the partitioned approach 81

4.2 Monolithic approach 83

4.2.1 Coupled fluid-panel equation 84

4.2.2 Solution strategy for the inhomogeneous equation and discretization 87

4.2.3 Boundary conditions 96

4.3 Comparisons of partitioned and monolithic approaches 97

5 Aeroacoustic-Structural Interaction in Duct Carrying Viscous Flow 100

5.1 Aeroacoustic-structural interaction 100

5.1.1 Summary of the experiment 101

5.1.2 Validation of the methodology 102

5.1.3 Aeroacoustic-structural response 110

5.2 Flow-induced structural instability 114

5.2.1 Summary of the experiment 114

5.2.2 Validation of the methodology 115

5.2.3 Aeroacoustic-structural response 122

6 Conclusions 132

6.1 Limitations and future works 135

References 139

List of Figures

1.1 Ventilation ducts commonly found in Hong Kong. 15

2.1 Triangulate grids in a computational domain. ∘ : A, C, E and G are the centroids of the grids; B, D and F are the nodes; × : G* is a solution point; and − − − is the boundary of a CE. 21

2.2 Geometrical definitions of $CE(\mathrm{G}^*, j)$. − − − is the boundary of $SE(\mathrm{G}^*, j)$. 22

2.3 Geometrical definitions of $SE(\mathrm{G}^*, j)$. 23

2.4 Free-body diagram of a small deflected flexible panel segment. . . 25

2.5 Meshes at fluid-panel interface. −·−·−, undeflected panel position; □, solution points of boundary cells and ghost cells of CE/SE mesh; ◯, panel mesh points. 29

2.6 Boundary segment of undeflected panel. ×, mesh nodes; ○, solution points; ●, a ghost point; ——, the panel segment. 32

2.7 Calculation procedure of the staggered coupling scheme (or initial estimation procedure of the iterative coupling scheme). AAM, aeroacoustical model; SDM, structural dynamic model. 34

2.8 Predictor-corrector procedure of the iterative coupling scheme where k is iteration index. 37

2.9 Calculation procedures of the block marked with "Calculations of AAM and PDM" in Figure 2.8. 38

3.1 Schematic configuration of a finite length tensioned flexible panel flush-mounted in an infinite rigid flow duct (not-to-scale). 43

3.2 Sensitivity of numerical solutions to mesh size. (a) Time traces of total acoustic pressure. (b) Panel mobility. $-\cdot-\cdot-$: Mesh I; ——: Mesh II; – – –: Mesh III. 46

3.3 Variation of transmission loss TL with panel length L_p/H. —— , theoretical result (Huang 1999) with undamped panel; – – –, theoretical result with damped panel; ◯, numerical result with undamped panel; ×, numerical result with damped panel. 49

3.4 Acoustic response along the centerline of the duct with $L_p/H = 3.2$ within one incident wave period t_1. (a) & (b), the total fluctuation pressure $p'/(p'_{inc})_{amp}$; (c) & (d), the re-radiated waves $p'_{rer}/(p'_{inc})_{amp}$; (e) & (f), the phase shift of re-radiated wave relative to the incident wave. – – –, panel edges. 52

3.5 Acoustic response along the centerline of the duct with $L_p/H = 3.4$ within one incident wave period t_1. (a) & (b), the total fluctuation pressure $p'/(p'_{inc})_{amp}$; (c) & (d), the re-radiated waves $p'_{rer}/(p'_{inc})_{amp}$; (e) & (f), the phase shift of re-radiated wave relative to the incident wave. – – –, panel edges. 54

3.6 Panel responses. Left column, panel mobility spectra Y_k; right column, the distributions of panel mobility amplitude Y_x. (a) & (b), $L_p/H = 5$; ◯, numerical panel mode number N; ×, theoretical (Huang 1999) panel mode number; $\cdots\cdots$, theoretical undamped Y_k. (c) & (d), $L_p/H = 3.2$; (e) & (f), $L_p/H = 3.4$. (c) to (f), ——, $C = 0$; – – –, $C = 0.0196$. 56

3.7 Variations of acoustic response with M. (a) Re-radiation amplitude. Δ, upstream radiation; $*$, downstream radiation. (b) Phase shift (ϕ/π) between the downstream re-radiation relative to the incident wave. (c) $1-|\phi/\pi|$. (d) Transmission loss. 60

3.8 Re-radiation at different M ($L_p/H = 3.2$). Left column, p'_{rer} along the centerline of the duct. Right column, snapshots at selected t_1. 62

3.9 Panel responses. (a) Variation of Y_k spectra with M. (b) Distribution of dominant modal peaks. (c) Distribution of flexural wave velocity c_B. ——, the subsonic branch; $-\cdot-\cdot-$, the first mode of supersonic branch; $\cdots\cdots$, $c_B = 1$. (d) The difference between the two opposite flexural wave velocities. In (b) & (c), $\bigcirc$, $c_B > 0$; $\times$, $c_B < 0$. 66

3.10 Distributions of Y_x at different M. (a) $M = 0.1$; (b) $M = 0.5$; (c) $M = 1$; (d) $M = 1.2$. 69

3.11 Schematic configuration of a finite length tensioned flexible duct segment in an infinite rigid flow duct (not-to-scale). 72

3.12 The TL spectra of four different mean flow speeds (Li 2015). ——, $M = 0$; – – –, $M = 0.1$; – · – · –, $M = 0.5$; $\cdots\cdots$, $M = 0.9$. . . . 73

3.13 Frequency-wavenumber spectra of $Y_{k,f}$. (a), $M = 0$. (b), $M = 0.1$. (c), $M = 0.5$. (d), $M = 0.9$. – – –, theoretical prediction with incompressible flow; $\cdots\cdots$, acoustic wave speed in fluid. 75

3.14 Frequency-wavenumber spectra of p' at the duct centreline within $-0.5 < x < 0.5$. (a), $M = 0$. (b), $M = 0.1$. (c), $M = 0.5$. (d), $M = 0.9$. $\cdots\cdots$, acoustic wave speed in far field of fluid domain. 78

4.1 Time history of the vibrating velocity at $x = -0.41$. ——, result by the partitioned approach; – – –, result by the monolithic approach. 82

4.2 Free-body diagram of small control volumes of fluid elements in contact with a flexible panel segment. 84

4.3 Iterative procedure for Newton's method. 89

5.1 The schematic setup of the testing rig from Choy and Huang (2005). The upper right corner is the overview of the wind tunnel. The unit of the dimensions shown in the figure is mm. 102

5.2 Schematic configuration of the drum-like silencer (not-to-scale). . 103

5.3 Comparison of instantaneous distribution of vibrating velocities with $T = 0.108$ and $M = 0.026$. (a), $f = 0.294$ (200 Hz). (b), $f = 0.618$ (420 Hz). ——, numerical result; – – –, experimental data (Choy and Huang 2005). 105

5.4 Comparison of the TL spectrum of numerical result to experimental data with $T = 0.116$ and $M = 0.045$. ——, numerical result with viscous flow; $\cdots\cdots$, numerical result with inviscid flow; ◯, experimental data (Choy and Huang 2005). – – –, duct mode frequency $f_{2,0,0}$. 105

5.5 Illustration of the occurrence of second duct mode pressure distribution in the experiment. 107

5.6 Comparisons of the TL spectra of numerical result to experimental data with $T = 0.108$. (a), $M = 0$; – – –, duct mode frequency $f_{2,0,0}$ and $f_{3,0,0}$. (b), $M = 0.03$; – – –, duct mode frequency $f_{2,0,0}$. (c), $M = 0.045$; – – –, duct mode frequency $f_{2,0,0}$ and $f_{4,0,0}$. ——, numerical result with viscous flow; $\cdots\cdots$, numerical result with inviscid flow; ◯, experimental data (Choy and Huang 2005). . . . 108

5.7 Panel responses with $T = 0.116$ and $M = 0.045$. (a), the modal spectrum of panel mobility Y_k. (b), the distributions of panel mobility amplitude Y_x. (c), the averaged frequency spectrum of panel mobility Y_f on the whole panel. ◯ and ——, with cavities; × and – – –, without cavities. 111

5.8 Frequency-wavenumber spectrum of $Y_{f,k}$. (a), with cavities. (b), without cavities. · · · · · ·, acoustic wave speed in fluid. 113

5.9 Spectral variation of TL. ——, with cavities; – – –, without cavities. 114

5.10 Schematic configuration of the experimental setting of Liu (2011) (not-to-scale). 115

5.11 Velocity mean profile at the inlet. ——, numerical result. – – –, experimental data (Liu 2011). 117

5.12 Time traces of panel response. (a), strain. (b), kinetic energy. (c) & (d), vibrating velocity at $x = -0.17$ and 0 respectively. 118

5.13 Averaged frequency spectrum of the vibration velocity on the whole panel. ——, numerical result; – – –, experimental data (Liu 2011). − · − · −, duct mode frequencies. 119

5.14 Comparison of frequency spectrum of the vibration velocity with viscous and inviscid flow. ——, numerical result with viscous flow; · · · · · ·, numerical result with inviscid flow; – – –, experimental data (Liu 2011). − · − · −, duct mode frequencies. 121

5.15 Panel spatial response. (a), the modal spectrum of panel velocity. (b), the distributions of panel velocity amplitude. (c), the wavenumber spectrum of panel velocity at $f = 0.07$. 122

5.16 Pressure fluctuation along the duct centreline within one period of the dominate vibrating frequency, $t_1 = 1/f_0$. 123

5.17 Snapshot at $t/t_1 = 0.2$. (a), velocity fluctuation in y-direction. (b), pressure fluctuation. 124

5.18 Distribution of average intensity of the panel over a period $t_1 = 1/f_0$. 125

5.19 Time traces of panel response without cavity backed. (a), strain. (b), kinetic energy. (c), vibrating velocity at $x = 0$. 126

5.20 Averaged frequency spectrum of the vibration velocity. ——, without cavity backed. – – –, with cavity backed. 127

5.21 Panel spatial response without cavity backed. (a), the modal spectrum of panel velocity. (b), the distributions of panel velocity amplitude. (c), the wavenumber spectrum of panel velocity at $f = 0.105$. 128

5.22 Pressure fluctuation along the duct centreline within one period of the dominate vibrating frequency, $t_1 = 1/f_0$. 130

5.23 Distribution of average intensity of the panel over a period $t_1 = 1/f_0$. 131

List of Tables

2.1 Comparisons between numerical and theoretical in-vacuo eigenmode frequencies. 39

2.2 Comparisons between numerical and theoretical fluid loaded eigenmode frequencies. 40

3.1 Mesh designs. The mesh stretching function, $F_i\left(\Delta x_{min}, \Delta x_{max}, N_i\right)$ $= 0.5\left(\Delta x_{max} - \Delta x_{min}\right)\left\{\tanh\left\{9\left[(i-1)/(N_i-1) - 0.5\right]\right\} + 1\right\} + \Delta x_{min}$ where Δx_{min} and Δx_{max} are the minimum and maximum mesh sizes, N_i is number of meshes required, and $i = 1, 2, ..., N_i$ is the mesh index. 45

3.2 Comparisons between theoretical (Huang 1999) and numerical TL by staggered and iterative coupling schemes at various L_p/H. The values in brackets are ΔTL. 48

3.3 Deviation ΔTL of numerical results from theory (Huang 1999) in all cases in Figure 3.3. 50

4.1 Comparison of two approaches for third eigenmode vibration. . . . 97

4.2 Comparison of two approaches for acoustic-structural interaction in duct. 98

Abbreviations

AAM	Aeroacoustical Model
CE	Conservation Element
CE/SE	Conservation Element and Solution Element
DAS	Direct Aeroacoustic Simulation
SDM	Structural Dynamic Model
SE	Solution Element

Nomenclature

A_N	modal amplitude
C	structural damping coefficient
D	bending stiffness
D_f	relative difference between numerical and theoretical frequencies
E	total energy
E_p	modulus of elasticity
H	duct width and cavity height
I	flow intensity
I_{panel}	panel intensity
KE	kinetic energy
K_p	stiffness of foundation
L_0	reference length
L_p	panel length
M	Mach number
M_{added}	added mass
N	mode number
N_{iter}	number of iteration steps per time step
N_x	in-plane force of panel
Pr	Prandtl number
$\boldsymbol{Q}$	source term

R	specific gas constant
Re	Reynolds number
S	duct cross-sectional area
S_{su}	Sutherland's constant
T	temperature
T_0	reference temperature
T_x	external tensile stress of panel
T_{comp}	computational time per time step
TL	transmission loss
$\boldsymbol{U}$	solution vector
Y_k	modal panel mobility
Y_x	spatial panel mobility
Z_f	fluid impedance
a	characteristic dimension of a duct cross section
c_0	reference acoustic speed
c_B	phase velocity of panel wave
c_p	specific heat capacity
f	frequency
f_0	fundamental frequency
f_{crit}	critical frequency
$f_{fluid,N}$	eigenmode frequency of fluid loaded panel in theory
f_{n_1,n_2,n_3}	duct mode frequency
$f_{vacuum,N}$	eigenmode frequency of in-vacuo panel
h_p	panel thickness
k	wavenumber
l	size of the fluid volume in normal direction with panel deflection
l_i	dimensions of duct in three directions, $i = 1$, 2 and 3

l''	end correction
n_i	duct mode numbers along three directions, $i = 1$, 2 and 3
p	pressure
p_A	amplitude of incident wave
p_{ex}	net pressure exerted on panel
q_x	heat flux in x direction
q_y	heat flux in y direction
t	time
t_1	time of one period
u	fluid velocity in x direction
u_0	inlet mean flow speed
v	fluid velocity in y direction
w	panel displacement
w_x	first-order spatial derivative of panel displacement
w_{xx}	second-order spatial derivative of panel displacement
w_{xxxx}	fourth-order spatial derivative of panel displacement
$\dot{w}$	panel velocity
$\ddot{w}$	panel acceleration
ΔTL	difference between numerical and theoretical transmission losses
Δc_B	difference between two opposite flexural wave velocities
Δf	frequency resolution
Δt	time step size
Δx	grid size in x direction
Δy	grid size in y direction
γ	specific heat ratio
δ	size of the fluid volume in normal direction without panel deflection
ϵ	panel strain

ε	prescribed precision of convergence check
θ	phase
κ	thermal conductivity
λ	wavelength
μ	viscosity
ρ	density of fluid
ρ_0	reference density
ρ_p	density of panel
τ_{xx}	normal stress in in x direction
τ_{xy}	shear stress
τ_{yy}	normal stress in in y direction
ϕ	phase shifts of the re-radiated wave relative to the incident wave
ω	angular frequency

Subscripts

B	boundary cell
G	ghost cell
H	homogeneous solution
a	fluid element above panel
amp	wave amplitude
b	fluid element beneath panel
k	iteration index
panel, a	upper fluid-panel interface
panel, b	lower fluid-panel interface
rms	root mean square value

Superscript

$\bar{}$	time averaged value
$\hat{}$	dimensional quantity
$'$	fluctuation component
j	index of time step
n	index of panel mesh point

Chapter 1

Introduction

Flexible thin structures in contact with unsteady and moving fluid are commonly found in many engineering or biological applications. They are easily excited to vibrate by fluid disturbances or acoustic waves. The acoustic wave is also generated when the geometry of the structures or flow unsteadiness are changed. It will, in turn, propagates back to the source region and modifies the flow process or vibration that generating it. The vibration and noise problems always are major considerations in these applications because they may seriously reduce the system performance or environmental friendliness.

For example, noise problem happens in heating, ventilating and other flow ducting of domestic and industrial installations that internal noise generated by flow moving machines can transmit through the duct wall to exterior (Cummings 2001). In these situations, the surfaces of the cabin or the duct wall are always constructed by periodic stiffened thin metal panels, they are excited to vibrate by the noise or unsteady flow from one side and re-radiate noise to another side. Besides, undesired vibration and noise radiation also arise in piping and exhaust systems in automotive applications (Herrmann et al. 2012). During their operations, pressure pulsation is generated that may excite the pipe shells, whose vibration will then transmit to other car components and produces more noise.

These noise and vibration problems annoy users and surrounding people and lead to serious discomfort and even damage health. For the aircraft application, noise problem also occurs when external noise generated by an aircraft engine that transmitted through the airframe into the cabin and causing annoying to the passengers (Frendi et al. 1995). Besides noise problem, strong structural and/or acoustic loading will seriously endanger the safety of aerospace application. Subjected to prolonged structure-borne or aeroacoustic excitation during the fight operations or the launching of space vehicle or aircraft, fatigue of components in the vehicle arises that may cause the flight mission failure (Djojodihardjo 2008, 2015). In the biological application, the interaction between acoustic wave, flow and flexible structure also play a dominant role in many physiological phenomena include pulse-wave propagation in the arteries, phonation and snoring (Cisonni et al. 2017, Heil and Hazel 2011, Huang et al. 1995). The arteries are flexible tubes carrying blood flow with pulse-wave. The mechanisms of phonation and snoring are sound generation of flow and its induced vibration of flexible structure include larynx, pharynx, soft palate and so on. All the aforementioned examples involve complex interactions between the acoustics, flow, and structural dynamics. Since such kind of interaction significantly affecting the engineering system performance, safety, human health and comfortability, it is a critical consideration in the various engineering fields. The understanding of the interaction is a fundamental issue for further development of noise and vibration control at sources.

On the positive side, the interaction can be used to facilitate many engineering designs include energy harvesting, vibration, and noise controls. At a sufficiently high flow velocity, dynamic instability of flexible plate is induced which is known as flutter. During the flutter, energy is continuously transferred from the flow to the plate. Making use of the flutter motion, some researchers in-

troduced some innovative concepts for electrical power generation (Cisonni et al. 2017, Tang et al. 2009). On the other hand, flutter problem also occurs with airfoil during a flight that may lead to the aircraft lose its control. However, active control using acoustic excitations had been verified that can suppress such kind of flow-induced vibration (Huang 1987, Nagai et al. 1996). Conversely, noise problem also can be reduced by making use of flexible panel vibration. A drum-like silencer, which constructed by flexible panels backed by rigid cavities and flush-mounted in a duct, is an effective low frequency noise control design (Huang 1999). When the noise in the duct passes through the silencer, the flexible panels will be excited to vibrate and cause noise reflection to its source region. All these concepts are the applications based on the understanding of the interaction between acoustics, flow, and structural dynamics.

1.1 Literature survey

Researchers have attempted different approaches and angles to study the aforementioned interaction between three dynamics: acoustics, flow and structural dynamics. However many of them only consider either two dynamical processes and treat the remaining one as a minor effect that without interaction or even can be neglected. The following is going to briefly review those approaches.

1.1.1 Interaction of flow and structure

Some of the studies put the focus on flow-structure interaction over the acoustic aspects. An early interest of the interaction between flow and flexible structure arose from the interest in the boundary-layer stabilization concept inspired by dolphins. Dolphins can achieve anomalously high swimming speeds that was attributed to the flexibility of its skin that delaying the transition of a laminar

boundary layer to a turbulent one (Gaster 1987). Many research, e.g. Benjamin (1960, 1963), Landahl (1962) and Carpenter and Garrad (1986), extensively studied the effect of infinitely long flexible structure surface with an elastic foundation on hydrodynamic stability. They mainly focus on the travelling wave behaviour, such as dispersion relation, at the surface of an incompressible and irrotational fluid. Following the classification by Carpenter and Garrad (1986), two types of instabilities can be summarized: Tollmien-Schlichting instabilities and flow-induced surface instabilities. Tollmien-Schlichting instabilities exist only with the viscous flow and could be stabilized by increasing the solid surface flexibility or decreasing the structural damping. Flow-induced surface instabilities could exist with the inviscid flow and could be stabilized by heavy damping. The conditions of occurrence and long-time behaviour of absolute (temporal) and convective (spatial) instabilities are addressed and analysed by Brazier-Smith and Scott (1984), and Crighton and Oswell (1991). The flow-structural interaction in internal, viscous and incompressible flow is studied by Huang (2001b), Luo and Pedley (1998), Stewart et al. (2010), etc. Stewart et al. (2010) showed the viscous effect can destabilize the system.

Aeroelasticity and hydroelasticity are another branches of research directions on flow-structure interaction which are structure-based studies (Arzoumanian 2011, Paidoussis 2004). They are sharing same theories and approaches but applying on gas and liquid flow respectively. These studies mainly consider the absolute instability, includes flutter (dynamic) and divergence (static), of a flexible panel of finite extent immersed in inviscid flow. The structural vibration is expressed as a modal expansion of equivalent in-vacuo modes by Galerkin's methods. The aero/hydroelastic forces are also expressed in terms of frequency and wavenumber by Laplace and Fourier transforms. The complete aeroelasticity theory was presented in the monograph of Dowell (1975). He also summarized

four parameters playing the primary roles on the onset of the instability: flow velocity, panel length to width ratio, dynamic pressure (as compared to the panel stiffness) and fluid to panel mass ratio (Dowell 1970). Peake (2004) indicated that the onset of instability is also related to the relationship between panel length and bending wavelength in a long finite panel. Instability may occur if the panel length is not an exact multiple of bending wavelength.

Numerical simulations were conducted by Lucey and his co-workers (Lucey 1998, Lucey et al. 1997, Lucey and Carpenter 1992) to study the responses of both finite and infinite flexible panel excited by a point pressure pulse or subjected to a boundary layer with an inviscid flow. The effects of structural damping and inhomogeneity, such as stiffness change and end conditions, of the panel on instability were investigated. The results agreed with the traditional hydrodynamic stability theory that the damping allows energy transfer from the flow to the panel to destabilize it. However, the role of destabilizing is replaced by the edge conditions in the finite panel and the damping is only to attenuate the surface wave. Energy will be scattered by any strong local inhomogeneity. It was possible for the finite panel to respond at frequencies other than that of the driver in the presence of uniform flow. They also pointed out that the flow nonlinearity is important for the accurate calculation of surface instability. Pitman and Lucey (2009) also found that the panel response in a uniform flow is dominated by attenuating upstream- and amplifying downstream-traveling motions. On the other hand, Davies and Carpenter (1997a,b) presented very detailed studies of the instabilities on a finite panel induced by Tollmien-Schlichting waves in a channel flow. The stabilization or occurrence of instability, such as travelling wave flutter or divergence, are depended on combination of panel length, wavelength of panel and Tollmien-Schlichting waves.

There are recent studies, e.g. Cisonni et al. (2017), Howell and Lucey

(2012), and Huang and Zhang (2013), concerned with the instability of a cantilevered panel in open or confined flow. The stability is found sensitive to some factors, such as the mounting at the leading edge, the mass at the trailing edge and the distance of the confinement. The viscous effect on a cantilever in internal flow is studied by Cisonni et al. (2017). The viscosity stabilizes the system, reduces the critical flow velocity and changes the first unstable structural mode. More comprehensive reviews on the studies of stability problem are provided by Abrahams and Wickham (2001), Arzoumanian (2011), Lucey et al. (1997), Paidoussis (2004), Peake (2004), Shankar (2015), and Stewart et al. (2010).

Furthermore, some researches, e.g. Clark and Frampton (1997) and Tang et al. (2007), calculated the acoustic radiation from the flow-structure interaction in inviscid flow. Schäfer et al. (2010) built a model investigate the acoustics radiated from vibration excited by a low Mach number turbulent flow. They showed both structural and acoustic responses were reduced by higher flow velocity and stronger isotropy of the turbulent fluctuations. In the problems of interest in these studies, fluid is always unconfined so the feedback of acoustics radiated from the vibration will be taken as an ignorable effect in the interaction.

1.1.2 Interaction of acoustics and structure

The field of study of the structural vibration, its response to sound and radiation to the surrounding still fluid is known as vibroacoustic or structural acoustics (Fahy and Gardonio 2007), which is acoustics-based study. The acoustic behavior in an inviscid, isotropic and compressible fluid is governed by the wave equation. Similar to the approach applied in aeroelasticity, the wave equation is transformed to a frequency domain by Laplace and Fourier transforms. The motion of the structure is also considered as a simple harmonic wave, that may be driven by acoustic incident or mechanical forces.

The influences of heavy and light fluid loadings on the acoustic radiation from an infinite flexible panel driven by localized forces are firstly addressed by Maidanik and Kerwin (1966). The importance of the acoustic effect in the fluid-structure interaction had been pointed out by Crighton (1984). He studied the influence of fluid loading on periodically ribbed panels and divided it into two types: subsonic surface wave and acoustic component. Since the panel segments separated by the ribs, the fluid motion induced by the vibration provided the only connection that allows structural waves transmission between two segments. The subsonic surface wave provides a local coupling (between the neighboring panel segments) under heavy fluid loading and the acoustic component provides a long-range coupling (between the non-neighboring panel segments). The acoustic radiation is strictly different subjected to subsonic and supersonic surface wave speed. Ffowcs Williams and Hill (1987) indicated that the energy radiated by a supersonic surface wave is much larger than subsonic one. The details of the theory of fluid loading were presented in the work of Crighton (1989).

The acoustic-structural interaction in a confined fluid was studied by Huang (1999, 2001a). By using Doak's theory (Doak 1973), he considered the vibration as a collection of harmonic point sources to calculate the pressure field generated in a duct. He showed that large transmission loss of a grazing incident acoustic wave can be achieved through the excitation of panel vibration and its re-radiation. The effectiveness is dominated by the panel length to duct width ratio and structural damping. Moreover, some other research, e.g. Maestrello et al. (1992), and Aginsky and Gottlieb (2012, 2013), concern the structural stability subjected to an acoustic loading of normal incidence. Linear, nonlinear and chaotic responses can be observed by increasing the sound pressure level of the incidence.

In addition, the effect of mean flow on the interaction between acoustics

and structure was also studied through the convected wave equation, e.g. Abrahams (1983), Choi and Kim (2002), and Ko (1994). Except for the properties of the panel itself, the panel response was found dependent on the flow speed. Sucheendran et al. (2014) investigated a similar problem in a duct by extended Doak's theory to account for uniform mean flow. They revealed the free vibrating frequencies in the presence of flow will significantly deviate from the in vacuo natural frequencies. The flow also reduced the peak response of the panel. However the effects of flow in these studies are calculated by linear and inviscid theories, nonlinear interaction and the effect of viscosity cannot be accounted.

1.1.3 Aeroacoustic-structural interaction

So far there are a large number of studies worked on the fluid-structure interaction. They reveal that acoustics, flow, and structural dynamics are certainly strong coupled together. Fluid provided additional mass to shift the natural frequencies of vibration and damping to attenuate the vibration. The presence of flow enhances the variability of the interaction. It may attenuate or amplify the vibration and may induce instabilities no matter in viscous or inviscid. The acoustic effect also plays an important role in the fluid-structure coupling (Crighton 1984), especially for internal flow problem. Unlike in an open flow problem, the sound radiated from a vibrating structure cannot propagate away but confined near its source. The acoustic effect on the vibration created by itself could be strong. The nonlinear and chaotic phenomenon can be induced if the acoustic excitation is strong enough (Maestrello et al. 1992). Maestrello and Grosveld (1992) carried out an experimental study on the effect of an acoustically excited flexible surface on the transition of a boundary layer. They found both sound and vibration were involved in the destabilization of the boundary layer. It showed clear evidence that three dynamic processes are inherently coupled, their responses are

nonlinear and cannot be simulated if anyone is missed. Therefore three dynamics have equivalent importance and their interaction should be analysed together carefully by an appropriate coupling approach. To distinguish the interaction problem involving all three dynamical processes together from the others, it is appropriate to describe such kind of problem as an aeroacoustic-structural interaction.

It is nearly impossible to solve highly nonlinear problems analytically because of their complexity. Many of the aforementioned studies applied simplified and linearized models together with analytical treatment, e.g. Crighton and Oswell (1991), Huang (1999, 2001a) and Choi and Kim (2002). They provided many significant fundamental understandings on the problem with simple geometry. However, the linear fluid model cannot accurately predict the flow-structure interaction with nonlinear oscillatory behaviour (Lucey et al. 1997). To further improve our understanding and deal with more complex configurations, the computational study is necessary (Korobkin et al. 2011). Computational method able to resolve the nonlinear problems in a numerical way and handle a large number of calculations.

Besides, the analytical study is always performed in the frequency domain and assumed the solutions are time-harmonic. It provides the time integrated or averaged results, and help people to understand the overall characteristics of the problems or the systems. However, the details of any transient and time evolution are missed. The time-harmonic assumption may also not effective to capture some transient or weak dynamics because the solution always is a summation of harmonic modes and the numbers of modes are limited which miss the high order effect. Therefore, they are far from satisfactory for the predictions of more practical and complex situations. For the understanding of the actual operation of the interaction between different dynamics, the details of transient and time

evolution must be captured. Therefore, the time-domain analysis will be a more suitable for the present studies.

Rare attempts are completely accounting all effects of three dynamics to each other. One of the complete numerical models on fluid-structure interaction was developed by Visbal and Gordnier (2004). They employ the compressible Navier-Stokes and von Karman plate equations for the fluid and structural domains respectively. The fluid solutions, which involve both flow and acoustic responses, are discretized by a sixth-order finite-difference method and solved with Newton-like sub-iterations to achieve second-order time accuracy. The structural solutions are also solved by the finite-difference method with second-order accuracy. Two domains are then coupled by an iterative implicit scheme. However, their study mainly focuses on the phenomena of instability rather than the acoustics. They revealed the flutter is independent of the type of panel ends conditions in supersonic flow. The divergence and traveling-wave-flutter emerged for low and high dynamic pressure respectively in high subsonic flow. Therefore, the current state of efforts in resolving the coupled interactions is still far from satisfactory.

1.2 Fluid-structure coupling

The fluid and structural dynamics are normally modeled by respective equations systems. A coupling must be constructed to achieve their connections and interactions. Different coupling schemes have been developed in the past. The benefits and drawback of different modelings and coupling schemes are reviewed by Dowell and Hall (2001) and Kamakoti and Shyy (2004). The coupling schemes can be generally classified into two categories: partitioned and monolithic approaches.

1.2.1 Partitioned approach

In the partitioned approach, separate solvers are used for different physical domains and an additional procedure is employed to handle the data transfer across interfaces between the domains. A detailed summary of different solvers along with interfacing methodologies was presented by Kamakoti and Shyy (2004). The major benefit of this approach is its flexibility. Different discretization techniques, solution algorithms, and independent modelings can be used for different domains. The efficiency may be enhanced by optimizing the individual algorithms and modelings. It is convenient if specialized solvers are readily available, only coupling procedures for the interfaces is required to develop. The solvers and the coupling procedures can be maintained, advanced and replaced separately for further improvement (Felippa et al. 2001, Heil 2004). However, interpolation and/or extrapolation must be employed if the solution points at the interfaces of the models are not identical. This eventually increases the computational cost and leads to substantial loss of the accuracy information, especially those at high frequencies.

The most straightforward, simple and time effective coupling scheme are staggered time-integration scheme, which also described as loose or weak coupling. It solves each domain once and one by one in each time step. The major drawback is the effects at the interface are always lag one time step in relation to the internal effect. When the first domain is going to be updated, the information contained in other domains are not updated yet, so the effects from the internal and external cannot be synchronized. The conservation properties of the continuum of the systems may be lost. Thus small errors may be generated and accumulated that lead to inaccurate solutions or poor stability. The solution of the time lagging problem is to introduce iterative correction scheme (Felippa et al. 2001, Heil 2004, Rugonyi and Bathe 2001), which also described as tight

or strong coupling correspondingly. In the beginning of each single time step, same procedure in the staggered scheme is carried out as an initial guess. It then feeds the updated solutions back to the first solver and reprocess all domains to correct the solutions. This feedback and reprocessing procedure will be repeated until the solutions converge. However, it may still unstable if the structure has low elasticity in relation to the compressibility of fluid. This can be overcome by underrelaxation in the iteration (Greenshields and Weller 2005). Besides, subcycling which multi time scales are used for different domains can be applied to enhance efficiency. However, there is still no guarantee of computationally efficient. The iterative method may tend to converge slowly. To achieve tight coupling, a large number of iterations is then required that extremely demanding on computational resources (Felippa et al. 2001, Greenshields and Weller 2005, Heil 2004, Rugonyi and Bathe 2001).

The approach proposed by Schäfer et al. (2010) is a good example. They attempted to calculate the acoustic field generated from a turbulent flow and its induced vibration of a thin flexible panel with in time-domain through a hybrid approach. First, the flow and the panel responses are resolved from a finite-volume incompressible large-eddy simulation solver and a finite-element structural solver. The unsteady flow and panel vibration solutions are then fed in a finite-element acoustic solver to calculate their individual acoustic contributions and were summed up to produce the total acoustic field. From this point of view, acoustics, flow, and structural dynamics are solved in three separate solvers with three pairwise channels. It inevitably involves many interpolation and/or extrapolation and a large number of iterations that consequently lead to computational cost ineffective and degradation of accuracy.

1.2.2 Monolithic approach

In the monolithic approach, the governing equations are reformulated by combining all different physical domains, then discretizes and solves all domains simultaneously. Newton-Raphson method or similar techniques with iteration procedures are always applied for the implicit solutions in the governing equations. Normally, this approach has faster convergence than the partitioned approach and unconditional stability because of the inherent coupling that guarantees the conservations and time accurate solutions (Greenshields and Weller 2005, Ishihara and Yoshimura 2005). However, it still has some drawbacks. If the rigidity and/or the mass of the structure are too large compared to the fluid, ill-conditioned system matrices may be obtained and lead to slow convergence or even divergence in the iteration procedure. A solution of this drawback is to develop appropriate preconditioners for the iterative solution (Ishihara and Yoshimura 2005, Rugonyi and Bathe 2001). Besides, the approach may be costly in computational resources. First, the main computational time cost may arise from the repeated assembly of the Jacobian matrix for the Newton method (Heil 2004). Second, the number of degrees of freedoms in the equations is increased since all physical domains be solved simultaneously. The storage of the variables will require a large amount of memory. This drawback can be overcome by a substructuring procedure to reduce the degrees of freedoms, such as expressing the structure variables in terms of fluid variables (Ishihara and Yoshimura 2005).

An example of monolithic coupling scheme was presented by Rugonyi and Bathe (2000, 2001). They aimed to study the flow-structural interaction in a Newtonian incompressible fluid. The governing equations for fluid and structure are discretized by the finite-element method and formed as a linearized coupled equations in a matrix form. The nodes at the interface between flow and structure domains are required coincident. Therefore the flow and structural responses can

be resolved simultaneously by using the Newton-Raphson method.

1.3 Research scopes

The aim of the present work is to develop an effective yet accurate numerical methodology that facilitates the better understanding of aeroacoustic-structural interaction in internal flow for advancing silencing design.

Recently Lam et al. (2014a) developed a validated and accurate aeroacoustic solver by using conservation element and solution element method for two-dimensional compressible Navier-Stokes equations and validated it with analytical solutions, experiments, and incompressible simulation results. This solver is adopted for the fluid model. Therefore the numerical model for the flexible panels and the coupling between two models are going to be developed in this thesis. Because of the aeroacoustic solver is readily available, partitioned coupling approach is the primary choice to take its advantage of simplicity. However, both partitioned and monolithic approaches have specific benefits and drawbacks. The monolithic approach may also be developed for different situations if necessary. The methodologies will be validated theoretically and experimentally. The theory on a duct silencer design introduced by Huang (1999) and the related experiments (Choy and Huang 2005, Liu 2011) are selected as benchmarks cases for validation. Based on the results in these cases, the aeroacoustic-structural response in a duct is analysed in both inviscid and viscous grazing flow, with and without grazing acoustic incidence, and with and without cavity backed flexible panel. Since some ducts commonly used in real applications have a small height to width ratio, an example is shown as Figure 1.1, the boundary effect in spanwise direction is small for the duct centre. Therefore two-dimensional assumption is adopted in the thesis.

Figure 1.1: Ventilation ducts commonly found in Hong Kong.

1.4 Outline

The remainder of the thesis is organized as the following.

Chapter 2 introduces the physical models and the numerical methodology by partitioned approach for solving the aeroacoustic-structural interaction in inviscid flow. The detail of the aeroacoustic and panel dynamic models, and the staggered and iterative coupling schemes are presented.

Chapter 3 presents the validation of the partitioned approach by comparing with an inviscid theoretical solution, and the analysis of the aeroacoustic-structural interaction of an acoustic-induced panel vibration in a duct. The accuracies of staggered and iterative coupling schemes are also discussed. The acoustic-structural responses with single frequency excitation, the effect of flow,

and the aeroacoustic-structural responses with broadband excitation are studied in detail.

Chapter 4 describes the derivation of the coupled governing equations and the numerical treatment by monolithic approach for the viscous problem since the partitioned one is found that cannot handle this problem. The accuracies and efficiencies of two approaches are also compared.

Chapter 5 gives the validation of the capability in capturing the aeroacoustic-structural interaction in a viscous flow of the monolithic approach by comparing with two experimental studies, and the analysis on the interaction of broadband acoustic- and flow-induced panel vibration in a duct. The aeroacoustic-structural responses, the effect of viscosity and cavity are investigated.

Chapter 6 summarizes the achievements and knowledge obtained in this thesis and comments on the further improvement and study of the computational aeroacoustic-structural interaction.

Chapter 2

Physical Models and Numerical Methods

The partitioned approach is employed for the aeroacoustic-structural interaction problem with inviscid fluid and sliding flexible panel because of its flexibility and convenience for the numerical methodology development. The accuracy is also satisfied as shown in the next chapter. It treats the fluid and the structure in separate solvers, and then allows their communication by a coupling strategy. Therefore to obtain an accurate aeroacoustic-structural response of a flexible panel exposed to flow and acoustic wave in the time-domain, three key elements are required in this methodology. They are (i) the modeling of aeroacoustics of the fluid, (ii) the modeling of the dynamic response of the panel, and (iii) the coupling strategy for correctly accomplish the interplay between aeroacoustics and panel dynamics. All of these elements must be included in the formulations of the numerical solvers and each one of them must be selected according to the specific configuration considered. The formulations and the corresponding numerical solvers are described in the following sections. In the present study, the fluid domain is only considered in two-dimensions and so the panel domain is considered in one-dimension. All the variables mentioned in the followings are

normalized by a reference length $\hat{L}_0$, a reference density $\hat{\rho}_0$ and a reference acoustic speed $\hat{c}_0$. Reader are reminded that the hat ($\hat{}$) denote dimensional variables.

2.1 Aeroacoustic model

In fact, the acoustic motion is simply a kind of unsteady flow motions supported by a compressible fluid medium (Crighton 1981). It is logical to adopt a numerical model for the medium that allows simultaneously calculate both the unsteady flow and the acoustic field. Otherwise, the inherent nonlinear interaction of these two fields cannot be accounted correctly in the calculation. This capability is particularly important for resolving the aeroacoustic problem in internal flow. It is because the acoustic fluctuations experience multiple reflections and scattering inside the duct and may propagate back and change the unsteady flow dynamics and the panel vibration that generating it. As such, we adopt an aeroacoustic model based on direct aeroacoustic simulation (DAS) scheme (Lam et al. 2013, 2014a) in the present study.

The aeroacoustic problem is governed by the two-dimensional compressible Navier-Stokes equations together with the ideal gas law for calorically perfect gas. The strong conservation form of the normalized Navier-Stokes equations without source can be written as,

$$\frac{\partial \boldsymbol{U}}{\partial t} + \frac{\partial \left(\boldsymbol{F} - \boldsymbol{F}_v\right)}{\partial x} + \frac{\partial \left(\boldsymbol{G} - \boldsymbol{G}_v\right)}{\partial y} = 0, \tag{2.1}$$

where

$$\boldsymbol{U} = \begin{bmatrix} \rho \\ \rho u \\ \rho v \\ \rho E \end{bmatrix}, \qquad \boldsymbol{F} = \begin{bmatrix} \rho u \\ \rho u^2 + p \\ \rho uv \\ (\rho E + p)u \end{bmatrix}, \qquad \boldsymbol{F}_v = \frac{M}{Re} \begin{bmatrix} 0 \\ \tau_{xx} \\ \tau_{xy} \\ \tau_{xx}u + \tau_{xy}v - q_x \end{bmatrix},$$

$$\boldsymbol{G} = \begin{bmatrix} \rho v \\ \rho uv \\ \rho v^2 + p \\ (\rho E + p)v \end{bmatrix}, \qquad \boldsymbol{G}_v = \frac{M}{Re} \begin{bmatrix} 0 \\ \tau_{xy} \\ \tau_{yy} \\ \tau_{xy}u + \tau_{yy}v - q_y \end{bmatrix},$$

$$E = \frac{p}{\rho(\gamma - 1)} + \frac{1}{2}(u^2 + v^2), \qquad p = \frac{\rho T}{\gamma}, \tag{2.2}$$

$$\tau_{xx} = \frac{2}{3}\mu\left(2\frac{\partial u}{\partial x} - \frac{\partial v}{\partial y}\right), \quad \tau_{yy} = \frac{2}{3}\mu\left(2\frac{\partial v}{\partial y} - \frac{\partial u}{\partial x}\right), \quad \tau_{xy} = \mu\left(\frac{\partial u}{\partial y} + \frac{\partial v}{\partial x}\right),$$

$$q_x = -\kappa\frac{\partial T}{\partial x}, \qquad q_y = -\kappa\frac{\partial T}{\partial y},$$

$\rho = \hat{\rho}/\hat{\rho}_0$ is the density of fluid, $u = \hat{u}/\hat{c}_0$ and $v = \hat{v}/\hat{c}_0$ are the velocities in $x = \hat{x}/\hat{L}_0$ and $y = \hat{y}/\hat{L}_0$ direction respectively, $t = \hat{t}\hat{c}_0/\hat{L}_0$ is the time, $p = \hat{p}/(\hat{\rho}_0\hat{c}_0^2)$ is the pressure, $E = \hat{E}/\hat{c}_0^2$ is the total energy, q_x and q_y are the heat fluxes, τ_{xx}, τ_{yy} and τ_{xy} are normal and shear stresses, $\mu = \hat{\mu}/\hat{\mu}_0$ is the viscosity, the thermal conductivity $\kappa = \mu c_p/Pr$, the specific heat capacity $c_p = 1/(\gamma - 1)$, the specific heat ratio $\gamma = 1.4$, Prandtl number $Pr = \hat{c}_p\hat{\mu}_0/\hat{k}_0 = 0.71$, the Mach number $M = \hat{u}_0/\hat{c}_0$, the Reynolds number $Re = \hat{\rho}_0\hat{u}_0\hat{L}_0/\hat{\mu}_0$, $\hat{u}_0$ is the mean flow velocity, the acoustic speed $\hat{c}_0 = \sqrt{\gamma\hat{R}\hat{T}_0}$ is also used as reference velocity, and the reference temperature $\hat{T}_0 = 288.2$ K. The relationship between viscosity and temperature is given by Sutherland's Law,

$$\mu = T^{\frac{3}{2}}\frac{1 + \hat{S}_{su}/\hat{T}_0}{T + \hat{S}_{su}/\hat{T}_0}, \tag{2.3}$$

where Sutherland's constant $\hat{S}_{su} = 110.4$ K. For inviscid fluid, the viscous terms will be ignored, i.e. $\boldsymbol{F}_v = \boldsymbol{G}_v = 0$, that the aforementioned equations become Euler equations.

2.1.1 The conservation element and solution element method

Low dispersive and dissipative are the necessary requirements for DAS scheme because of the great disparity of the energy and length scale between acoustics and flow dynamics (Lam et al. 2014a). That is why the high-order finite-difference scheme is applied in the work of Visbal and Gordnier (2004). However, high-order schemes are always highly demanding in the computational resources. The major disadvantage of the finite difference method is that is only efficient with uniform and regular meshes, so it is not suitable for complex geometries (Hamdan and Dowling 1995). On the other hand, the finite-element method may be a better choice that provides a greater versatility in modelling complex geometries. However, it is computationally expensive in terms of computer time and storage requirements because it has to handle a huge matrix calculation. An alternative is the space-time conservation element and solution element (CE/SE) method (Chang 1995) that the accuracy up to second order although it is built to first order in nature (Lam et al. 2014a), so it should be more efficient than the high-order finite-difference scheme. It emphasises on the strict conservation of physical laws and the unified treatment in both space and time, that is a completely different concept from finite-difference or finite-element schemes. Lam et al. (2014a) showed that conservation element and solution element method is capable of resolving the low Mach number interactions between the unsteady flow and acoustic field accurately by calculating the benchmark aeroacoustic problems with increasing complexity. Therefore, the CE/SE method based the DAS solver is adopted as the aeroacoustic model in the present study. The full description of the solver can be referred to the works of Lam (2011), the concept is briefly described in the following.

Let the spacial coordinates x and y, and the time t be considered as the

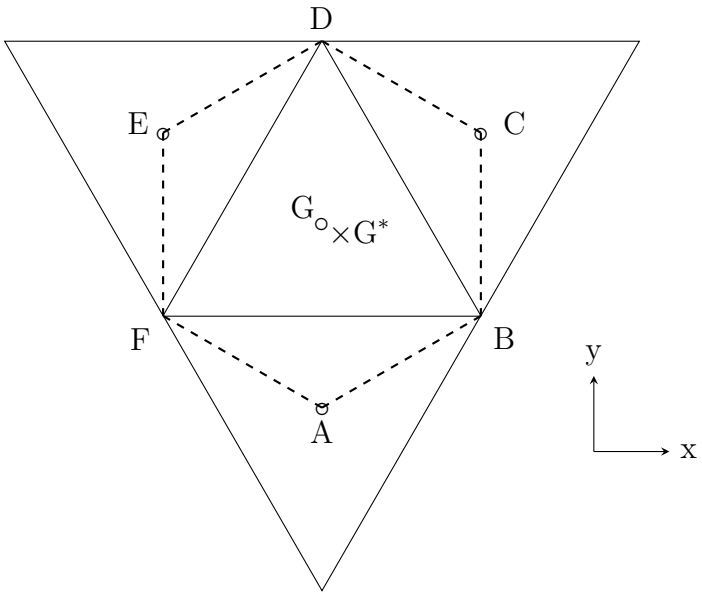

Figure 2.1: Triangulate grids in a computational domain. ∘ : A, C, E and G are the centroids of the grids; B, D and F are the nodes; × : G* is a solution point; and − − − is the boundary of a CE.

coordinates of a three-dimensional Euclidean space E_3. The equation in the strong conservation form, Equation 2.1, can be written as,

$$\nabla \cdot \boldsymbol{K} = 0, \tag{2.4}$$

which $\nabla\cdot$ is the divergence operator in E_3 and $\boldsymbol{K} = [\boldsymbol{F} - \boldsymbol{F}_v,\ \boldsymbol{G} - \boldsymbol{G}_v,\ \boldsymbol{U}]$. By using Gauss's divergence theorem in E_3, Equation 2.4 can be written as the integral conservation law,

$$\oint_{S(V)} \boldsymbol{K} \cdot d\boldsymbol{s} = 0, \tag{2.5}$$

where $d\boldsymbol{s} = [\Delta x,\ \Delta y,\ \Delta t]$ and $S(V)$ is the surface of an arbitrary space-time region V in E_3. The computational domain is then decomposed into triangulate grids as Figure 2.1. The figure shows a grid BDF and its centroid is G. A, C and E are the centroids of adjacent grids. To construct a conservation element (CE), the nodes of a grid and the adjacent centroids will be connected to form

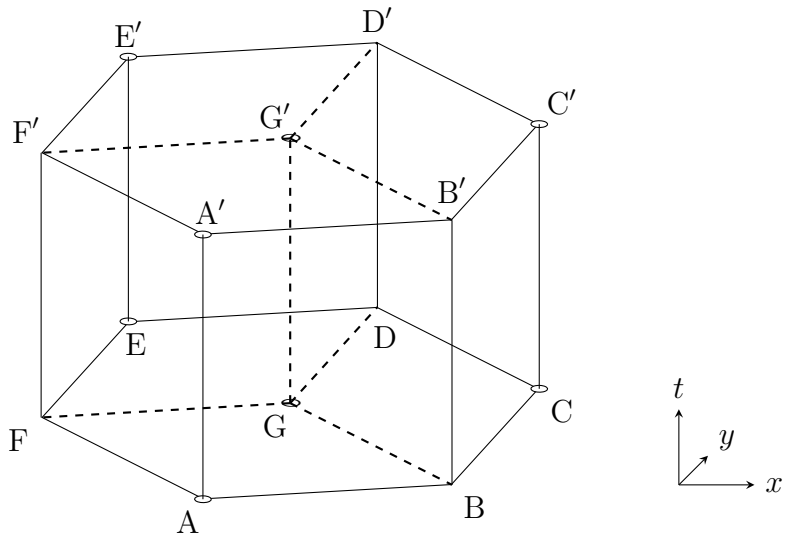

Figure 2.2: Geometrical definitions of $CE(\mathrm{G}^*,\, j)$. $---$ is the boundary of $SE(\mathrm{G}^*,\, j)$.

the boundary, i.e. ABCDEF. G^* is the centroid of the hexagon ABCDEF, but notice that the grids can be non-uniform, and G^* and G may not be the same point in this situation. G^* is also taken as the solution point of the hexagon. The hexagon is then extended in time axis to form a hexagonal prism, that defined as a CE. Conservation of flux, Equation 2.5, is enforced in it. The CE shown in Figure 2.2 is denoted as $CE(\mathrm{G}^*,\, j)$, where G^* represents the spatial location and n denotes the j-th time level.

Meanwhile, a solution element (SE) is formed by all the adjacent planes of the corresponding solution point as Figure 2.3 for example. The flow variables $\boldsymbol{\Psi}(\boldsymbol{X}) = \boldsymbol{U}(\boldsymbol{X})$, $\boldsymbol{F}(\boldsymbol{X})$, $\boldsymbol{F}_v(\boldsymbol{X})$, $\boldsymbol{G}(\boldsymbol{X})$ or $\boldsymbol{G}_v(\boldsymbol{X})$ at any location $\boldsymbol{X}$ within the $SE(\mathrm{G}^*,\, j)$ can be estimated by first order Taylor expansions from the solution point G^*,

$$\boldsymbol{\Psi}\left(\boldsymbol{X}\right) = \boldsymbol{\Psi}_{\mathrm{G}^*} + \left(x - x_{\mathrm{G}^*}\right)\left(\boldsymbol{\Psi}_x\right)_{\mathrm{G}^*} + \left(y - y_{\mathrm{G}^*}\right)\left(\boldsymbol{\Psi}_y\right)_{\mathrm{G}^*} + \left(t - t_{\mathrm{G}^*}\right)\left(\boldsymbol{\Psi}_t\right)_{\mathrm{G}^*}, \quad (2.6)$$

where the terms with subscripts x, y, and t are the derivatives respect to x, y, and t respectively. However, the viscous terms $\boldsymbol{F}_v(\boldsymbol{X})$ and $\boldsymbol{G}_v(\boldsymbol{X})$ are assumed

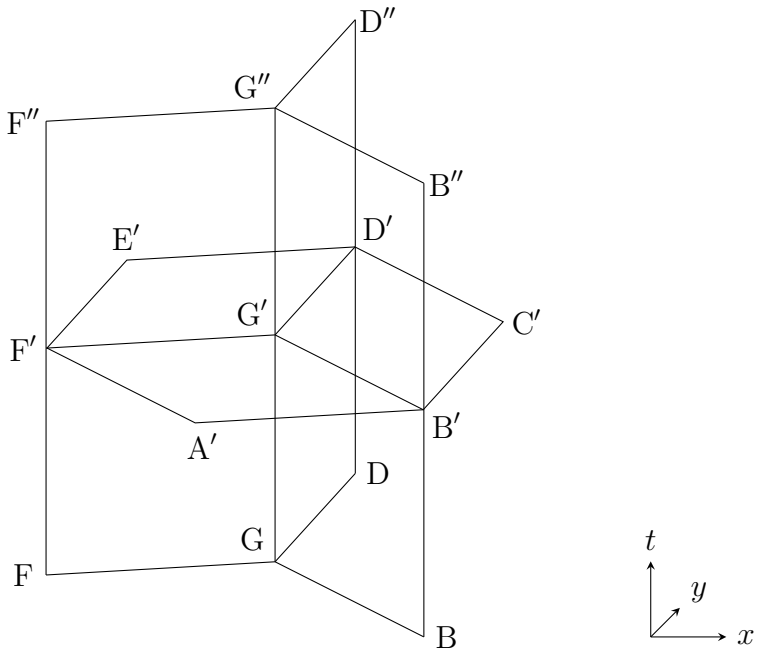

Figure 2.3: Geometrical definitions of $SE(\mathrm{G}^*,\, j)$.

as constant within the $SE(\mathrm{G}^*,\, j)$. Therefore the Navier-Stokes equations can be expressed as

$$(\boldsymbol{U}_t)_{\mathrm{G}^*} = -\,(\boldsymbol{F}_x)_{\mathrm{G}^*} - (\boldsymbol{G}_x)_{\mathrm{G}^*}\,, \tag{2.7}$$

and $\boldsymbol{K}(\boldsymbol{X})$ can also be approximated as

$$\boldsymbol{K}\,(\boldsymbol{X})_{\mathrm{G}^*} \equiv [\boldsymbol{F}(\boldsymbol{X})_{\mathrm{G}^*} - \boldsymbol{F}_v(\boldsymbol{X})_{\mathrm{G}^*},\; \boldsymbol{G}(\boldsymbol{X})_{\mathrm{G}^*} - \boldsymbol{G}_v(\boldsymbol{X})_{\mathrm{G}^*},\; \boldsymbol{U}(\boldsymbol{X})_{\mathrm{G}^*}]\,. \tag{2.8}$$

As such all the fluxes through the planes in solution element and flow variables can be approximated by the solution point G^*.

The time marching of the solution is carried out as the following. For $CE(\mathrm{G}^*,\, j)$ in Figure 2.2, the fluxes through planes ABGF, ABB′A′ and FAA′F′ are approximated by $SE(\mathrm{A}^*,\, j-1/2)$; similarly, the fluxes through planes CDGB, CDD′C′ and BCC′B′ are approximated by $SE(\mathrm{C}^*,\, j-1/2)$; and the fluxes through planes EFGD, EFF′E′ and DEE′D′ are approximated by $SE(\mathrm{E}^*,\, j-1/2)$. The flux $\boldsymbol{U}_t$ through the top plane A′B′C′D′E′F′ can be found because of the conservation

of flux. The fluid variables $\boldsymbol{U}$ at G* at j-th time step can also be determined.

2.2 Panel dynamic model

The dynamic response of the flexible panel can be generally modelled with the two-dimensional nonlinear Von Karman's theory for an isotropic rectangular elastic plate on Kelvin foundation (Rao 1999). The panel is assumed to be of uniform small thickness $h_p = \hat{h}_p/\hat{L}_0$ and initially flat. However, the nonlinear dynamic response can be simplified to the one-dimension plate equation with simplest approximation (Dowell 1975). Using the same set of reference parameters adopted in the aeroacoustic model, the normalized governing equation for panel displacement $w(x) = \hat{w}/\hat{L}_0$ can be written as,

$$D\frac{\partial^4 w}{\partial x^4} - (T_x + N_x)\frac{\partial^2 w}{\partial x^2} + \rho_p h_p \frac{\partial^2 w}{\partial t^2} + C\frac{\partial w}{\partial t} + K_p w = p_{ex}, \tag{2.9}$$

where $D = \hat{D}/(\hat{\rho}_0 \hat{c}_0^2 \hat{L}_0^3)$ is the bending stiffness, $T_x = \hat{T}_x/(\hat{\rho}_0 \hat{c}_0^2 \hat{L}_0)$ is the external tensile stress resultant per unit length in the tangential direction (i.e. x-direction), N_x is the in-plane force in the tangential direction induced by stretching, $L_p = \hat{L}_p/\hat{L}_0$ is the length of panel, $\rho_p = \hat{\rho}_p/\hat{\rho}_0$ is the density of panel, $C = \hat{C}/(\hat{\rho}_0 \hat{c}_0)$ is the structural damping coefficient, $p_{ex} = \hat{p_{ex}}/(\hat{\rho}_0 \hat{c}_0^2)$ is the net pressure exerted on the panel surface, and $K_p = \hat{K}_p \hat{L}_0/(\hat{\rho}_0 \hat{c}_0)$ is the stiffness of foundation. K_p is set equal to zero for all cases reported in the thesis. Four types of flexible panels can be classified according to their ratio of thickness to length (h_p/L_p) (Szilard 2004). They are membranes ($h_p/L_p < 1/50$), stiff plates ($1/50 < h_p/L_p < 1/10$, "plate" is understood to mean stiff plate in engineering practice), moderately thick plates ($1/10 < h_p/L_p < 1/5$) and thick plates ($h_p/L_p > 1/5$). It is necessary to carry out a full three-dimensional stress analysis to yields sufficiently accurate results for the moderately thick plates and thick plates ($h_p/L_p > 1/10$). Therefore, they are not considered in the present study. For the stiff plates with $h_p/L_p \gg 1/50$,

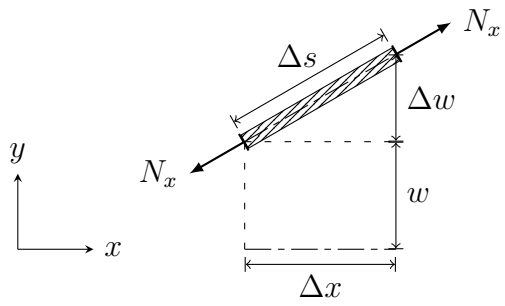

Figure 2.4: Free-body diagram of a small deflected flexible panel segment.

the restoring force will be dominated by bending stiffness compared to the tensile forces, so they are negligible, $(T_x+N_x) = 0$. In another situation, the tensile forces will dominate the membranes motion, flexural resistance will be not appreciable, $D = 0$. On the other hand, the in-plane shear stress can be ignored because the sideways motion at every point on the membrane is negligible when the deflections are small in comparison with the thickness ($w/h_p \leq 0.2$). The panel motion can be assumed linear. Therefore, the nonlinearity term is then ignored, $N_x = 0$, and the tensile force on the middle surface remains constant, which is the small-deflection theory. For $w/h_p \gg 0.2$, the panel motion is no longer linear. The large-deflection theory should be employed. The nonliear tensile force will even dominates if $w/h_p \gg 1$ (Dowell 1975, Szilard 2004).

The large-deflection theory accounts for the in-plane force created by the stretching of a deflected panel (Szilard 2004). The in-plane force can be obtained by Hooke's Law (Dowell 1975),

$$N_x = E_p h_p \epsilon, \tag{2.10}$$

where ϵ is the strain and $E_p = \hat{E}_p \hat{c}_0^2/(\hat{\rho}_0 \hat{L}_0^4)$ is the modulus of elasticity. When a small panel segment in one dimension is elongated from Δx to Δs long after deflection as shown in Figure 2.4, the strain of the segment is

$$\epsilon' = \frac{\Delta s - \Delta x}{\Delta x} = \frac{\Delta s}{\Delta x} - 1. \tag{2.11}$$

The Pythagorean theorem gives $\Delta s^2 = \Delta x^2 + \Delta w^2$, so

$$\frac{\Delta s}{\Delta x} = \sqrt{1 + \left(\frac{\Delta w}{\Delta x}\right)^2}. \tag{2.12}$$

By considering the following expression and neglect the higher order term $(\Delta w/\Delta x)^4$,

$$\left[1 + \frac{1}{2}\left(\frac{\Delta w}{\Delta x}\right)^2\right]^2 = 1 + \left(\frac{\Delta w}{\Delta x}\right)^2 + \frac{1}{4}\left(\frac{\Delta w}{\Delta x}\right)^4 \approx 1 + \left(\frac{\Delta w}{\Delta x}\right)^2, \tag{2.13}$$

Equation 2.12 can be approximated as

$$\frac{\Delta s}{\Delta x} = 1 + \frac{1}{2}\left(\frac{dw}{dx}\right)^2. \tag{2.14}$$

The strain (Equation 2.11) of the small segment can also be approximated as

$$\epsilon' = \frac{1}{2}\left(\frac{dw}{dx}\right)^2. \tag{2.15}$$

The total strain of the entire panel is therefore obtained by integration,

$$\epsilon = \frac{1}{L_p}\int_0^{L_p} \epsilon' dx = \frac{1}{2L_p}\int_0^{L_p} \left(\frac{dw}{dx}\right)^2 dx. \tag{2.16}$$

Finally the nonlinear in-plane force can be obtained by substitute Equation 2.16 into Equation 2.10,

$$N_x = \frac{E_p h_p}{2L_p}\int_0^{L_p} \left(\frac{dw}{dx}\right)^2 dx. \tag{2.17}$$

The panel dynamic equation is solved using the standard finite-difference procedures. The panel is initially discretized into a series of meshes of constant size Δx. All spatial derivatives of the panel displacement are approximated using second-order central differences (Hayek 2011) as follows,

$$\frac{\partial w^{n,j}}{\partial x} = w_x^{n,j} = \frac{1}{2\Delta x}\left(w^{n+1,j} - w^{n-1,j}\right), \tag{2.18}$$

$$\frac{\partial^2 w^{n,j}}{\partial x^2} = w_{xx}^{n,j} = \frac{1}{\Delta x^2}\left(w^{n+1,j} - 2w^{n,j} + w^{n-1,j}\right), \tag{2.19}$$

$$\frac{\partial^4 w^{n,j}}{\partial x^4} = w_{xxxx}^{n,j} = \frac{1}{\Delta x^4}\left(w^{n+2,j} - 4w^{n+1,j} + 6w^{n,j} - 4w^{n-1,j} + w^{n-2,j}\right), \tag{2.20}$$

where the superscripts j and n indicate the j-th time step and n-th panel mesh point respectively. The time derivatives are calculated using the following approximations, with time step size Δt,

$$\frac{\partial w^{n,j}}{\partial t} = \dot{w}^{n,j} = \frac{1}{2\Delta t}\left(w^{n,j+1} - w^{n,j-1}\right), \tag{2.21}$$

$$\frac{\partial^2 w^{n,j}}{\partial t^2} = \ddot{w}^{n,j} = \frac{1}{\Delta t^2}\left(w^{n,j+1} - 2w^{n,j} + w^{n,j-1}\right), \tag{2.22}$$

Substituting all these approximations to Equation 2.9, the panel displacement is approximated as

$$w^{n,j+1} = \frac{4\rho_p h_p w^{n,j} + \left(-2\rho_p h_p + C\Delta t\right) w^{n,j-1} + 2\Delta t^2 B}{2\rho_p h_p + C\Delta t}, \tag{2.23}$$

where $B = p_{ex} + \left(T_x + N_x\right) w^{n,j}_{xx} - D w^{n,j}_{xxxx} - K_p w^{n,j}$. Therefore, after each time step the dynamics of all panel mesh points $\boldsymbol{W} = [w, \dot{w}, \ddot{w}]^\intercal$ are readily available.

2.3 Boundary conditions

2.3.1 Fluid domain

The boundary conditions for the fluid domain are prescribed as follows. Isothermal condition,

$$T = T_0, \tag{2.24}$$

is specified on all solid surfaces. Zero normal velocity $v = 0$ is applied for all rigid surfaces. The details of the treatment of the sliding wall boundary conditions in CE/SE method can be referred in the works of Lam et al. (2014a). For the fluid boundary in contact with the vibrating panel are required to satisfy the tangency condition (i.e. in y-direction),

$$v = \dot{w} + u w_x, \tag{2.25}$$

and the normal pressure gradient condition,

$$-\frac{\partial p}{\partial y} = \rho\frac{\partial v}{\partial t} + \rho u\frac{\partial v}{\partial x}, \tag{2.26}$$

to ensure the continuity of velocity and momentum, respectively, at the fluid-panel interface. However, the present study only focus on the effect of fluid inertia so the convective terms are ignored. In fact, this is only valid for low speed flow, i.e. when u is small. The inclusion of the convective terms will induces huge difficulty in the computation so its effects are left to future studies. The tangency and normal pressure gradient conditions become

$$v - \dot{w} = 0, \tag{2.27}$$

$$-\frac{\partial p}{\partial y} = \rho\ddot{w}. \tag{2.28}$$

The net pressure exerted on the panel surface can be found as,

$$p_{ex} = p_{\text{panel},b} - p_{\text{panel},a}, \tag{2.29}$$

where the pressure exerted on the identical side of panel,

$$p_{\text{panel},a} = p_a + \rho_a\ddot{w}^n\left(\delta_a - w^n\right), \tag{2.30}$$

and the opposite side of panel,

$$p_{\text{panel},b} = p_b - \rho_b\ddot{w}^n\left(\delta_b + w^n\right), \tag{2.31}$$

where δ is the offset of solution point from the panel surface without deflection as shown in Figure 2.5. If the fluid dynamics interact with the opposite side of the panel is considered as stationary in the calculation, $p_{\text{panel},b} = p_0$.

At each time step, the fluid domain should be deformed by the calculated panel displacement. Usually, remeshing (e.g. in So et al. (2003)) is applied to the deformed fluid domain so as to eliminate any highly strained mesh where

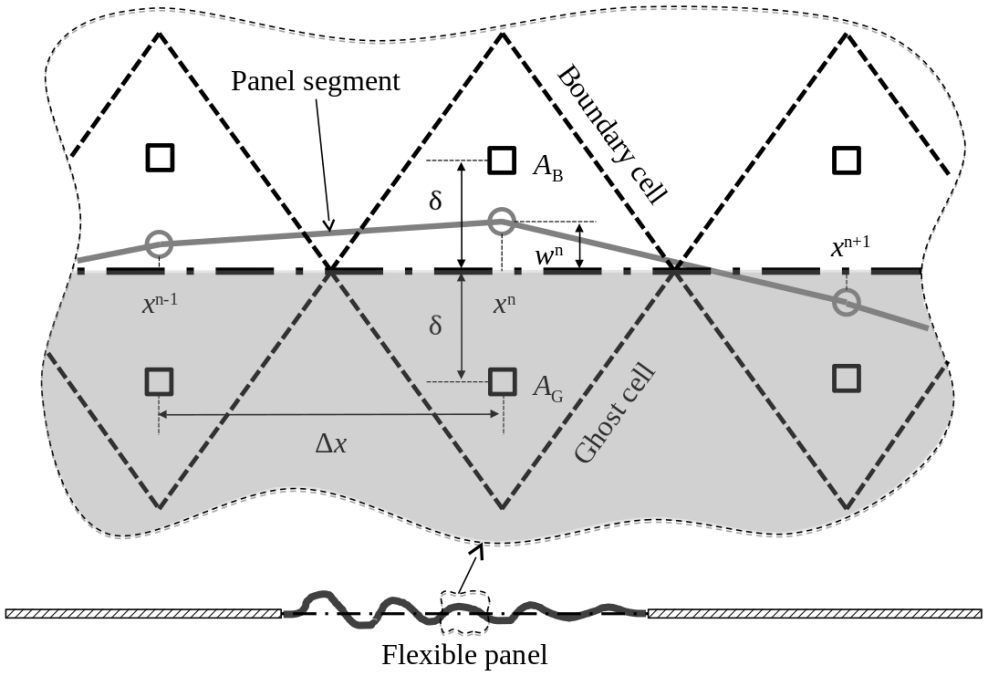

Figure 2.5: Meshes at fluid-panel interface. −·−·−, undeflected panel position; □, solution points of boundary cells and ghost cells of CE/SE mesh; ◯, panel mesh points.

the solution is underresolved. Otherwise, the solution accuracy will be seriously deteriorated. In the remeshing procedure, all mesh points in the fluid domain are updated so heavy computational resources are required. However, recognizing the characteristic feature in CE/SE method how the flow solution is calculated at solution points (Lam 2011) and assuming that panel displacements are very small compared to panel thickness, we can account for the effect of deformation of fluid domain with a much simpler technique that is derived in the spirit of immersed element boundary method (de' Michieli Vitturi et al. 2007).

Referring to Figure 2.5, the solution points are not laid on the physical fluid domain boundary in CE/SE method. The flow conditions at the boundary there are manifested by placing a mirror ghost cell behind the boundary, i.e. A_G. Appropriate flow variables are then specified at the ghost cell such that the desired flow conditions at the true panel position are implicitly given by interpolation with the boundary and ghost cells. For the rigid duct boundaries, the ghost point is set normal velocity $v_G = -v_B$ and its normal gradient $v_{x,G} = -v_{x,B}$ for enforcing zero normal velocity condition, where the subscript G and B represent the ghost and boundary cells respectively. It is also set tangential velocity $u_G = u_B$ and its tangential gradient $u_{y,G} = -u_{y,B}$ for enforcing sliding boundary condition. For the vibrating panel surfaces, the normal displacements of the panel can reach the order of h_p in the theory, but the tangential velocity can still be assumed to be negligibly small. Its displacement is assumed that smaller than the offset δ of solution point A_B and its normal velocity v_G can be approximated by the linear extrapolation with Equation 2.27,

$$\frac{v_G - \dot{w}^n}{\delta + w^n} = \frac{\dot{w}^n - v_B}{\delta - w^n}. \tag{2.32}$$

The derivatives of v_G and p_G in the normal direction, i.e. $v_{y,G}$ and $p_{y,G}$, are assumed same as the derivatives at the fluid-panel interface. Therefore, by Equa-

tion 2.28

$$p_{y,G} = -\rho_B \ddot{w}^n, \tag{2.33}$$

and by the first order finite difference approximation,

$$p_G = p_B - 2\delta p_{y,G}, \tag{2.34}$$

$$v_{y,G} = \frac{v_B - v_G}{2\delta}. \tag{2.35}$$

The density is determined by Equations 2.2 and 2.24, and its derivative can be approximated same as Equation 2.35. The setting of tangential velocity and its normal gradient are assumed same as the setting for a rigid surface. All tangential gradients are simply assumed $\boldsymbol{U}_{x,G} = \boldsymbol{U}_{x,B}$. The results in the forthcoming chapters show this assumption is acceptable. Therefore, all the flow variables in the ghost cell for isothermal, sliding flexible panel boundary is set by Equations 2.32 to 2.35, as

$$\begin{aligned}
&u_G = u_B, && u_{x,G} = u_{x,B}, && u_{y,G} = -u_{y,B},\\
&v_G = \dot{w}^n + \frac{\delta + w^n}{\delta - w^n}\left(\dot{w}^n - v_B\right), && v_{x,G} = v_{x,B}, && v_{y,G} = \frac{v_B - v_G}{2\delta},\\
&p_G = p_B - 2\delta\rho_B \ddot{w}^n, && p_{x,G} = p_{x,B}, && p_{y,G} = \rho_B \ddot{w}^2,\\
&\rho_G = \frac{\gamma p_G C_1}{T_0}, && \rho_{x,G} = \rho_{x,B}, && \rho_{y,G} = \frac{\rho_B - \rho_G}{2\delta}.
\end{aligned}$$

Certainly, the validity of the assumption had been checked during the course of calculations. For a panel displacement larger than the offset of solution point (i.e. $w > \delta$), this extrapolation method is not physically valid. In the fluid model, the CE/SE solver relies on applying the conservation law in each small control volume (i.e. CE) and the calculation of the flux through the surface of those control volume. The solution points at those volume surfaces are used to provide information for flux calculation. If $w > \delta$, that solution point does not physically exist. The corresponding control volume will be destroyed and the

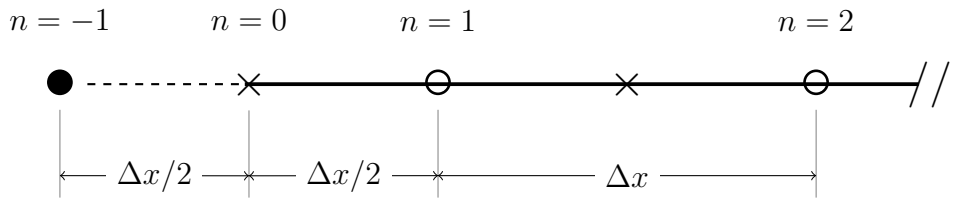

Figure 2.6: Boundary segment of undeflected panel. ×, mesh nodes; ○, solution points; ●, a ghost point; ——, the panel segment.

flux calculation cannot be completed. Therefore the solver will give wrong result in this situation. Other more complex but proper technique, such as immersed element boundary method or remeshing procedure, must be used. In all the calculations reported in the next chapter, $w/\delta < 68\%$ consistently. This observation indicates that our proposed simplified technique works well for the present study.

2.3.2 Flexible panel

The panel and the fluid domain are sharing the same mesh, and all panel solution points are located below the row of CE/SE solution points just next to boundary of the fluid domain as Figure 2.5. Therefore, there no panel solution point is directly located at the panel edge as shown as Figure 2.6. To approximate the forth-order spatial derivative by second-order central differences, there must have four adjacent points, which two at positive and two at negative sides, for each solution point. However, there are not enough adjacent points for the boundaries $n = 1$ and n', where n' is the total number of panel solution points. Therefore, one ghost point is added to each panel end as Figure 2.6. Two ghost points are denoted as $n = -1$ and $n = n' + 2$; and two boundary nodes are denoted as $n = 0$ and $n = n' + 1$.

Pinned or clamped conditions can be applied at the edges. For the pinned-pinned ends, the displacement and bending moment should be set as zero at the

boundary nodes,

$$w^{0,j} = w^{n'+1,j} = w^{0,j}_{xx} = w^{n'+1,j}_{xx} = 0. \tag{2.36}$$

Hence,

$$w^{-1,j} = -w^{1,j}, \qquad w^{n'+2,j} = -w^{n',j}. \tag{2.37}$$

If clamped-clamped ends are used, the displacement and slop should be set as zero,

$$w^{0,j} = w^{n'+1,j} = w^{0,j}_{x} = w^{n'+1,j}_{x} = 0. \tag{2.38}$$

Hence,

$$w^{-1,j} = w^{1,j}, \qquad w^{n'+2,j} = w^{n',j}. \tag{2.39}$$

By using the Taylor series, the second-order spatial derivatives are given by

$$w^{1,j}_{xx} = \frac{1}{\Delta x^2}\left(-4w^{1,j} + \frac{4}{3}w^{2,j}\right), \qquad w^{n',j}_{xx} = \frac{1}{\Delta x^2}\left(-4w^{n',j} + \frac{4}{3}w^{n'-1,j}\right); \tag{2.40}$$

and the forth-order spatial derivatives are given by

$$w^{1,j}_{xxxx} = \frac{1}{\Delta x^4}\left(C'w^{1,j} - 8w^{2,j} + \frac{8}{5}w^{3,j}\right), \tag{2.41}$$

$$w^{2,j}_{xxxx} = \frac{1}{\Delta x^4}\left(-8w^{1,j} + 8w^{2,j} - \frac{24}{5}w^{3,j} + \frac{8}{7}w^{4,j}\right), \tag{2.42}$$

$$w^{n',j}_{xxxx} = \frac{1}{\Delta x^4}\left(C'w^{n',j} - 8w^{n'-1,j} + \frac{8}{5}w^{n'-2,j}\right), \tag{2.43}$$

$$w^{n'-1,j}_{xxxx} = \frac{1}{\Delta x^4}\left(-8w^{n',j} + 8w^{n'-1,j} - \frac{24}{5}w^{n'-2,j} + \frac{8}{7}w^{n'-3,j}\right), \tag{2.44}$$

where $C' = 16$ for pinned-pinned ends, or $C' = 32$ for clamped-clamped ends.

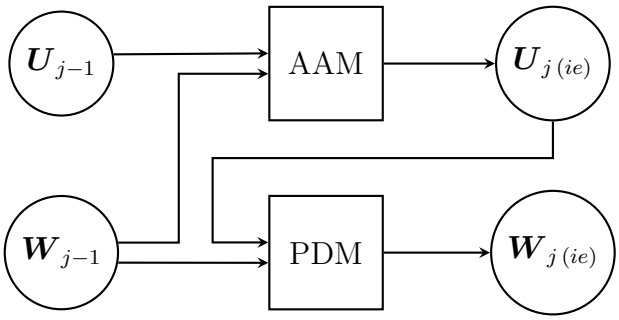

Figure 2.7: Calculation procedure of the staggered coupling scheme (or initial estimation procedure of the iterative coupling scheme). AAM, aeroacoustical model; SDM, structural dynamic model.

2.4 Partitioned fluid-panel coupling scheme

When an unsteady flow and an acoustic wave are passing over the flexible panel, the flow pressure fluctuations acting on the panel will force to vibrate. The vibrating panel then modifies the boundary condition of the aeroacoustic flow which has to change as a consequence. The aeroacoustic field and the panel structural response are coupled to each other through two key conditions: the tangency boundary condition (Equation 2.27) which is the effect of structural response on the unsteady flow, and the normal pressure gradient condition (Equation 2.28) which is the effect of flow unsteadiness on the structural response. Therefore, a coupling scheme that allows seamless coupling of both effects is necessary for the accurate prediction of the flow-panel interaction involved. Generally, both the staggered and iterative coupling schemes were selected by different researchers depends on the accuracy requirement of their problems. Both schemes are described in the following.

2.4.1 Staggered coupling scheme

The first scheme attempted is schematically illustrated in Figure 2.7. In this scheme, the panel structural dynamic solution $\boldsymbol{W}_{j-1}$ available at the end of the

$(j-1)$-th time step is treated as the boundary condition of the fluid domain in contact with the panel for the solver of aeroacoustic model for calculating the new aeroacoustic solution at the j-th time step, i.e. $\boldsymbol{U}_j$. Then the new panel structural response $\boldsymbol{W}_j$ is evaluated by solving Equation 2.23 with its forcing term, i.e. p_{ex}, constructed from the aeroacoustic solution $\boldsymbol{U}_j$ (refer to Equation 2.29). Both $\boldsymbol{U}_j$ and $\boldsymbol{W}_j$ available at the end of the j-th time step are then used as the initial solutions for the $(j+1)$-th time step and the solution of the problem marches in time afterward. As such in each time step, the update of the panel structural response appears to lag that of the aeroacoustic solution. This feature leads to the enforcement of the tangency condition and the normal pressure gradient condition in a staggered manner. Thus the communication between the two solutions is literally one-way, so the scheme can be considered to resolve the fluid-panel interaction in a loose coupling sense. The numerical error arising from the delay between the updates of aeroacoustic and structural dynamic solutions can be effectively suppressed with the reduced time step size (Jaiman et al. 2011). Since a small time step size is always needed for the present explicit CE/SE aeroacoustic solver (Lam et al. 2014a), especially in the case with a low Mach number flow, the scheme appears to be a reasonable choice for solving the present problem.

2.4.2 Iterative coupling scheme

This scheme follows the idea of Jadic et al. (1998) which emphasizes more on the two-way coupling between the aeroacoustic and structural dynamic solutions. It can be divided as two parts: initial estimation and predictor-corrector procedure. In the calculation at the j-th time step, initial solution estimates, $\boldsymbol{U}_{ie}$ and $\boldsymbol{W}_{ie}$ are firstly evaluated in the same way as described in the staggered coupling scheme (Figure 2.7). The initial estimates are then put into the predictor-corrector pro-

cedure, as Figure 2.8, in which the errors in the satisfaction of both tangency and normal pressure gradient conditions are minimized in an iterative manner. Essentially, an aeroacoustic solution estimate $\boldsymbol{U}_{k+1}$ is obtained with an predicted boundary condition $\lambda \boldsymbol{W}_k + (1-\lambda)\boldsymbol{W}_{k-1}$, where λ is the relaxation factor (Anderson et al. 1984). Then the estimated $\boldsymbol{W}_{k+1}$ is obtained with an predicted forcing from $\lambda \boldsymbol{U}_{k+1} + (1-\lambda)\boldsymbol{U}_k$. If the relative errors between the solutions at iterations k and $k+1$ at all panel mesh points is less than the prescribed precision ε, i.e.

$$\frac{|\boldsymbol{U}_{k+1} - \boldsymbol{U}_k|}{|\boldsymbol{U}_{k+1}|} < \varepsilon, \tag{2.45}$$

$$\frac{|\boldsymbol{W}_{k+1} - \boldsymbol{W}_k|}{|\boldsymbol{W}_{k+1}|} < \varepsilon, \tag{2.46}$$

then the final solutions $\boldsymbol{U}_j = \boldsymbol{U}_{k+1}$ and $\boldsymbol{W}_j = \boldsymbol{W}_{k+1}$ are marched forward to next time step; otherwise the iteration continues until the precision requirement is reached. Since the effects of aeroacoustics on the panel structural dynamics and its vice versa are accounted for in the solution in equal footing, the procedure described leads to a more tightly coupled scheme for resolving the fluid-panel interaction. Nevertheless the computational resources incurred is heavier. In all the calculations reported in the this thesis and computed by the procedure described, λ is set equal to 0.5 whereas the precision requirement ε is prescribed to 10^{-10}, and the number of iterations in each time step is around 18. The performance of the iteration procedure is discussed in Section 4.3 and Table 4.2.

2.5 Validation for in-vacuo and fluid loaded panel vibration

Lam et al. (2014a) already validated that the aeroacoustic model is capable of resolving the aeroacoustic interactions in low subsonic to supersonic Mach numbers accurately through comparisons with the existing results of the benchmark

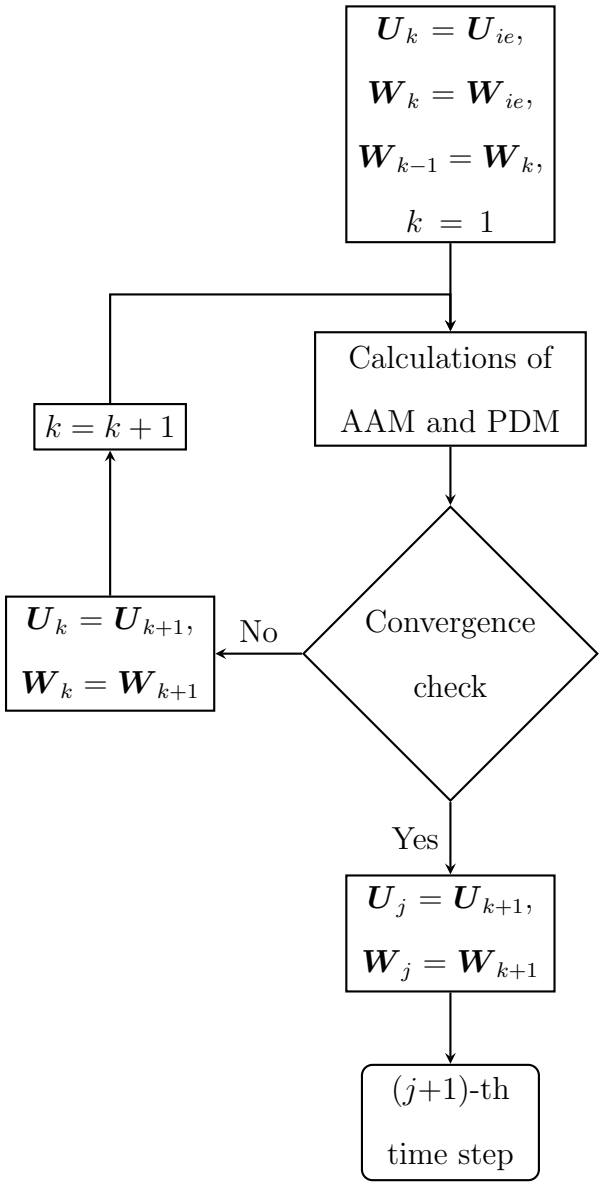

Figure 2.8: Predictor-corrector procedure of the iterative coupling scheme where k is iteration index.

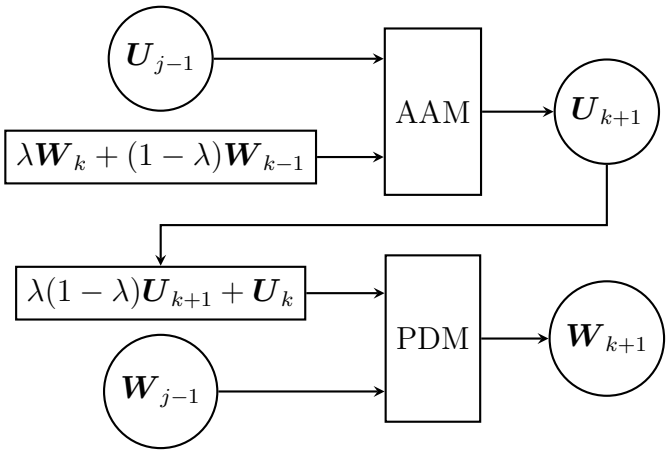

Figure 2.9: Calculation procedures of the block marked with "Calculations of AAM and PDM" in Figure 2.8.

aeroacoustic problems with increasing complexity. Therefore, the forthcoming validations focus on the panel vibration and the fluid-structure interaction. The validations of the aforementioned solvers for the basic problems, i.e. in-vacuo and fluid loaded panel vibration, are presented in this section. Comparison with the theory of other more complicated problems, such as acoustics-structure interaction, are discussed with other results in other chapters. The first step of the validation is to assess the panel dynamic model. The theoretical solution of a in-vacuo finite membrane with pinned-pinned ends is well established, the eigenmode shape and frequency in one-dimension are known as (Blevins 1979),

$$w(x) = A_N \sin N\pi x, \tag{2.47}$$

$$f_{vacuum,N} = \frac{N}{2}\sqrt{\frac{T_x}{\rho_p h_p}}, \tag{2.48}$$

where N is the mode number and A_N is the modal amplitude. For comparison, some eigenmode vibrations are tested numerically. In this case, the panel dynamic model is decoupled from the aeroacoustic model as the net pressure p_{ex} is set as constant zero. An undamped ($C = 0$) finite membrane ($D = 0$) with 100 elements and pinned-pinned ends is applied. The material properties are

Table 2.1: Comparisons between numerical and theoretical in-vacuo eigenmode frequencies.

N	$f_{vacuum,N}$	D_f
1	0.05	0.05 %
2	0.1	0.25 %
3	0.15	0.39 %
7	0.35	0.52 %
10	0.5	0.74 %

set as $T_x = 0.00128$ and $\rho_p h_p = 0.128$, so $f_{vacuum,N} = 0.05N$ based on Equation 2.48. A certain eigenmode shape (Equation 2.47) is set as the initial condition of the membrane, and let it free vibrate as the prescribed eigenmode when $t > 0$. Five eigenmodes are tested and the comparisons are shown in Table 2.1, the relative difference between numerical and theoretical results is determined by $D_f = |f_N - f_{vacuum,N}|/f_{vacuum,N}$. The maximum difference is only 0.74 %, so the panel dynamic model strongly agrees with the theory.

Since the panel dynamic model is validated, the fluid loading should be included in the next step. When the panel is moving, an oscillating fluid force is induced that applied by the surrounding fluid to the panel. Because of the fluid and the panel are in contact, the fluid surrounding the panel must accelerate as well as the panel accelerates. The inertia generated by this fluid motion is called added mass, that can be considered as an additional mass attach to and move with the panel (Blevins 1979). The added mass, M_{added} of a finite panel with pinned-pinned ends can be predicted from potential flow theory as (Dugundji et al. 1963),

$$M_{added} = \frac{\rho}{N\pi}. \tag{2.49}$$

Table 2.2: Comparisons between numerical and theoretical fluid loaded eigenmode frequencies.

N	$f_{fluid,N}$	D_f	
		Staggered coupling	Iterative coupling
3	0.111	6.88 %	6.88 %
7	0.301	4.32 %	4.38 %
10	0.447	0.20 %	0.19 %

The added mass always decreases the eigenmode frequency as the effective mass of the panel increase. Since the eigenmode frequency is inversely proportional to the square root of the mass of the membrane, which can be refer to Equation 2.48, the ratio of the frequency of the membrane in a vacuum to the membrane immersed in a fluid can be found as (Blevins 1979),

$$\frac{f_{fluid,N}}{f_{vacuum,N}} = \left(1 + \frac{M_{added}}{\rho_p h_p}\right)^{-\frac{1}{2}}. \tag{2.50}$$

Five eigenmodes with the same numerical setting and material properties for the membrane like the in-vacuo tests are carried out. However, this time the coupling between aeroacoustic and panel dynamic models is applied and Euler equations are used because the fluid is assumed inviscid. The fluid loaded eigenmode frequency can be determined by Equations 2.49 and 2.50, but the added mass is halved because fluid loading is calculated for one side of the membrane in these cases, another side is stationary. Both staggered and iterative coupling schemes are tested and compared in Table 2.2. Two coupling schemes have similar results. The maximum difference to the theory is 6.9%. However, Dugundji et al. (1963) showed that the theoretical approximation also have maximum 6% error compared to the experimental data. Therefore the numerical results have acceptable agreement with the theory. Besides, the lower mode has larger difference. This

may because the added mass of lower mode is lager. The error of the ratio of added mass and panel mass should be larger in the theoretical approximation too. Therefore the difference in frequency will be larger. Since two coupling schemes have similar accuracy in this test, their comparison will be continued for other cases in the next chapter.

Chapter 3

Aeroacoustic-Structural Interaction in Duct Carrying Inviscid Flow

To assess the accuracy of the numerical methodology, the work by Huang (1999) is selected as our canonical problem to compare with his frequency-domain theoretical results with single frequency excitation. Besides, any physics that could not be captured in the theory is further uncovered and discussed in the meantime. After the discussion on the aeroacoustic-structural response with a single frequency excitation, the effect of excitation frequencies will be further discussed by investigate the similar problem exposed to broadband excitation.

3.1 Single frequency excitation

3.1.1 Acoustic-structural interaction

Huang (1999) proposed to flush-mount a finite length tensioned flexible panel in an infinite rigid flow duct, as shown as Figure 3.1, for controlling low-frequency

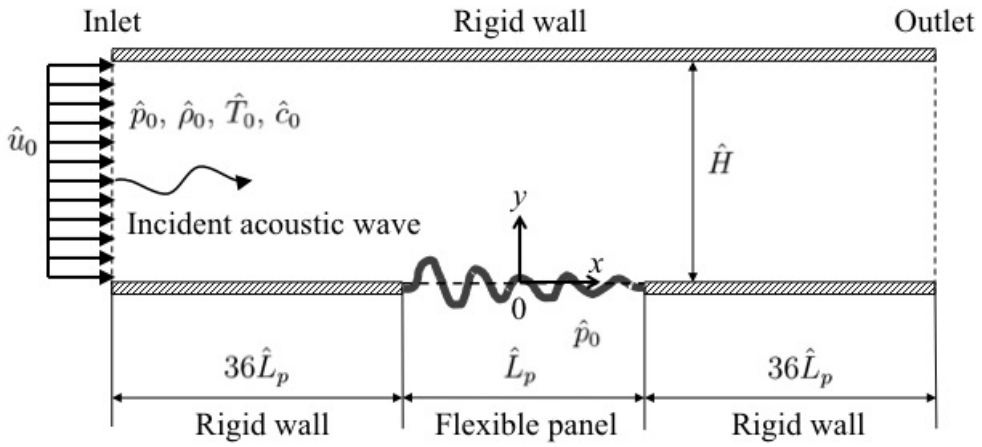

Figure 3.1: Schematic configuration of a finite length tensioned flexible panel flush-mounted in an infinite rigid flow duct (not-to-scale).

duct noise in his work. When a plane acoustic wave is propagating through the duct, the panel responds to vibrate and the local distension in the vicinity of the panel thus created renders a local wave propagation speed far less than its isentropic value. The mismatch in the wave speed there leads to reflection and scattering of the acoustic wave at the edges of the panel. The extent of reflection and scattering depends on the acoustic-structural interaction occurring with the vibrating panel which eventually results in creates passbands and stopbands for the acoustic transmission. Assuming harmonic fluctuations and quasi one-dimensional variation along the duct for all dynamic quantities, Huang presented a detailed linear analysis in frequency-domain of how various panel parameters (e.g. length, stiffness, structural damping, etc.) influence the panel acoustic-structural interaction and subsequently the transmission loss in the duct in case there is no flow. His results of the analysis are complete and provide a set of good reference for validating the numerical methodology.

In this regard a same set of problem parameters Huang (1999) studied is taken, i.e. the duct width $\hat{H} = 100$ mm, panel density $\hat{\rho}_p = 1000$ kg/m^3, the

panel thickness $\hat{h}_p = 0.05$ mm, the tension $\hat{T}_x = 58.0601$ N/m, the frequency of incident wave $\hat{f} = 340$ Hz and the mean flow speed $\hat{u}_0 = 0$ m/s. $\hat{L}_0 =$ panel length $\hat{L}_p$, ambient acoustic velocity $\hat{c}_0 = 340$ m/s, time $\hat{t}_0 = \hat{L}_0/\hat{c}_0$, ambient density $\hat{\rho}_0 = 1.225$ kg/m^3, ambient pressure $\hat{\rho}_0\hat{c}_0^2$, and ambient temperature $\hat{T}_0$ are chosen for the normalization of all flow and panel variables. The frequency of the incident wave $\hat{f}$ used is fixed at 340 Hz which becomes $f = 0.1L_p/H$ after normalization. The computational domain is illustrated in Figure 3.1. The duct sections upstream and downstream of the flexible panel are set equal to $36L_p$ so as to ensure sufficient space for the generated acoustic waves to propagate. Euler equations have been solved in this calculation because the flow in the problem is assumed inviscid.

Before the actual calculations, the mesh and time step convergence need to be established. Three mesh designs are established with different mesh density. A summary of different mesh designs on the fluid domain and the panel is given in Table 3.1. One should note that finer mesh sizes are adopted in the vicinity of the panel in order to suppress the contamination of the truncation errors on the fine details of calculated aeroacoustic-structural interaction as much as possible. The coarser mesh sizes in the rigid duct sections are so selected that the acoustic wave propagation with the fastest mean flow of interest (i.e. $M = 1.2$) can be correctly calculated, yet it does not make the time for calculations prohibitively long. By following the approach given in Lam et al. (2014b), the time step size is set and the Courant-Friedrichs-Lewy number is fixed for all mesh designs. The case $L_p/H = 5$ and $M = 0$ is selected for the mesh convergence check with the time-stationary solution. Figure 3.2 shows the sensitivity of the resolved temporal change of the total acoustic pressure and the panel vibration mobility, $Y_x = (\dot{w}(x))_{rms}/(p'_{inc})_{rms}$, under the acoustic-structural interaction. Evidently, the variation decreases with the mesh size. The maximum deviations in the

Table 3.1: Mesh designs. The mesh stretching function, $F_i\left(\Delta x_{min}, \Delta x_{max}, N_i\right) = 0.5\left(\Delta x_{max} - \Delta x_{min}\right)\left\{\tanh\left\{9\left[(i-1)/(N_i-1) - 0.5\right]\right\} + 1\right\} + \Delta x_{min}$ where Δx_{min} and Δx_{max} are the minimum and maximum mesh sizes, N_i is number of meshes required, and $i = 1, 2, ..., N_i$ is the mesh index.

	For $-0.5 \leq x \leq 0.5$	For $-0.6 \leq x < -0.5$ and $0.5 < x \leq 0.6$
Mesh I	$\Delta x = 0.004$	$\Delta x_i = F_i(0.004, 0.02, 12)$
Mesh II	$\Delta x = 0.002$	$\Delta x_i = F_i(0.002, 0.01, 22)$
Mesh III	$\Delta x = 0.001$	$\Delta x_i = F_i(0.001, 0.005, 46)$

	For $-1.3 \leq x < -0.6$ and $0.6 < x \leq 1.3$	For $x < -1.3$ and $x > 1.3$
Mesh I	$\Delta x_i = F_i(0.02, 0.1, 13)$	$\Delta x = 0.1$
Mesh II	$\Delta x_i = F_i(0.01, 0.05, 24)$	$\Delta x = 0.05$
Mesh III	$\Delta x_i = F_i(0.005, 0.025, 50)$	$\Delta x = 0.025$

	For all x	
Mesh I	$\Delta y = H/50$	$\Delta t = 0.0005$
Mesh II	$\Delta y = H/50$	$\Delta t = 0.00025$
Mesh III	$\Delta y = H/50$	$\Delta t = 0.000125$

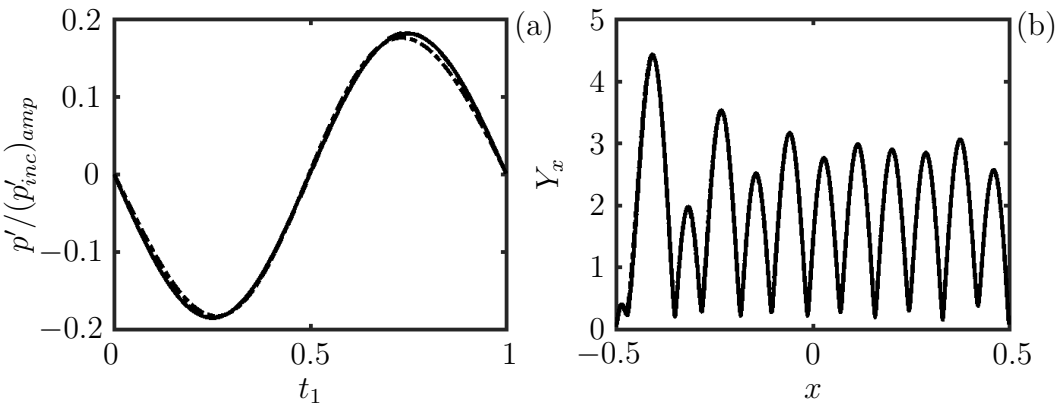

Figure 3.2: Sensitivity of numerical solutions to mesh size. (a) Time traces of total acoustic pressure. (b) Panel mobility. $-\cdot-\cdot-$: Mesh I; ——: Mesh II; – – –: Mesh III.

pressure and mobility obtained from switching from Mesh I to Mesh II are 2.3% and 0.61% respectively. Upon switching from Mesh II to Mesh III the maximum deviations further reduce to 0.055% and 0.25% respectively. Therefore, the Mesh II is selected for all calculations discussed in forthcoming discussions.

3.1.1.1 Acoustic response

Huang (1999) showed that an excited vibrating panel in duct reflects and scatters the incident acoustic wave p'_{inc} in the absence of mean flow. He assumed the total panel pressure, the force felt by the panel form the fluid, is the summation of the simple harmonic temporal and spacial dependant incident wave and the re-radiation p'_{rer} generated by the excited panel itself. The pressure perturbation induced by the panel oscillation was calculated by the theory of Doak (1973). The panel oscillation was considered as a number of vibrating pistons flush-mounted in the duct wall, and they vibrated at the same frequency. Each vibrating piston is treated as a point acoustic source of simple harmonic temporal dependence. Therefore the pressure perturbation induced by panel oscillation can be deter-

mined by the inhomogeneous wave equation, and the solution can be constructed as a linear superposition of contributions from each of the characteristic duct modes and the point sources. Since the total panel pressure was given, the panel vibration can be determined by membrane equation with external pressure. The equation was solved in frequency/axial mode domain, and sine transform was selected to satisfy the panel boundary conditions which were the simply supported ends. Under this theory, the total pressure perturbation, $p' = p - \bar{p}$, in the duct can be imagined as the superposition of incident and re-radiation waves,

$$p' = p'_{rer} + p'_{inc}. \tag{3.1}$$

The re-radiated wave destructively interfere with the incident wave downstream of the panel and results in a net reduction of transmitted acoustic energy as a result of the acoustic-structural interaction. The energy reduction also depends on whether the panel is structurally damped or not. Huang claimed such phenomena can be utilized for the development of a new breed of the design of duct silencer across which the flow pressure drop is very low. The performance of the silencer design is described by the transmission loss TL defined as

$$TL = -20 \log_{10} \left| \frac{p'_{inc} + p'_{rer}}{p'_{inc}} \right|. \tag{3.2}$$

The TL with different panel lengths $L_p/H = 4.3$, 6 and 8, and without structural damping ($C = 0$) are calculated by using both staggered and iterative coupling schemes. Since the panel length is chosen as the reference length, the effects of L_p/H variation are calculated here through modifying the value of duct width H. This is different from the notation adopted in the theory where H is fixed but L_p varies. However this change of scaling does not affect the accuracy of the numerical results. In general situation, any fluid variable contains the fluctuations from the incident and re-radiated waves. The p'_{rer} cannot be determined directly from the numerical results with the flexible wall. Therefore, in addition

Table 3.2: Comparisons between theoretical (Huang 1999) and numerical TL by staggered and iterative coupling schemes at various L_p/H. The values in brackets are ΔTL.

L_p/H	4.3		6		8	
Theory	2.1		2.1		15.0	
Staggered scheme	4.4	(2.3)	1.1	(−1.0)	14.2	(−0.8)
Iterative scheme	3.0	(0.9)	1.3	(−0.8)	14.7	(−0.3)

to each actual calculation, an additional one is calculated in a synchronized manner on the propagation of p'_{inc} only within a rigid duct of the same size. Then the rigid duct results are subtracted from the results with flexible wall to obtain the p'_{rer}. The temporal evolutions of p'_{inc} and p' at locations $20L_p$ upstream and downstream respectively of the panel are recorded over one incident wave cycle for each calculation of TL. The locations are so selected that any higher-order duct mode, if generated from the panel, decays completely and only plane waves can be detected. This requirement is consistent with the quasi one-dimensional propagation assumed in theory. Their root-mean-squared values are evaluated and substituted into Equation 3.2 for the calculation of TL. A comparison of the numerical TL with the corresponding theoretical values and their difference $\Delta TL = TL_{numerical} - TL_{theoretical}$ are given in Table 3.2. In general $|\Delta TL|$ reduces as L_p/H increases. The iterative coupling scheme appears to perform better than the staggered coupling scheme for all cases attempted. The difference in the numerical result is particularly pronounced for a short panel ($L_p/H = 4.3$) where the $\Delta TL = 2.3$ db for staggered coupling scheme but $\Delta TL = 0.9$ db for the iterative coupling scheme. All these observations reveal that the iterative coupling scheme is more superior in capturing the fluid-panel interaction. Furthermore, a

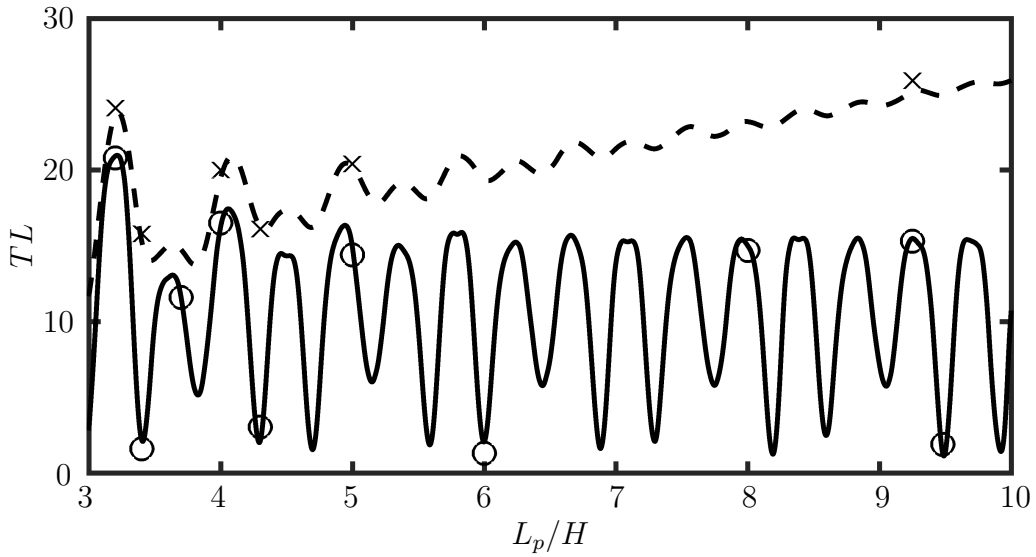

Figure 3.3: Variation of transmission loss TL with panel length L_p/H. ——, theoretical result (Huang 1999) with undamped panel; – – –, theoretical result with damped panel; ◯, numerical result with undamped panel; ×, numerical result with damped panel.

careful check shows that additional time spent in iterative coupling scheme takes approximately 30% of that used in the staggered coupling scheme. However, the accuracy of the iterative scheme is much better than the staggered scheme so the iterative scheme is employed for all subsequent calculations.

A more comprehensive assessment of the numerical methodology with the iterative scheme is illustrated in Figure 3.3 with the corresponding theoretical predictions (Huang 1999). The theoretical predictions of TL for an undamped panel behaves more or less an approximate regular function with L_p/H with its minimum values close to 0 db. For the damped panel, the general trend of TL is increasing linearly with the panel length. The structural damping effectively reinforces the TL for the long panel. In the frequency-domain analysis of Huang (1999), he expanded the panel dynamics into the summation of N sinusoidal in-vacuo panel velocity eigenmodes and calculated the temporal variations of

Table 3.3: Deviation ΔTL of numerical results from theory (Huang 1999) in all cases in Figure 3.3.

L_p/H	ΔTL	
	$C = 0$	$C = 0.0196$
3.2	-0.1	0.5
3.4	-0.7	0.1
3.7	0.0	—
4	0.3	0.6
4.3	0.9	-0.1
5	-0.2	0.1
6	-0.5	—
8	-0.3	—
9.25	-0.2	0.8
9.48	0.6	—

the modal coefficients for the panel response. The m-th panel modal damping coefficient can be estimated as

$$C = N\bar{C}\sqrt{T_x \rho_p h_p}, \tag{3.3}$$

where $\bar{C}$ is a function of material property. For the present time domain analysis, the same damping coefficient cannot be directly applied. Instead, the dominant mode of undamped solution is determined first. Then the dominant mode number N is substituted in Equation 3.3 to find the value of C. Huang chose $\bar{C} = 0.2$ which gives $C = 0.0196$ in the present study. A summary of the deviation ΔTL of numerical results from theory in Table 3.3 shows that the largest deviation observed is less than 1 db. It indicates that the present numerical methodology is able to capture the acoustic-structural interaction accurately.

Two extreme cases with different panel length in Figure 3.3 are chosen as examples to study the temporal evolution of the acoustic pressure fluctuations for the better understanding of the effect of the re-radiation of both undamped ($C = 0$) and damped ($C = 0.0196$) panel. The first one is $L_p/H = 3.2$ which is the highest TL; the another one is a low TL case, $L_p/H = 3.4$. These two cases have been chosen because their TL are extremely different but panel length is merely extended 6.2%. Figure 3.4 shows acoustic responses with undamped and damped panel of $L_p/H = 3.2$. The temporal evolution of acoustic pressure fluctuation along the duct centerline, that is $p'(x,t)/(p'_{inc})_{amp}$ at $y = 0.15625$, with undamped panel within one incident wave period $t_1 = 1/f$ is shown in Figure 3.4(a). The record starts at the moment when a maximum $p'_{inc}/(p'_{inc})_{amp}$ hits the leading edge of the panel. Within two dash-lines is denoted as the area above the panel, that is the acoustic-structural interaction happens in it. Therefore the negative and positive sides outside the interaction area are regarded as upstream and downstream respectively. A standing wave, which nodes are located at $x = -1.79$ and -3.34, appears in the upstream because the incident wave superimposed with a strong reflection from the interaction area. In the meantime, the wave in the downstream is very weak as hard to be noticed in the figure. Upon exposure to the incident wave, the panel responds to vibrate and alter the acoustic wave propagation in the duct. Figure 3.4(c) shows the re-radiated wave $p'_{rer}(x,y,t)/(p'_{inc})_{amp}$ at $y = 0.15625$, which is the effect of panel vibration to the acoustics field. The re-radiation appears to start at around $x = -0.3$ which close to the leading edge of the panel. The upstream p'_{rer} is equal to the reflected wave, and the amplitude is almost same as the incident p'_{inc}. The two waves superimpose to form a complete standing wave in Figure 3.4(a). The downstream p'_{rer} has a weaker amplitude only 93% of the p'_{inc}. It propagates the same direction with the incident wave and causes a strong destructive interference, which results

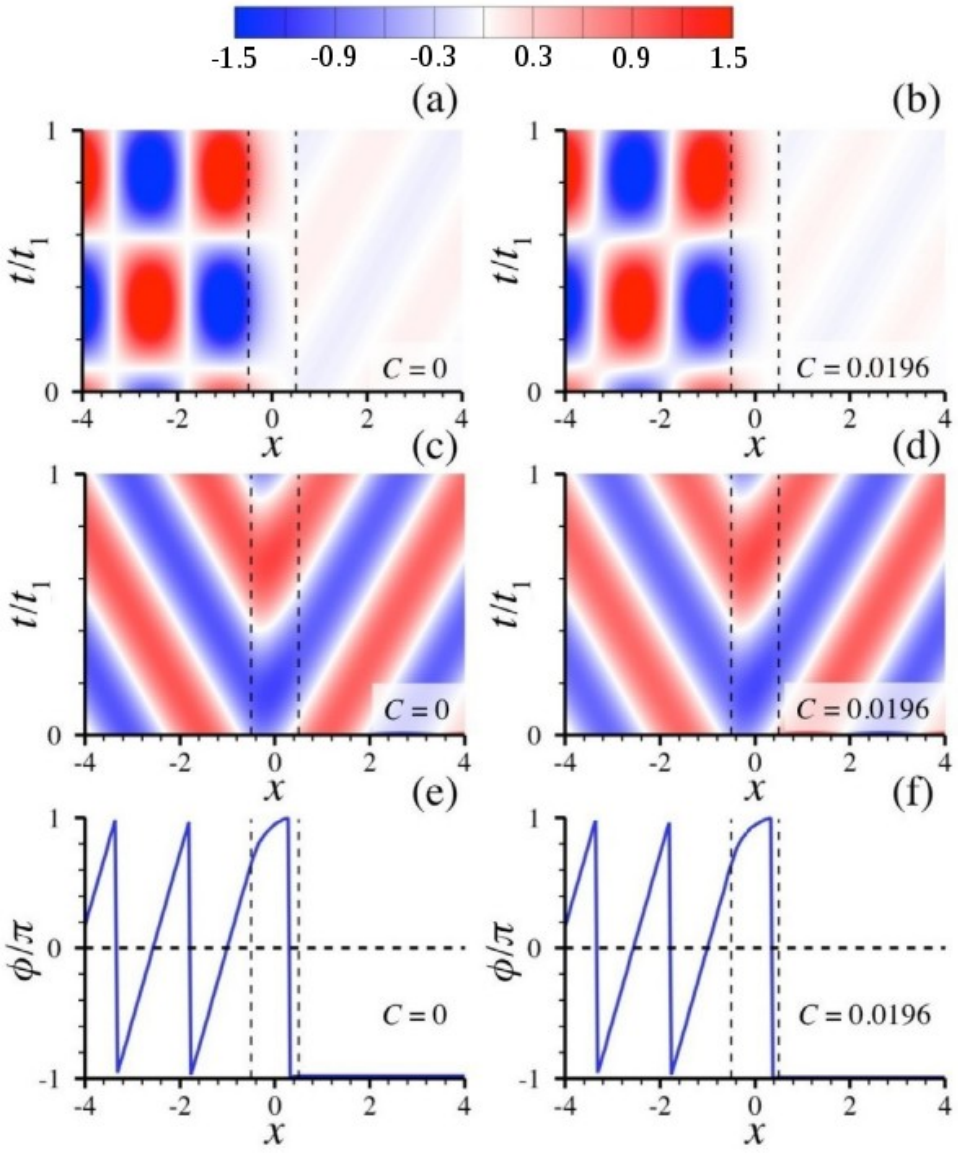

Figure 3.4: Acoustic response along the centerline of the duct with $L_p/H = 3.2$ within one incident wave period t_1. (a) & (b), the total fluctuation pressure $p'/(p'_{inc})_{amp}$; (c) & (d), the re-radiated waves $p'_{rer}/(p'_{inc})_{amp}$; (e) & (f), the phase shift of re-radiated wave relative to the incident wave. – – –, panel edges.

in a weak transmitted wave. The effectiveness of the interference is related to the phase difference between two waves. The phase shifts ϕ of the re-radiated wave relative to the incident wave of each location x along the duct center line is shown in Figure 3.4(e). In the upstream, p'_{inc} and p'_{rer} propagate in different direction, thus ϕ changes continuously with x. The ϕ is adjusted to the panel which eventually settles to a value close to -0.98π after passing $x = 0.34$ close to the panel trailing edge. It gives rise to an effective destructive interference along the duct and results in a high $TL = 20.9$ db. The $p'(x,t)/(p'_{inc})_{amp}$, $p'_{rer}(x,t)/(p'_{inc})_{amp}$ and $\phi(x)$ with structural damping are also shown in Figures 3.4(b), (d) and (f). Compare to the undamped case, the difference is not large. The amplitudes of the upstream and downstream p'_{rer} are reduced to 89% and 94% of the incident wave. The energy loss should be dissipated by the structural damping. Although the downstream p'_{rer} is reduced, the ϕ is adjusted to -0.99π that promotes the destructive interference. Two effect sum up enhance the TL to 24.1 db, that is 3.3 db increment of the undamped one. It indicated that the ϕ plays a more important role in this situation.

The same analysis for low TL case, $L_p/H = 3.4$, is operated. Figure 3.5(a) show the p' has a partial standing wave forms in the upstream, which the nodes are shifted towards the panel to $x = -1.49$ and -2.94. Stronger wave also appears in the downstream compared to the case with $L_p/H = 3.2$. These changes are attributed to the p'_{rer}. Figure 3.5(c) shows it has a strong preference towards downstream. The amplitude of the upstream propagation is only 50% of the incident. However, the downstream propagation is 138% of the incident and begins approximately at $x = 0.1$ that is close to the center of the panel. The ϕ in downstream is also changed to a higher value, that is -0.8π shown in Figures 3.5(e). These changes altogether destroy the destructive interference in the downstream duct section effectively so the TL is reduced sharply to only 1.8 db (Figure 3.3).

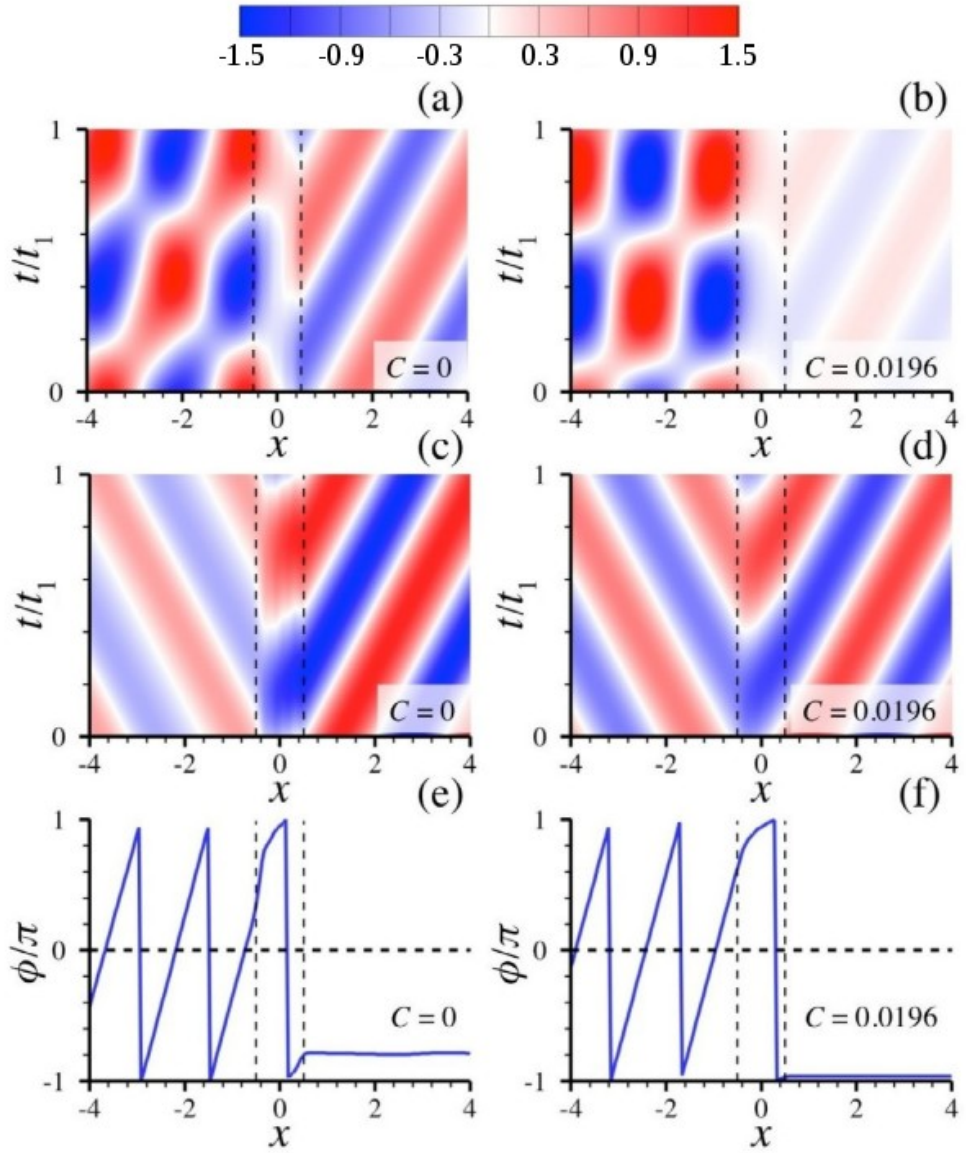

Figure 3.5: Acoustic response along the centerline of the duct with $L_p/H = 3.4$ within one incident wave period t_1. (a) & (b), the total fluctuation pressure $p'/(p'_{inc})_{amp}$; (c) & (d), the re-radiated waves $p'_{rer}/(p'_{inc})_{amp}$; (e) & (f), the phase shift of re-radiated wave relative to the incident wave. – – –, panel edges.

When the structural damping is included, p'_{rer} propagation preference towards downstream is reduced and the ϕ goes back to -0.97π as shown as Figures 3.5(d) and (f). The amplitudes of upstream and downstream p'_{rer} are 74% and 112% of the incident. The ϕ that is close to π together with the strong downstream p'_{rer} promote the destructive interference and result a high $TL = 15.8$ db that is 14.2 db increment of the undamped one.

3.1.1.2 Structural response

In order to ascertain the capability of the present numerical methodology in capturing the panel response under acoustic-structural interaction, the variation of the panel velocity over one incident wave period is analysed. Figure 3.6 shows the wavenumber spectrum of the panel mobility $Y_k = (\dot{w}(k))_{rms}/(p'_{inc})_{rms}$, where k is the wavenumber, and the distribution of the panel mobility $Y_x = (\dot{w})_{rms}/(p'_{inc})_{rms}$. In the work of Huang (1999), an incident traveling wave of unit amplitude ($p'_{inc} = 1$) was used and the panel response was represented by the panel velocity. For comparison, the numerical panel velocity is normalized by the incident acoustic pressure so the panel mobility selected to represent the panel response. To determinate the Y_k spectrum, the $(\dot{w}(k))_{rms}$ spectrum should be obtained first. Since the pinned-pinned ends condition is applied, the eigenmode shapes can be expressed as a sinusoidal function and the mode number $N = k/2$ can be converted directly by wavenumber. The $(\dot{w}(k))_{rms}$ spectrum can then be obtained by using standard spatial fast Fourier transform (FFT) procedure. In Figure 3.6(a), the Y_k of a panel with $L_p/H = 5$ without damping is compared with Huang's theoretical data. The panel response dominates the spectrum within a narrowband centered at $k = 6$ corresponding to the 12-th panel mode. Besides, the comparison of Y_x along the panel with that derived from the theoretical results are shown in Figure 3.6(b). The leading edge response is stronger than elsewhere. Both

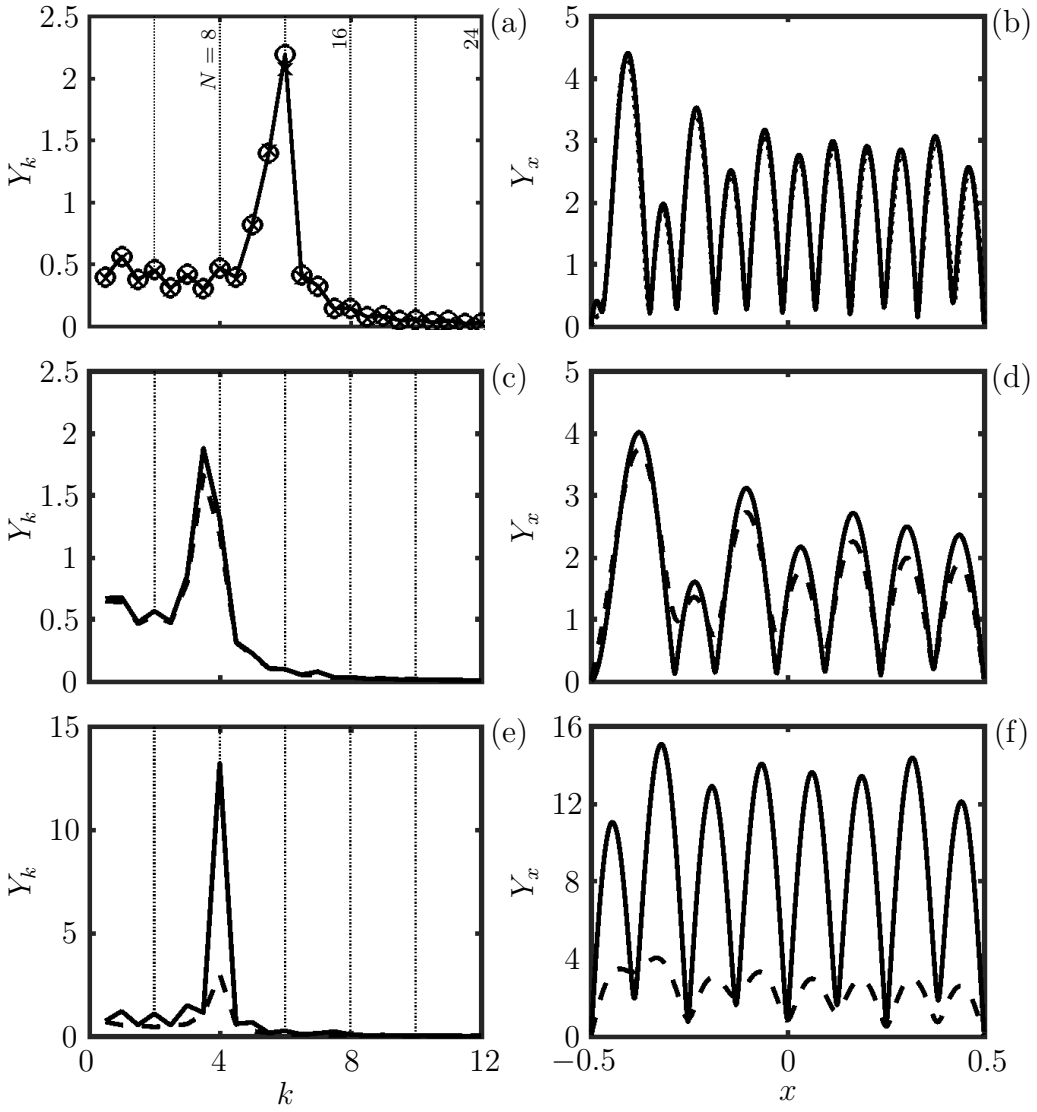

Figure 3.6: Panel responses. Left column, panel mobility spectra Y_k; right column, the distributions of panel mobility amplitude Y_x. (a) & (b), $L_p/H = 5$; ◯, numerical panel mode number N; ×, theoretical (Huang 1999) panel mode number; · · · · ·, theoretical undamped Y_k. (c) & (d), $L_p/H = 3.2$; (e) & (f), $L_p/H = 3.4$. (c) to (f), ——, $C = 0$; – – –, $C = 0.0196$.

comparisons show excellent agreement. The numerical panel responses are also expanded by using the same set of eigenwave modes Huang adopted. The corresponding modal mobilities $Y_k(N)$ are shown as circles in Figure 3.6(a). All the numerical $Y_k(N)$ overlap with the theoretical values except the one at the peak. The maximum deviation of numerical Y_k and Y_x amplitudes from the theoretical values are 5.9% and 4.9% respectively. These differences may be attributed to the stronger fluid inertia induced on the panel response due to the lack of inclusion of the reaction force imposed on the fluid induced by the panel motion in the theory. Generally, these two figures clearly indicate the present numerical methodology is able to capture the panel responses accurately.

In Figure 3.6(b), the present numerical methodology captures all the 12 peaks since the 12-th panel mode is dominated. It is interesting to note that the very weak first peak at $x = -0.48$ with $Y_x = 0.4$, whose magnitude is less than 10% of the others, is captured but not show up clearly in the theoretical solution of Huang (1999). Except for the effect of fluid inertia, this observation may be attributed to a fundamental difference between Huang's and present works. Harmonic temporal and spatial dependence is assumed for all fluctuating quantities in the theory. The capture of the relatively strong harmonic acoustic-structural interaction solutions may be effective but not for transient or weak dynamics, because the solutions may not be perfect harmonic temporal and spatial dependence. On the contrary, there is no restriction in the time marching in the present methodology. Therefore the weak first peak in Figure 3.6(b) can still be captured. In fact, by using the staggered coupling scheme, the calculation of the same problem can also capture the same weak peak. That further supports an assumed harmonic dependence is too restrictive for resolving the acoustic-structural interaction problem completely.

Figure 3.6(c) and (d) show the Y_k spectra and Y_x distributions for the

panel with $L_p/H = 3.2$ which induce high TL. The dominative panel response is within a narrowband centered at $k = 3.5$ that is $N = 7$. The structural damping reduces the amplitude by only 14%. The strongest response appears at the leading edge which is similar to the panel with $L_p/H = 5$. Figures 3.6(e) and 3.6(f) show the same quantities for $L_p/H = 3.4$ which induce low TL. The panel response is dominated by a monotone $k = 4$ that is $N = 8$. The peak Y_k response appears to be 7 times stronger than that of the shorter panel but it can be significantly suppressed with the structural damping. The strongest response is still close to leading edge but its amplitude is higher than elsewhere mildly. Generally, stronger panel response tends to re-radiate stronger acoustic wave to duct downstream.

3.1.2 Aeroacoustic-structural interaction

The capability of the numerical methodology in capturing aeroacoustic-structural interaction was established by comparing with an experimental study of Choy and Huang (2005) on the drum-like silencer carrying a low Mach number flow. Since the viscous effect, in this case, is going to be discussed, the detail is described together with the viscous result in Section 5.1. The setting in Figure 3.1 is used continuously to study the flexible panel interacts with the simultaneous flow and acoustic excitations and its aeroacoustic-structural response in a flow duct, instead of using the setting in the experimental study. The reason is the flexible panels are backed by cavities in the experiment. The cavity effect will make the problem more complicated, so this factor should be eliminated before get a clear understanding of the simple flow duct with a flexible panel. This also benefits for the comparison to the analysis of acoustic-structural interaction in the aforementioned sections. In this case, the same incident acoustic wave is used as Section 3.1.1. The simplest kind of the flow excitation, a uniform mean flow,

is introduced. The uniform means flow with Mach number M is in the same direction with the incident acoustic wave. An undamped panel with $L_p/H = 3.2$ is selected in this case because it has the most obvious response in Figure 3.3. Its variation from low subsonic M to supersonic $M = 1.2$ is studied. The mean flow creates an additional dimension to the incident wave for the excitation acting on the flexible panel. It is enlightening to analyze and study the nonlinear impact on the panel response upon a change from acoustic- to aeroacoustic-structural interaction.

3.1.2.1 Aeroacoustic response

The effect of the aeroacoustic-structural interaction on the acoustic transmission is shown in Figure 3.7. Figure 3.7(a) shows the amplitudes of the upstream and downstream re-radiated wave at different M. The upstream p'_{rer} seems to be prominently affected by the convective effect of the flow. It grows with flow velocity until $M = 0.8$. Afterwards, it reduces sharply down to the zero at $M = 1$ and maintains zero with the supersonic flow. On the other hand, the downstream p'_{rer} appears to be strongly influenced by the panel dynamics. The aeroacoustic-structural interaction effects cause a nonlinear variation of the phase ϕ between the downstream p'_{rer} and p'_{inc} shown in Figure 3.7(b). In the range $0.1 \leq M \leq 0.5$, the downstream p'_{rer} are leading p'_{inc}. Otherwise in other M, the downstream p'_{rer} are leaded by p'_{inc}. It may be the dominating factor to modifies the destructive interference in duct downstream of the panel. For a more clear understanding of the effectiveness of the destructive interference, the difference between ϕ and π is illustrated in Figure 3.7(c). When the difference is large, the destructive interference will be less effective. The overall trend of the difference is growing with M. Summarized Figure 3.7(b) and 3.7(c), four regimes can be divided. They are low subsonic $M \leq 0.05$, middle subsonic $0.1 < M < 0.5$, high subsonic

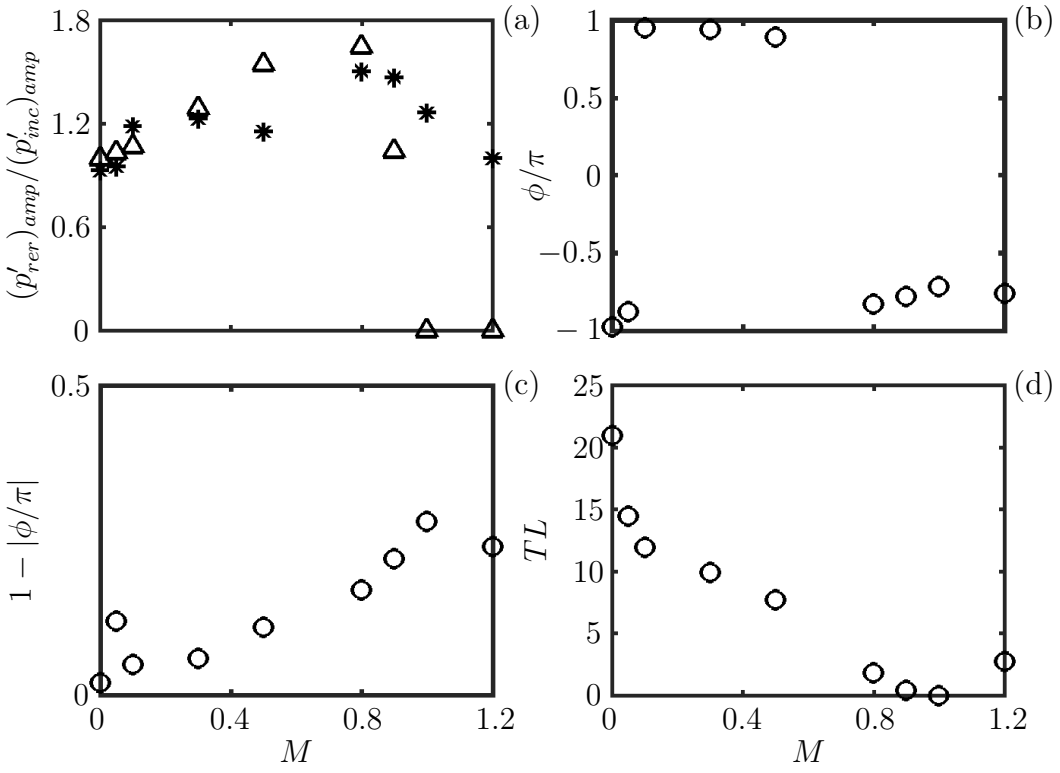

Figure 3.7: Variations of acoustic response with M. (a) Re-radiation amplitude. Δ, upstream radiation; $*$, downstream radiation. (b) Phase shift (ϕ/π) between the downstream re-radiation relative to the incident wave. (c) $1-|\phi/\pi|$. (d) Transmission loss.

$0.5 < M < 1$ and low supersonic $1 < M < 1.2$. Their growing rates are 2, 0.15, 0.32 and -0.2 per unit of M respectively. Figure 3.7(a) shows the amplitudes of upstream and downstream p'_{rer} variation with M. The upstream p'_{rer} grows with mean flow velocity until $M = 0.8$. Afterwards, it reduces sharply down to the zero at $M = 1$ and maintains zero with the supersonic flow. It seems to be prominently affected by the convective effect of the flow. On the other hand, the downstream p'_{rer} show approximately stepwise increase within subsonic M and eventually drops linearly with M when it close to sonic and becomes supersonic ($M > 0.9$). Except $M \leq 0.05$ and $M = 1.2$, all other downstream p'_{rer} are larger than the p'_{inc}. Figure 3.7(d) shows TL variation with M. Four regimes are divided in the following similar to the aforementioned discussion. TL drops rapidly with the increasing M in low subsonic regime $M < 0.1$, the rate is ~ 90 db per unit of M. It drops continuously in the regimes of $0.1 < M < 0.5$ and $0.5 < M < 1$ with rates of ~ 10 db and ~ 16 db respectively. Finally, it vanishes with a sonic mean flow, $M = 1$, and rises up again to 2.6 db at $M = 1.2$ with a rate of ~ 13 db. The overall trend of the TL is suppressed by M increment until supersonic mean flow. The TL is most sensitive to the change of mean flow velocity in the low subsonic zone. The ratio between the changing rates of TL variation with M is similar to the changing rates of ϕ. Therefore the TL variation is highly related to the ϕ variation. Besides in sonic mean flow, there is no upstream p'_{rer} and TL. All the incident wave energy transmitted to downstream. The aeroacoustic-structural interaction may only affect the phase of the incident wave propagation. However, there are also no upstream p'_{rer} but TL is not zero in the supersonic mean flow. In this case, the incident acoustic energy loss may be transformed into other forms, such as heat or flow, by the aeroacoustic-structural interaction.

The downstream re-radiation patterns with different M illustrated in Figure 3.8 provided more information to explain the emergence of the TL trend. As

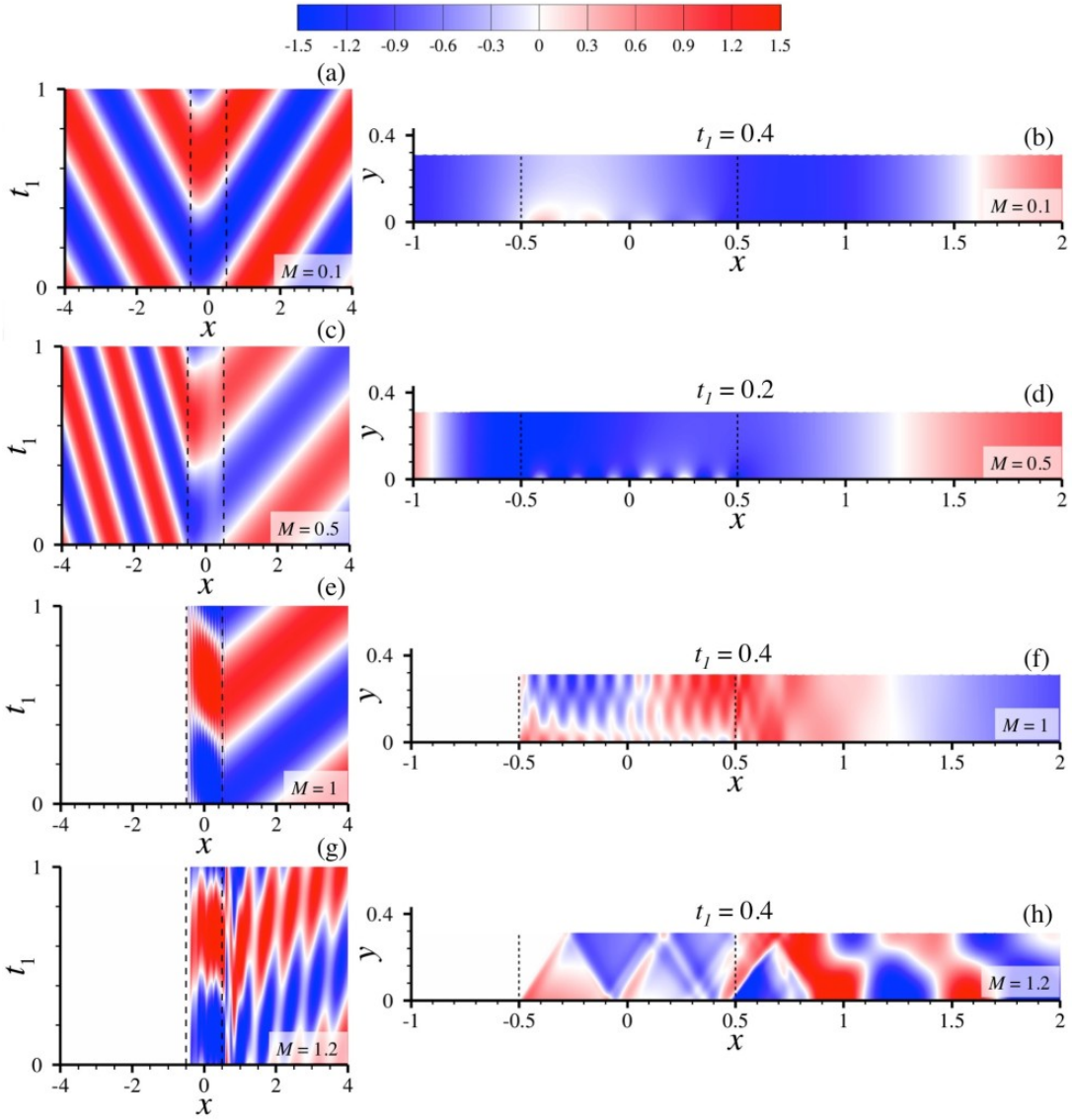

Figure 3.8: Re-radiation at different M ($L_p/H = 3.2$). Left column, p'_{rer} along the centerline of the duct. Right column, snapshots at selected t_1.

observed in Figure 3.8(a) the p'_{rer} at $M = 0.1$ shows high resemblance to the case without mean flow (Figure 3.4(c)). That means the aeroacoustic-structural interaction induced in this case operates in a similar way as the pure acoustic-structural interaction. Although the flow convection increases the deviation of ϕ from π by a small amount (Figure 3.7(b)), it is sufficient to distort the standing wave pattern upstream of the panel and make the destructive interference downstream less effective. As a matter of fact, perfect destructive interference is never achieved under the aeroacoustic-structural interaction. So the TL drops from 20.9 db at $M = 0$ to reach 11.9 db at $M = 0.1$, weakens further to 7.7 db at $M = 0.5$ at which the flow convection effects enhances (Figure 3.8(c)), and then practically vanishes at $M = 1$. It is worthwhile to note that, as long as the mean flow is subsonic, the p'_{rer} generation is confined in the proximity of the excited panel and will propagate away as clean plane waves at the panel leading and trailing edges (Figures 3.8(b) and 3.8(d)). When the flow becomes sonic, p'_{rer} is able to propagate only in downstream direction. Once generated the p'_{rer} will undergo multiple reflections between the upper duct wall and the vibrating panel and form a partial standing wave across the duct width (Figure 3.8(e)). Part of its energy propagates away as a plane wave mixed with contribution from the excited first higher-order duct acoustic mode (Figure 3.8(f)). The higher-order mode radiation decays rapidly and a clean plane wave emerges at $x \sim 1.3$. Although the eventual plane wave in p'_{rer} is 27% stronger than the incident wave, their resultant wave gives an amplitude identical to the incident wave with their ϕ given in Figure 3.7(b) so $TL = 0$.

A new aeroacoustic-structural interaction phenomenon emerges at $M = 1.2$ (Figures 3.8(g) and 3.8(h)). In this case a shock forms and reflects after hitting the upper duct wall at $x \sim -0.3$. The multiple reflections of oblique shock waves persists up to $x \sim 0.9$. The occurrence of this phenomenon can be explained as

follows. Under the action of aeroacoustic-structural interaction, the displacement of the vibrating panel effectively produces a weak obstruction to the passage of the mean flow. When the supersonic mean flow approaches the obstructing panel vibration, it is forced to change its direction for satisfying the tangency boundary condition (Section 2.3.2) and consequently creates a weak oblique shock at the panel leading edge. Such flow features resemble that occur in a steady isentropic supersonic flow passing over a wedge with a half-angle θ_{wedge} (John and Keith 2006) and the flow Mach number, determines the shock angle in response to flow direction change. Assuming the effective θ_{wedge} in the present case is equal to the rms value (= 0.052) of the panel deflection over one incident wave period, the theory of gas dynamics predicts an effective shock angle of 56.54 at $M = 1.2$. From the present numerical results, we determine the rms shock angle to be 57.28. The close agreement between the numerical and theoretical shock angle confirms the obstruction effect of panel vibration. The deviation may attribute to the phase difference of p'_{rer} generation along the vibrating panel. One may argue that the panel vibration can be viewed equivalently as a collection of acoustic point sources for p'_{rer} generation laid along an unexcited panel. The shock waves are just the accumulation of upstream propagation p'_{rer} due to the Doppler effect of the supersonic mean flow. From this view we calculate the shock angle to be 56.44. Its relatively larger deviation from the numerical results firmly establishes the panel displacement really matters in the present problem and highlights its role in the aeroacoustic-structural interaction at high flow velocity. From Figure 3.8(h) the oblique shocks tend to strongly excite the first higher-order duct mode in p'_{rer} which decays completely beyond $x = 20$. It then also produces a p'_{rer} plane wave but its amplitude is weaker than in the $M = 1$ case.

3.1.2.2 Structural response

A summary of the panel response from $M = 0$ to 1.2 is show in Figure 3.9. For easier comparison, all spectra in the figure are expressed in terms of mode number N only rather than shown with wavenumber k. The variation of the modal mobilities $Y_k(N)$ with M is given in Figure 3.9(a). The dominant mode is observed that bifurcates to two branches when the mean flow present. Then the dominant modes are recorded and the variation with M is shown in Figure 3.9(b). Since the results are discreted rather than continuous, the complete functions of M cannot be determined. However, the variation is observed that can be roughly divided into four distinct regimes same as the aeroacoustic response in Section 3.1.2.1. The first regime is $0 \leq M \leq 0.1$, the panel response essentially dominates within a narrowband centered at $N = 7$ as in the no flow case. The bandwidth increase with M but the peak amplitude reduces simultaneously. Two peaks are found at $N = 6$ to 8 when $M = 0.1$, their modal amplitudes are comparable. This change significantly indicated the dominant modes bifurcation begins. When $M = 0.3$, the Y_k distribution total transforms from a unimodal to a bimodal pattern with a strong modal band at $N = 4$ and a weak one at $N = 10$. The panel response changes substantially with M. The lower modal band goes towards $N = 0$ and strengthens as M increases further. On the other side, the higher modal band moves away from the lower one but gets weaker. Such substantial changes are almost in a linear manner when $M < 0.5$. Thus $0.1 < M \leq 0.5$ is defined as the second regime. The lower band settles at $N = 1$ until $M = 0.8$. Its bandwidth suddenly widens when M increases to 0.9, but reduces again when $M = 1$. At the same time, the higher modal band continuously moves farther away and arrived $N = 23$ when $M = 1$. $0.5 < M < 1$ is defined as the third regime. In the fourth regime $M \geq 1$, the higher modal band die away and only remains the lower modal band at $N = 1$.

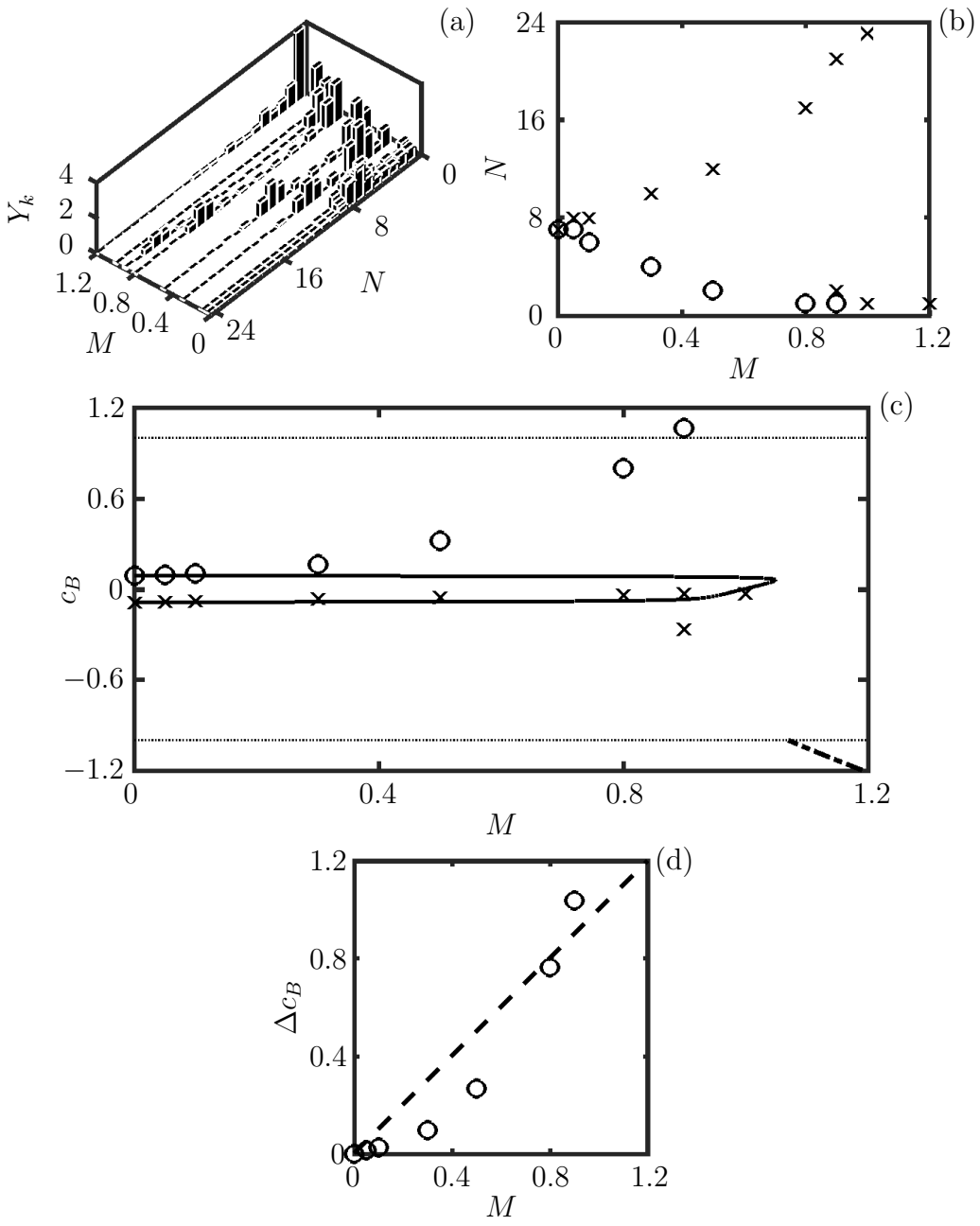

Figure 3.9: Panel responses. (a) Variation of Y_k spectra with M. (b) Distribution of dominant modal peaks. (c) Distribution of flexural wave velocity c_B. ——, the subsonic branch; $- \cdot - \cdot -$, the first mode of supersonic branch; $\cdots\cdots$, $c_B = 1$. (d) The difference between the two opposite flexural wave velocities. In (b) & (c), ◯, $c_B > 0$; ×, $c_B < 0$.

The bimodal pattern revealed suggests that two types of flexural waves emerge in the panel response as a result of the nonlinear aeroacoustic-structural interaction. Indeed they represent the flexural waves with different travelling directions. For a better understanding of their characteristics, the two dimensional Fourier transformation proposed in Lam et al. (2013) is applied to the panel response in one incident wave period. The panel velocities in time and space domain $\dot{w}(t,x)$ are transformed to frequency and wavenumber domain $\dot{w}(f,k)$ according to

$$\dot{w}(f,k) = \frac{1}{2\pi} \int_{-\infty}^{\infty} \int_{-\infty}^{\infty} \dot{w}(t,x) e^{-2\pi i(kx+ft)} dx dt. \tag{3.4}$$

The frequency/wavenumber distribution of $\dot{w}$ can be obtained and the phase velocities c_B of the flexural waves are readily determined since $c_B = f/k$. The variation of c_B with M is shown in Figure 3.9(c), and different travelling directions are marked as respective notations. Upstream $c_B < 0$ and downstream $c_B > 0$ travelling waves are represented by $\times$ and $\bigcirc$ respectively. Same notations are also used in Figure 3.9(b) for easier comparison. It is found that whenever the mean flow is subsonic, there are the two flexural waves travelling in opposite directions on the panel. The flexural waves associated with lower modal bands travel towards downstream and higher bands travel against the flow direction. However, an extra flexural wave with $N = 2$ appears when $M = 0.9$. When $M \geq 1$, the downstream travelling flexural wave vanishes and only the upstream waves exist.

The phase velocities c_B are also compared with the linear theory. Choi and Kim (2002) carried out a theoretical analysis for the same setup as in the present problem. They derived a general equation for the flexural wave dispersion characteristics in an infinitely long panel with the effect of mean flow taken into account. The characteristic equation is derived by the two-dimensional homogeneous wave equation and the membrane equation in the frequency domain.

Both solutions of the equations, acoustic pressure and membrane displacement, are assumed harmonic time dependence. Through the pressure equivalent and wavenumber relation, the characteristic equation is derived and given below after normalization,

$$\rho_p h_p \omega - iC - T_x \omega / c_B^2 = iZ_f \tag{3.5}$$

where $i^2 = -1$, $\omega = 2\pi f$, the fluid impedance $Z_f = -i\rho\omega \cot(k_y)/k_y$ when $c_B > 1$ (supersonic branch), and $Z_f = i\rho\omega \coth(|k_y|)/|k_y|$ when $c_B < 1$ (subsonic branch), and $k_y = \omega\sqrt{(1 - M/c_B)^2 - 1/c_B^2}$. Note that here the descriptions supersonic, or subsonic, indicate when the flexural wave velocities faster or slower than the ambient acoustic velocity in fluid domain. It is different from the definition of M which measures the mean flow velocity relative to the ambient acoustic velocity. For the present panel of interest, Equation 3.5 is solved to determine the eigenwave velocities at different M, and compare the results with the flexural velocity resolved from the frequency/wavenumber distribution in Figure 3.9(c). Only the first two theoretical eigenwave modes are shown in the figure. The four regimes defined earlier are still evident in the variation of c_B. When there is no mean flow, two flexural waves simply have the same eigenwave velocities. In the first regime, the effect of aeroacoustic-structural interaction is not strong because the velocities shift to positive side little bit as M increases up till 0.1. However, the velocity shift becomes evident in the second regime. The downstream travelling wave velocity appears to grow significantly with M as it aligns with the mean flow direction. Against with the flow, the upstream travelling wave slows down slightly from the eigenwave velocity. Notwithstanding these velocity changes, the mobility Y_x still exhibits a regular pattern along the panel, which can be referred to Figures 3.10(a) and 3.10(b) that show the distributions of Y_x at $M = 0.1$ and 0.5. The velocity shifts increase continuously in the third regime. The downstream travelling wave finally becomes supersonic $c_B > 1$ at $M = 0.9$. At the

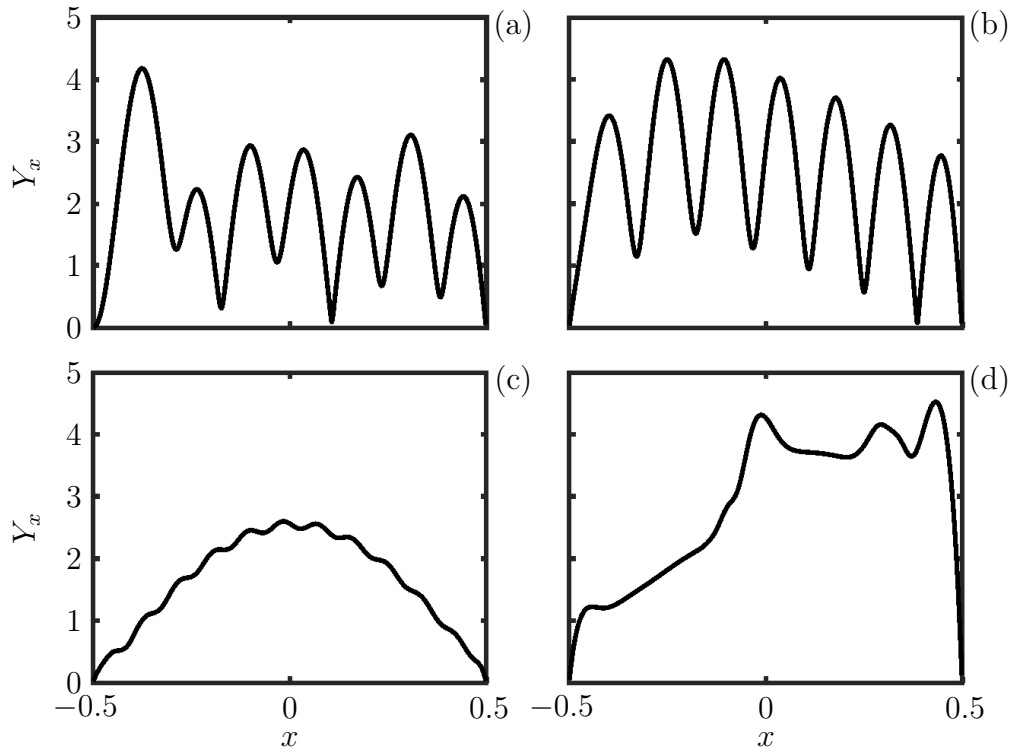

Figure 3.10: Distributions of Y_x at different M. (a) $M = 0.1$; (b) $M = 0.5$; (c) $M = 1$; (d) $M = 1.2$.

same time, an additional subsonic upstream travelling wave with $c_B = -0.27$ emerges. When the mean flow becomes sonic, $M = 1$, the downstream travelling wave stops and only two upstream travelling modes are possible. One of them is close to the theoretical eigenwave velocity but another takes up a much higher $c_B = -16$ with mode shape $N = 1$, which is shown in Figures 3.9(a) but not in Figure 3.9(c) because the scale is too large compared to the others. Its pattern of Y_x distribution is given in Figure 3.10(c), the first mode $N = 1$ is dominated. In the last regime the c_B slows down to -5.3, which is not shown in Figure 3.10(c) again, when the mean flow takes a supersonic $M = 1.2$. The regularity of Y_x distribution is completely lost as shown as Figure 3.10(d). The modal vibration is limited around panel leading edge because of the strong fluid-loading induced by the shock waves within $-0.5 \leq x \leq 0.1$ as shown as Figure 3.8(h). The modal vibration near the panel trailing edge gets stronger, due to weaker fluid-loading induced by the shock waves within $0 \leq x \leq 0.45$, and appears to contribute most to the p'_{rer} radiation far downstream.

The result only agrees well with the theory when $M < 0.3$, it shows the bimodal flexural wave pattern that the theory cannot predict. It may be argued that the reason and mechanism of the emergence of this pattern is the Doppler effect. The acoustically induced excitation under the action of mean flow should be accelerated in the flow direction and decelerated against the flow. Since the flexural waves are driven by the acoustically induced excitation, the difference between the two opposite flexural wave velocities Δc_B should bear a linear relationship with M which is $\Delta c_B = M$. However, Figure 3.9(d) shows that the emergence of bimodal flexural wave pattern is not only caused by the Doppler effect. The supersonic flow case is not included in the figure because the panel has only one wave there. The result shows Δc_B increases nonlinearly with M. The difference is less than M for low subsonic flow $M \leq 0.8$ and surpasses M

with higher subsonic M like $\Delta c_B = 1.04$ at $M = 0.9$. Such trend clearly indicates the nonlinearity by the aeroacoustic-structural interaction imposes on the panel dynamics. In addition, the incompressible theory only includes fluid inertia effect and ignores the fluid compressibility. Since $M > 0.3$, the non-negligible density change shows up in the compressible flow (White 1998). Therefore the it is only valid for low M. The assumption of fluid incompressibility is relaxed in the present study comparing to their theories. The effect of fluid compressibility may be the reason that triggers the bimodal pattern. It further supports that the significant bimodal flexural wave pattern when $M \geq 0.3$ shown in Figure 3.9(c) is caused by the effect of fluid compressibility. Nevertheless, the underlying mechanism has not been clearly understood yet, so a further study is needed.

3.2 Broadband excitation

The aforementioned analysis is primarily focused on a single frequency excitation, the effect of excitation frequencies is not considered. The broadband excitation is so selected to explore these effect in the following. Li (2015) has studied the silencing performance and aeroacoustic-structural responses of a flexible duct segment exposed to broadband excitation. The computational domain is illustrated in Figure 3.11. In this cases, the panel length is 1000 mm so the panel length to duct width ratio is $L_p/H = 10$. The broadband incident acoustic plane wave cover a range from a low frequency 4.25 to the cut-off 1700 Hz with a frequency resolution 4.25 Hz, so in dimensionless $f = 0.0125$ to 5 with $\Delta f = 0.0125$. Following the method of Leung et al. (2007), the excitation functions are written as,

$$p'_{inc} = p_A \sum_{n=1}^{400} \sin(2\pi t f_n + \theta_n), \tag{3.6}$$

$$u'_{inc} = p'_{inc}/\rho, \tag{3.7}$$

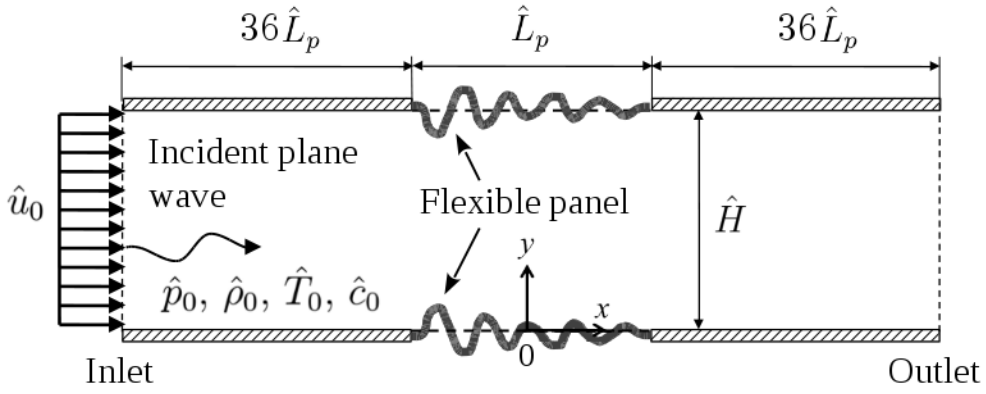

Figure 3.11: Schematic configuration of a finite length tensioned flexible duct segment in an infinite rigid flow duct (not-to-scale).

where p_A is pressure amplitude and constant to all f_n, and θ_n is uniformly random phase. Other settings are same as in Section 3.1.1.

Li's results are briefly described in the following. He studied four cases with different mean flow speed $M = 0$, 0.1, 0.5 and 0.9. As shown as Figure 3.12, the silencing performance is reduced by the mean flow for low frequency ($f < 1$) but the change with the mean flow in the higher frequency range ($f > 1$) is not linear. In absence of flow, TL is shown in an increasing trend to f with a converging fluctuation when the frequency $f < 2.95$. When $f > 2.95$, TL suddenly drop and tend to zero. It indicates that $f = 2.95$ is the critical frequency f_{crit} for the silencing effectiveness. At low subsonic $M = 0.1$, the general trend is similar to $M = 0$ but keeps at lower level around $TL \sim 10$ db. The f_{crit} also shift to higher value 3.06 with $TL = 14.9$ db. When $M = 0.5$, although the average value of TL further drops to ~ 3.5 db when $f < 1$, the trend increase sharply to the $f_{crit} = 2.69$ with $TL = 58.5$ db. The effective band of noise reduction becomes narrow. When $M = 0.9$, the effective band of noise reduction become narrower to around $2 < f < 3$ and TL of the whole spectrum are suppressed to very low. f_{crit} also cannot be determined. There are only two major peaks in

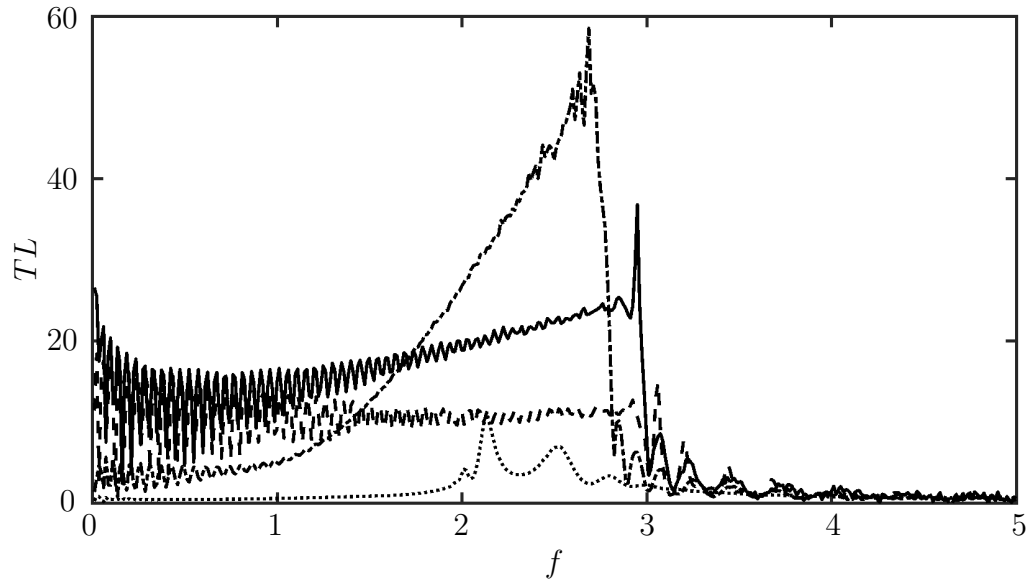

Figure 3.12: The TL spectra of four different mean flow speeds (Li 2015). ——, $M = 0$; – – –, $M = 0.1$; – · – · –, $M = 0.5$; · · · · · ·, $M = 0.9$.

this range, they are $TL = 10.9$ db at $f = 2.14$ and $TL = 6.9$ db at $f = 2.53$.

On the other hand, two sets of flexural waves are discovered in the panel responses. The variation of flexural wave velocities with mean flow speed is also found nonlinear. However, the underlying mechanism related to the structural and acoustic responses is still unclear yet. These results are worth to be further analysed, so his data are used for more detailed analysis and discussion here. The following discussions focus on the structural and near field fluid responses.

3.2.1 Dispersion characteristic of structural response

The phase velocities and the travelling directions of the flexural waves of all frequencies can be found by transforming the result in the time-space domain to frequency/wavenumber domain. The panels motions are found that are in varicose so only the response of the lower panel is taken for analysis. There do not have any constraints on the motion of the panels. Therefore the opposed sinuous

motions are totally due to the symmetry of the set-up. The technique in Section 3.1.2.2 is applied again, the panel mobility in a period of lowest frequency, $T = 80$, are transformed to frequency/wavenumber domain by Equation 3.4 and $Y_{f,k}(f,k) = \dot{w}(f,k)/p'_{inc}$. Figure 3.13 shows the panel responses with four difference mean flow speed and compared with the theoretical prediction by incompressible theory. The theoretical solution can be found by solving Equation 3.5. The negative and positive wavenumbers represent the travelling direction which is upstream and downstream directions respectively. The dotted lines represent the acoustic wave speed in fluid since the upstream and downstream travelling speeds are $M - 1$ and $M + 1$ respectively. They divide the subsonic and supersonic zones which defined that the flexural wave speed comparing to the acoustic wave speed in the fluid. In each sub-figure, any responses bounded by two dotted lines are travelling with supersonic speed ($c_B > M + 1$ or $c_B < M - 1$). In contrast, other responses are travelling with subsonic speed ($M + 1 > c_B > M - 1$). When $M = 0$, two modes of response, subsonic and supersonic modes, are found. The subsonic mode responses to all frequencies and the frequency/wavenumber relation strongly agree with the theoretical prediction. The supersonic mode also has a great agreement with the theory. It appears when $f \leq 2.98$ which only 1.4% difference to the theory. When a low subsonic flow $M = 0.1$ presented, the subsonic mode offsets a little bit from the theory. As the discussion in Section 3.1.2.2, the difference should be resulted by the fluid compressibility effect. In terms of travelling speed, the downstream travelling mode is faster than the theoretical prediction, and the upstream one is in contrast. It shows the lack of fluid compressibility effect causes underprediction of the influence of mean flow on the subsonic panel response, but the supersonic mode is not obviously affected in this case. When the mean flow speed increase to $M = 0.5$, the compressibility effect is more obvious. The theoretical subsonic mode does not change too much

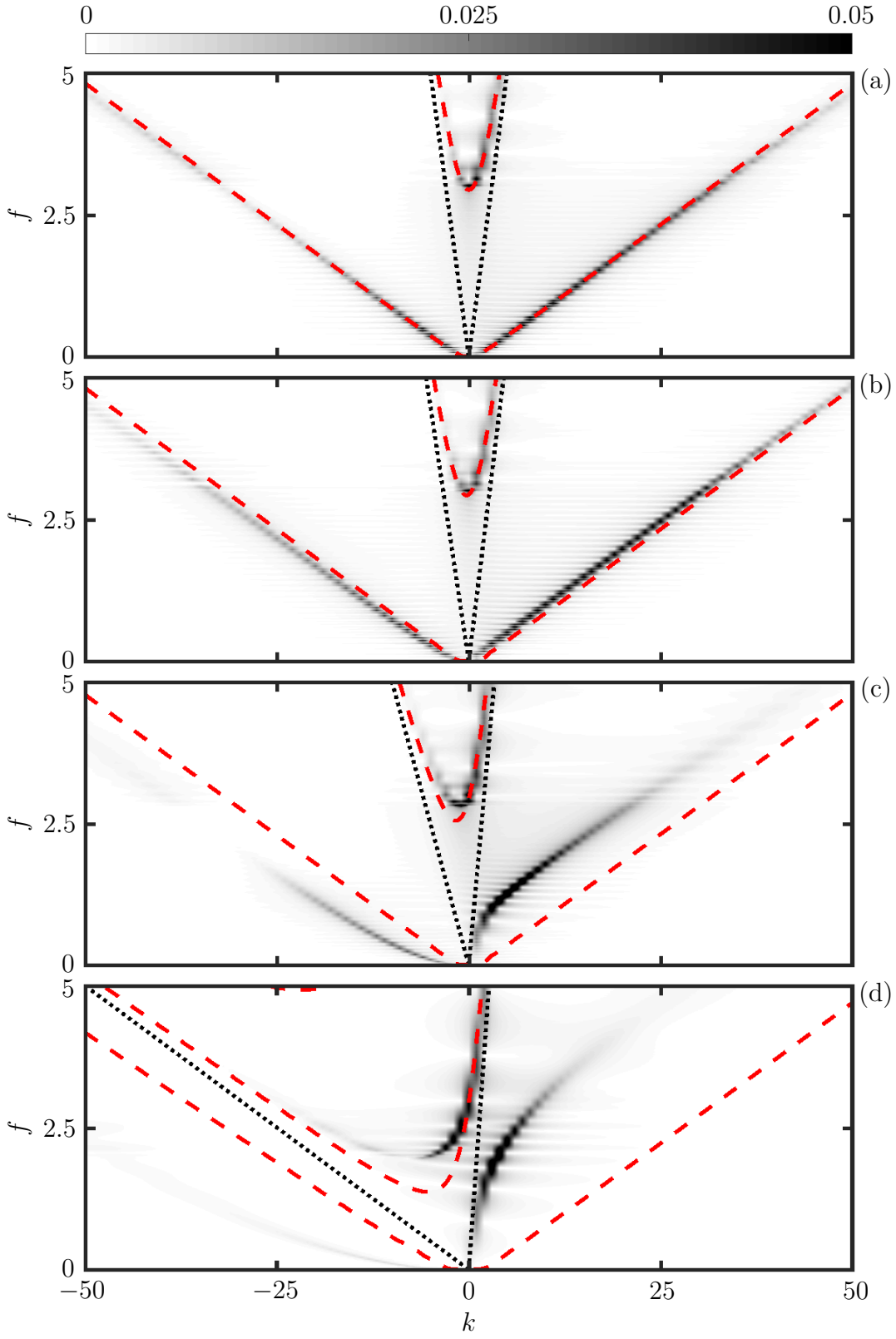

Figure 3.13: Frequency-wavenumber spectra of $Y_{k,f}$. (a), $M = 0$. (b), $M = 0.1$. (c), $M = 0.5$. (d), $M = 0.9$. – – –, theoretical prediction with incompressible flow; · · · · ·, acoustic wave speed in fluid.

by the mean flow comparing with $M = 0$. However, the subsonic mode further offsets away from the theory. On the other hand, the compressibility effect on supersonic mode is noticeable. The lowest frequency of this mode is 2.79 but 9.5% difference to the theory. The compressibility effect shifts the lowest frequency of the supersonic mode higher. When $M = 0.9$, the offset from the theory of subsonic mode is further increased. The lowest frequency of supersonic mode is 1.97 and the difference to the theory is also increased to 44.9%. The second supersonic mode predicted by the theory can be merely noticed at around $f \approx 5$ and $-26 < k < -20$ but cannot be observed in the numerical result since it may be out of the frequency range of calculation under the compressibility effect.

Because of the effect of fluid inertia, the mean flow accelerates waves with the same travelling direction (downstream) but decelerates that with opposite travelling direction (upstream) for both subsonic and supersonic modes. The variation of the effect with frequency is nonlinear. When $M = 0$, the travelling speeds of the subsonic mode are constant 0.092 for both direction. When $M = 0.5$ and 0.9 the downstream travelling speed is very close to the sonic speed in a low frequency range that $f < 0.8$. However farther away from $f = 0.8$, the increment is much smaller. The effect of flow to the decrement of upstream travelling speed is also stronger in low frequency. In addition, the effect of flow shifts the lowest frequency of the supersonic mode lower. The lowest frequencies of both $M = 0$ and 0.1 are 2.98. It is shifted to 2.79 and 1.97 when $M = 0.5$ and 0.9 respectively. By comparing the lowest frequencies of the supersonic mode to the f_{crit} of acoustic responses of $M = 0$, 0.1 and 0.5, their differences are less than 0.1. They should be somehow related which the supersonic mode may cause the extremely low TL at high f.

Referring to Figure 3.12, it can be noticed that the downstream travelling speed of subsonic mode at $M = 0.5$ is very close to the sonic speed occur together

with low TL when $f < 1$. For the panel response higher than the f_{crit}, the subsonic mode is weakened and the response is dominated by the supersonic mode. Its downstream travelling speed is close to the sonic speed too. The similar observation also found when $M = 0.9$. The downstream travelling speeds of subsonic mode when $f < 2$ and of supersonic mode when $f > 2.7$ are very close to the sonic speed, and low TL also observed in these frequency ranges. It may indicate that the panel wave with nearly sonic speed is beneficial the transmission of the incident acoustic wave since the difference of their travelling speed is small.

3.2.2 Near field fluid response

To uncover the different effect of two kinds of flexural waves to the fluid, the pressure fluctuation in the area above the flexible panel which can be defined as near field response is discussed in the following. In order to identify any wave travelling, the pressure field is also transformed to frequency/wavenumber domain. The pressure fluctuations $p'(x,t)$ in a period and $-0.5 < x < 0.5$ are transformed as $p'(f,k)$ according to

$$p'(f,k) = \frac{1}{2\pi} \int_{-\infty}^{\infty} \int_{-\infty}^{\infty} p'(x,t) e^{-2\pi i(kx+ft)} dx dt. \tag{3.8}$$

Figure 3.14 shows $p'(f,k)$ in near field with four different mean flow speed. In all four cases, there are no waves travelling exactly with speed of sound. Almost only supersonic waves are observed except $M = 0.9$. In $M = 0.9$, subsonic waves are observed that are only in downstream travelling direction and within around $1.5 < f < 2.5$. By comparing to Figure 3.13, the frequency/wavenumber relation of fluid responses overlap with the panel responses. The amplitudes are also directly proportional to the panel responses. These may indicate that the near field responses are totally controlled by and follow the panel responses.

In addition, the near field response is agreed with the theory presented by

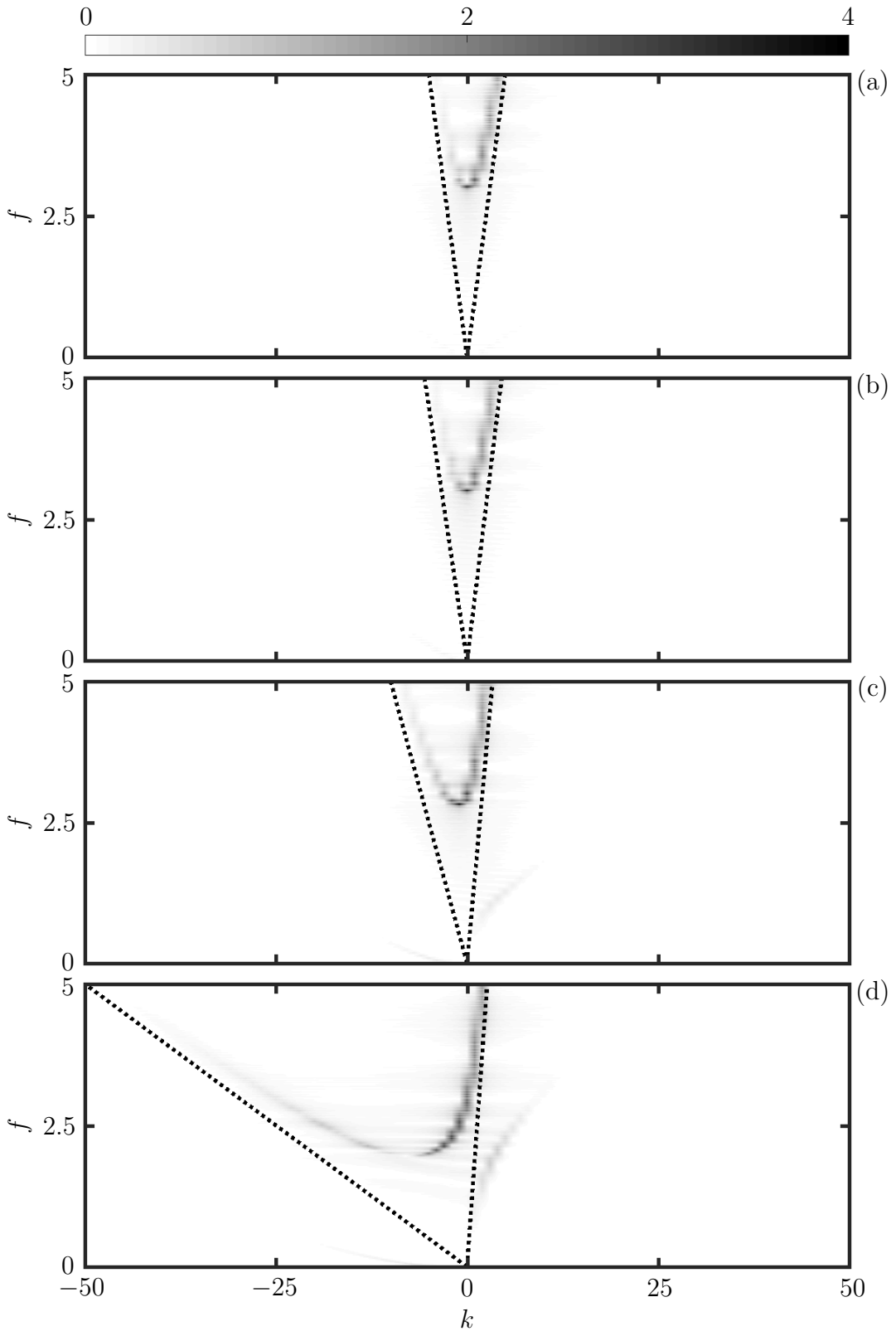

Figure 3.14: Frequency-wavenumber spectra of p' at the duct centreline within $-0.5 < x < 0.5$. (a), $M = 0$. (b), $M = 0.1$. (c), $M = 0.5$. (d), $M = 0.9$. $\cdots\cdots$, acoustic wave speed in far field of fluid domain.

Crighton (1989). The problem discussed by Crighton is the fluid loading effect on vibration of an infinite thin elastic plate driving by a time-harmonic forcing in absence of flow and the corresponding acoustic response. The fluid loading is represented by time-harmonic pressure which satisfies the wave equation. In the theory, when the surface wave speed slower than the acoustic wave speed, it is called a subsonic surface wave. The surface wave represents the transverse wave at the fluid-panel interface, which is equal to the panel responses in this problem. The energy of subsonic surface wave will be transported without loss parallel to the surface, and none is radiated normal to the surface. When the surface wave is supersonic, it will radiate energy to the acoustic field and it is called a leaky wave. Its amplitude decays exponentially in its travelling direction as energy loss to the fluid continuously. The present study has the similar observation that only supersonic waves are observed when $M = 0$ because there are no energy leaks from the subsonic surface wave. However, Figure 3.14(d) indicates the subsonic surface wave may also radiate energy to fluid at high subsonic mean flow. Besides, there has a difference between the theoretical analysis and the present problem that the theory is not considering inside a duct. The disturbances radiated by the panel to the duct near field are reflected by the duct wall of the opposite side and go back to the source again. Such interaction may results that the waves in near field and the surface wave are engaged together, so they have same frequency/wavenumber relation.

By the observation of the near field response, it can be deduced that none of the incident waves can travel through the duct segment with flexible walls directly with speed of sound. In this regards, the transmission loss may created due to two possible reasons. When the incident acoustic waves arrive the flexible panels, it should be transformed as the flexural wave. The input energy may be transported by the wave to the panels trailing edge. A portion is transformed as

acoustic waves again to the downstream by scattering when they hit the edge. The rest is reflected and transported to the upstream by the same process. On the other hand, the another possibility that a portion incident acoustic waves are reflected directly at the panels leading edge because the duct cross-sectional area is changing. However, it is difficult to determine how much is transformed as surface waves or directly reflected because they are mixed together in the present results. Nevertheless, the present numerical model appears able to solve the complete fluid model and the interaction between acoustic, flow and structural dynamics. Therefore all system behaviours can be captured.

Chapter 4

Formulation and Numerical Methods for Viscous Problem

In real applications, viscous flow effect is an important factor that affects the aeroacoustic-structural response. The result in the next chapter also demonstrated that the viscous effect cannot be neglected in the flow-induced vibration problem. Therefore, it is necessary to investigate the fluid-structure interaction in viscous flow.

4.1 Problem of the partitioned approach

The partitioned approach is attempted to calculate the viscous problem first, but the inability of this approach is discovered. For the purpose of indicating the problem of the partitioned approach, the details of numerical setting are not described in this section but can be referred to the coming sections and chapter. For viscous fluid, the Navier-Stokes equations are used instead of Euler equations. The boundary condition of the fluid domain for rigid wall and flexible panel interfaces also have to be modified as no-slip instead of sliding condition. For no-slip condition, the tangential velocity at the interfaces is zero. The detail

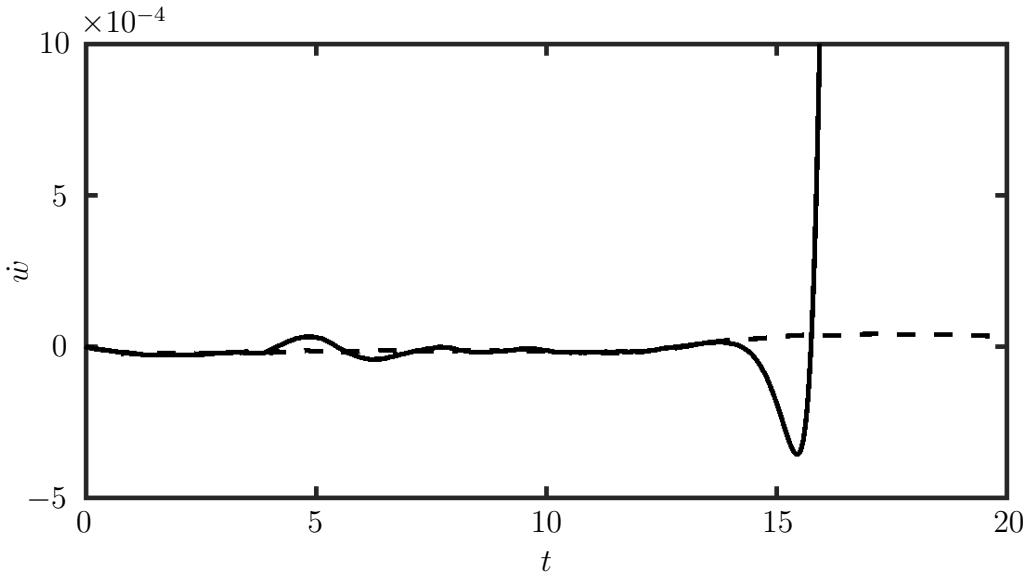

Figure 4.1: Time history of the vibrating velocity at $x = -0.41$. ——, result by the partitioned approach; – – –, result by the monolithic approach.

setting is same as that described in Section 4.2.3.

A flow-induced vibration problem studied experimentally by Liu (2011) is selected as the benchmark case for validation. In this case, a segment of rigid duct wall is replaced by a flexible panel and backed by a rigid cavity. The panel was excited by a low subsonic flow ($M = 0.103$) in the duct, and the vibration would be sustaining which shows the panel instability. The detail description of the problem is shown in Section 5.2. However, the calculation failed after a very short time from the beginning as shown as the time history of the vibrating velocity in Figure 4.1. The maximum vibrating velocity occurs at $x = -0.41$ which is one-tenth of the panel from the leading edge before the calculation break down. Therefore the time history at this location is chosen for demonstrates the panel response. It shows that a sudden change occurred at around $t = 15$ and the amplitude grew to infinite afterward. This cannot be agreed with the experiment.

The problem of partitioned approach may be caused by the incorrect infor-

mation transfer. In the fluid-panel coupling procedure, the panel response exerts on the fluid is only through the setting of ghost element. The ghost element in CE/SE method can be considered as an artificially added fluid element that does not physically exist. The concept is assuming the panel motion is equivalent and can be replaced by a fluid motion with the same velocity, acceleration, and static pressure. However, the influence from panel to fluid is not totally same as fluid to fluid, especially in viscous flow. Except static pressure p and dynamic pressure $(\rho v^2)/2$, the flux in fluid is also contributed by the viscous stresses τ_{yy} and τ_{xy}. For the inviscid problem, viscous stresses vanish so this approach is workable. However, in viscous flow, the ghost element provides additional viscous stresses to the fluid which is incorrect. Through the coupling procedure, the error may accumulate and cause terrible consequence as the case aforementioned. Therefore the partitioned approach is not suitable in CE/SE method for fluid-panel interaction in viscous flow. The monolithic approach, which introduced in the Section 4.2, does not have such problem because the panel and fluid are interacting directly, ghost element is not involved in the coupling. Its result is also put on Figure 4.1 as a reference. This is because the result of the monolithic approach agreed well with the experimental data which is discussed in Section 5.2.2. That validated the monolithic approach provided a proper result for comparison. The reference shows the amplitude is growing but relatively much stable. It further confirms the problem of the partitioned approach. Therefore the monolithic approach must be introduced for the study in the viscous problem.

4.2 Monolithic approach

The monolithic approach solves the fluid and structure dynamics simultaneously in a common system. Therefore the system only contains one set of governing equations which describing both physical behaviors.

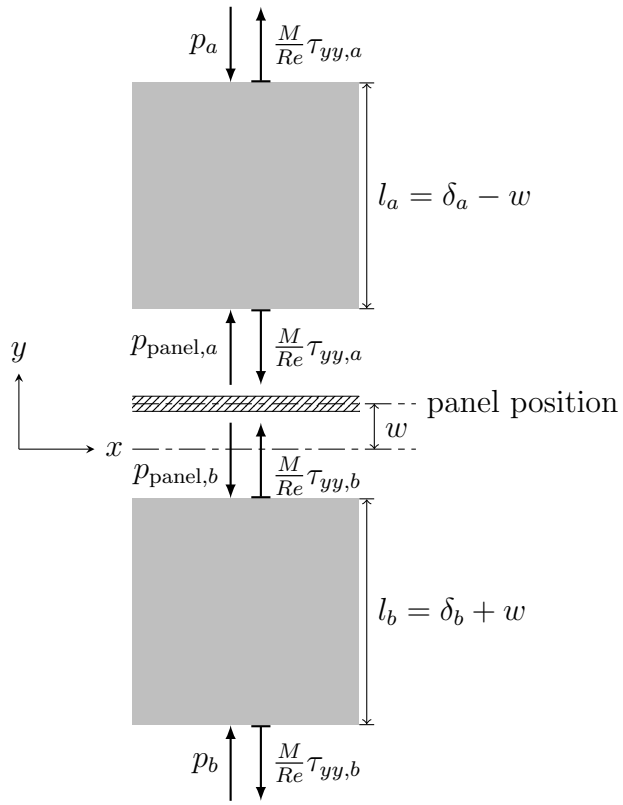

Figure 4.2: Free-body diagram of small control volumes of fluid elements in contact with a flexible panel segment.

4.2.1 Coupled fluid-panel equation

Consider the stresses exerted on two small control volumes of fluid above and below a flexible panel segment, a free-body diagram is drawn as Figure 4.2. There only consider the stresses along y-direction because the vertical vibration of the panel is the primary interest. The viscous perturbation stresses applied in tangential direction along the panel cannot be modelled because only a one-degree-of freedom flexible wall model is used for simplification. The subscript "panel" indicates the variables on the fluid-panel interface. The subscripts "a" and "b" indicate the variables above or below the panel respectively. δ is the initial height of the control volume without panel deflection and $l(t) = \delta - w(t)$ is the height of the control volume which varies with time because the panel displacement $w(t)$

compresses or stretches the volume during vibration. Since the primary focus of the present study is on the weak vibration problem where $w < \delta$, $l_a + l_b$ can be kept as constant along the entire panel. p is the pressure acting from the surrounding on the surface of the fluid volume. The viscosity-induced normal stress (Anderson 2011) may be expressed as

$$\tau_{yy} = \frac{2}{3}\mu\left(2\frac{\partial v}{\partial y} - \frac{\partial u}{\partial x}\right). \tag{4.1}$$

However, the no-slip panel surface gives $\partial u/\partial x = 0$, so the viscosity-induced normal stress can be written as

$$\tau_{yy} = \frac{4}{3}\mu\frac{\partial v}{\partial y}. \tag{4.2}$$

When the fluid is driven by the panel, the additional stress exerted on the fluid element by the panel through its surface in contact is the difference in total stresses, $\sigma = (M/Re)\tau_{yy} - p$,

$$\frac{\partial \sigma}{\partial y} = \frac{M}{Re}\frac{\partial \tau_{yy}}{\partial y} - \frac{\partial p}{\partial y} \approx -\frac{\partial p}{\partial y}, \tag{4.3}$$

where the change of viscous stress $\partial\tau_{yy}/\partial y = (4/3)\mu(\partial^2 v/\partial y^2)$ is neglected because it is higher order and much smaller than the change of pressure $\partial p/\partial y$. The corresponding mechanical power per unit length (Anderson 2011) is

$$v\frac{\partial \sigma}{\partial y} \approx -v\frac{\partial p}{\partial y}. \tag{4.4}$$

This stress σ arising from the vibrating fluid-panel interface modifies the fluid momentum in its normal direction. Therefore, it is better to resolve their effects by expressing them as a source term $\boldsymbol{Q}$ in the homogeneous Equation 2.1 originally for fixed domain boundary. The inhomogeneous form of the governing equations is obtained as,

$$\frac{\partial \boldsymbol{U}}{\partial t} + \frac{\partial\left(\boldsymbol{F} - \boldsymbol{F}_v\right)}{\partial x} + \frac{\partial\left(\boldsymbol{G} - \boldsymbol{G}_v\right)}{\partial y} = \boldsymbol{Q}, \tag{4.5}$$

where

$$\boldsymbol{Q} = \begin{cases} [Q_1,\ Q_2,\ Q_3,\ Q_4]^\intercal = -\dfrac{\partial p}{\partial y}\,[0,\ 0,\ 1,\ v]^\intercal\,, & \text{along fluid-panel interface,} \\ 0, & \text{elsewhere.} \end{cases} \tag{4.6}$$

and it is dependent on the panel dynamics.

On the other hand, the net external force applied to the panel is

$$p_{ex} = \sigma_{\text{panel},b} - \sigma_{\text{panel},a} = \left(p_{\text{panel},b} - \frac{M}{Re}\tau_{yy,b}\right) - \left(p_{\text{panel},a} - \frac{M}{Re}\tau_{yy,a}\right). \tag{4.7}$$

The panel dynamics equation (Equation 2.9) is therefore re-written as,

$$D\frac{\partial^4 w}{\partial x^4} - (T_x + N_x)\frac{\partial^2 w}{\partial x^2} + \rho_p h_p \ddot{w} + C\dot{w} + K_p w = \left(p_{\text{panel},b} - \frac{M}{Re}\tau_{yy,b}\right) - \left(p_{\text{panel},a} - \frac{M}{Re}\tau_{yy,a}\right). \tag{4.8}$$

To satisfy the tangency condition for no-slip wall, velocities of the fluid at the interface and the panel are equivalent (Rugonyi and Bathe 2001), $v = \dot{w}$. From the momentum equation in Equation 2.1, the normal pressure gradient can be obtained as

$$-\frac{\partial p}{\partial y} = \frac{\partial \rho v}{\partial t} + \frac{\partial \rho u v}{\partial x} + \frac{\partial \rho v^2}{\partial y} + \frac{M}{Re}\left(\frac{\partial \tau_{xy}}{\partial x} + \frac{\partial \tau_{yy}}{\partial y}\right). \tag{4.9}$$

When no-slip condition is applied, i.e. $u = \partial u/\partial x = 0$,

$$\frac{\partial\,(\rho u v)}{\partial x} = 0. \tag{4.10}$$

For the physical problems of interest that presented in Sections 5.1 and 5.2 in the next chapter, the vibrating frequency is lower than 1700 Hz which is the cut-off frequency of the duct and the displacement will not larger than 2 mm. Therefore the vibrating velocity will not larger than 3.4 m/s ($M = 0.01$). When the fluid velocity on the wall is small that $M_{wall} = v/c_0 < 0.3$, the local viscous effect and compressibility could be ignored White (1998). Therefore

$$\frac{M}{Re}\left(\frac{\partial \tau_{xy}}{\partial x} + \frac{\partial \tau_{yy}}{\partial y}\right) \approx 0, \tag{4.11}$$

and $\partial\rho/\partial y = \partial v/\partial y = 0$ so

$$\frac{\partial \rho v^2}{\partial y} \approx 0. \tag{4.12}$$

The normal pressure gradient is therefore simply written as

$$\frac{\partial p}{\partial y} \approx -\rho \frac{\partial v}{\partial t} = -\rho \ddot{w}. \tag{4.13}$$

Through the relationship between the normal pressure gradient of fluid, the pressure applied on the panel and the panel acceleration, the fluid (Equation 4.5) and the panel dynamics (Equations 4.8) can be coupled.

4.2.2 Solution strategy for the inhomogeneous equation and discretization

Since the source term is a function of the solution vector $\boldsymbol{U}$, the fluid-panel coupled equations, Equation 4.5, cannot be solved directly. Therefore Newton's method with an iterative procedure is employed to solve $\boldsymbol{U}$ (Loh 2005). First, $\partial \boldsymbol{U}/\partial t$ can be expressed from Equation 4.5 as,

$$\frac{\partial \boldsymbol{U}}{\partial t} = \boldsymbol{Q} - \boldsymbol{H'}, \tag{4.14}$$

where

$$\boldsymbol{H'} = \frac{\partial \left(\boldsymbol{F} - \boldsymbol{F}_v\right)}{\partial x} + \frac{\partial \left(\boldsymbol{G} - \boldsymbol{G}_v\right)}{\partial y}.$$

At j-th time step of solution time marching, the solution vector is estimated by approximating $\partial \boldsymbol{U}/\partial t = \Delta \boldsymbol{U}/\Delta t$,

$$\boldsymbol{U}_j = \Delta t \left(\boldsymbol{Q}\left(\boldsymbol{U}_j\right) - \boldsymbol{H'}\right) + \boldsymbol{U}_{j-1}. \tag{4.15}$$

To eliminate $\boldsymbol{H'}$, the local homogeneous solution $\boldsymbol{U}_H$ when $\boldsymbol{Q} = 0$ is introduced,

$$\boldsymbol{U}_{j,H} = \boldsymbol{U}_{j-1} - \Delta t \boldsymbol{H'}. \tag{4.16}$$

Eliminating $\boldsymbol{H'}$ from Equations 4.15 and 4.16 results in the equation

$$\boldsymbol{\Phi}\left(\boldsymbol{U}_j\right) = \boldsymbol{U}_j - \Delta t \boldsymbol{Q}\left(\boldsymbol{U}_j\right) - \boldsymbol{U}_{j,H} = 0, \tag{4.17}$$

Equation 4.17 is implicit in nature and its solution $\boldsymbol{U}_j$ can be solved with Newton's method through iterating the following equation, where k is the iteration index,

$$\boldsymbol{U}_{j,k+1} = \boldsymbol{U}_{j,k} - \left(\frac{\partial \boldsymbol{\Phi}}{\partial \boldsymbol{U}}\right)^{-1} \boldsymbol{\Phi}\left(\boldsymbol{U}_{j,k}\right). \tag{4.18}$$

Jacobian matrix $\partial\boldsymbol{\Phi}/\partial\boldsymbol{U}$ is given by

$$\frac{\partial \boldsymbol{\Phi}}{\partial \boldsymbol{U}} = \boldsymbol{I} - \Delta t \frac{\partial \boldsymbol{Q}}{\partial \boldsymbol{U}}. \tag{4.19}$$

To determinate $\boldsymbol{U}_j$ from Equation 4.18, the iterative procedure is shown as Figure 4.3 is employed. At the beginning of each time step, the homogeneous solution $\boldsymbol{U}_{j,H}$ is determined by the aeroacoustic model and substituted into Equation 4.18 as initial estimate $\boldsymbol{U}_{j,k=1}$ to start the iteration. The iteration will terminate when the relative errors between the solutions at iterations k and $k+1$ at all mesh points is less than the prescribed precision ε, i.e.

$$\frac{|\boldsymbol{U}_{k+1} - \boldsymbol{U}_k|}{|\boldsymbol{U}_{k+1}|} < \varepsilon, \tag{4.20}$$

then the final solutions $\boldsymbol{U}_j = \boldsymbol{U}_{k+1}$ is marched forward to next time step; otherwise the iteration continues until the precision requirement is reached. The precision requirement $\varepsilon = 10^{-10}$ which is same as that in the iterative partitioned method in Chapter 2, and the number of iterations is around 4 in all the calculations reported by using the monolithic approach.

In order to determines $\boldsymbol{Q}$ and $\partial\boldsymbol{Q}/\partial\boldsymbol{U}$ in Equations 4.17 and 4.19, $p_{\text{panel},a}$ and $p_{\text{panel},b}$ have to be estimated from the panel dynamics for determining the normal pressure gradients $\partial p/\partial y$, and which must be expressed as in terms of $\boldsymbol{U}$.

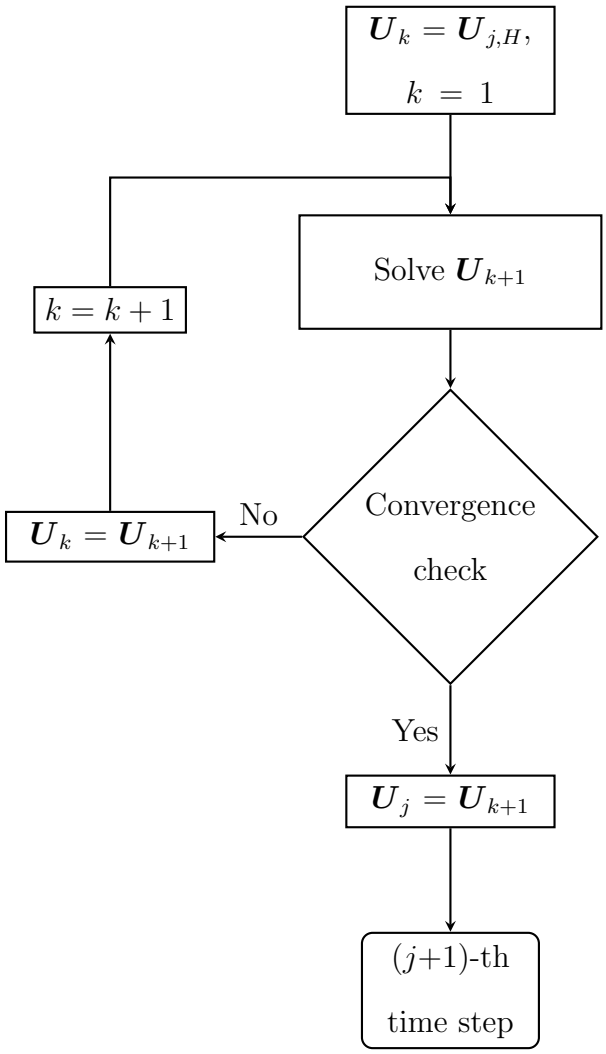

Figure 4.3: Iterative procedure for Newton's method.

Referring to Figure 4.2, the normal pressure gradient (Equation 4.13) above and below the panel, and panel acceleration are approximated as

$$\left(\frac{\partial p}{\partial y}\right)_a = \frac{p_a - p_{\text{panel},a}}{l_a}, \quad \left(\frac{\partial p}{\partial y}\right)_b = \frac{p_{\text{panel},b} - p_b}{l_b}, \tag{4.21}$$

$$\ddot{w} = \frac{1}{\rho_a}\left(\frac{p_{\text{panel},a} - p_a}{l_a}\right) = \frac{1}{\rho_b}\left(\frac{p_b - p_{\text{panel},b}}{l_b}\right). \tag{4.22}$$

The relationship between $p_{\text{panel},a}$ and $p_{\text{panel},b}$ are than given by Equation 4.22,

$$p_{\text{panel},b} = \frac{l_b\rho_b}{l_a\rho_a}\left(p_a - p_{\text{panel},a}\right) + p_b. \tag{4.23}$$

On the other hand, the velocity gradient can be approximated by the equivalent of velocity as

$$\left(\frac{\partial v}{\partial y}\right)_a = \frac{v_a - \dot{w}}{l_a}, \quad \left(\frac{\partial v}{\partial y}\right)_b = \frac{\dot{w} - v_b}{l_b}. \tag{4.24}$$

Therefore the normal stresses in Equation 4.2 can be approximated as

$$\tau_{yy,a} = \frac{4}{3}\mu\frac{v_a - \dot{w}}{l_a}, \quad \tau_{yy,b} = \frac{4}{3}\mu\frac{\dot{w} - v_b}{l_b}. \tag{4.25}$$

By substitute $p_{\text{panel},b}$, $\tau_{yy,a}$ and $\tau_{yy,b}$ into Equation 4.8, it can be re-written as,

$$\begin{aligned} D\frac{\partial^4 w}{\partial x^4} - (T_x + N_x)\frac{\partial^2 w}{\partial x^2} + \rho_p h_p \ddot{w} + \left[C + \frac{4}{3}\frac{M}{Re}\left(\frac{\mu_a}{l_a} + \frac{\mu_b}{l_b}\right)\right]\dot{w} + K_p w \\ = \frac{l_b\rho_b}{l_a\rho_a}\left(p_a - p_{\text{panel},a}\right) + p_b - p_{\text{panel},a} + \frac{4}{3}\frac{M}{Re}\mu\left(\frac{v_b}{l_b} + \frac{v_a}{l_a}\right), \end{aligned} \tag{4.26}$$

At j-th time step, the vibrating velocity $\dot{w}$ can be approximated by integrating $\ddot{w}$ and using backward finite difference procedure,

$$\begin{aligned} \dot{w}^j = \int_{j-1}^{j} \ddot{w}dt + \dot{w}^{j-1} &= \frac{\Delta t}{2}\left(\ddot{w}^j + \ddot{w}^{j-1}\right) + \dot{w}^{j-1} \\ &= \frac{\Delta t}{2}\frac{1}{l_a\rho_a}\left(p_{\text{panel},a} - p_a\right) + \frac{\Delta t}{2}\ddot{w}^{j-1} + \dot{w}^{j-1}. \end{aligned} \tag{4.27}$$

Similarly the panel displacement w can be also approximated as

$$\begin{aligned} w^j = \int_{j-1}^{j} \dot{w}dt + w^{j-1} &= \frac{\Delta t}{2}\left(\dot{w}^j + \dot{w}^{j-1}\right) + w^{j-1} \\ &= \frac{\Delta t^2}{4}\frac{1}{l_a\rho_a}\left(p_{\text{panel},a} - p_a\right) + \frac{\Delta t^2}{4}\ddot{w}^{j-1} + \Delta t\dot{w}^{j-1} + w^{j-1}. \end{aligned} \tag{4.28}$$

Since $\ddot{w}$, $\dot{w}$, and w are written as functions of $p_{\text{panel},a}$, $p_{\text{panel},a}$ can be than obtained explicitly from Equation 4.26 and expressed in terms of $\boldsymbol{U}$,

$$p_{\text{panel},a} = \frac{1}{1+B'}\left(B'p_a + p_b + B'_0\right), \tag{4.29}$$

where

$$B' = \frac{1}{l_a U_{1,a}}\left\{l_b U_{1,b} + \rho_p h_p + \frac{\Delta t}{2}\left[C + \frac{4}{3}\frac{M}{Re}\left(\frac{\mu_a}{l_a} + \frac{\mu_b}{l_b}\right)\right] + \frac{\Delta t^2}{4}K_p\right\},$$

$$\begin{aligned} B'_0 = \frac{4}{3}\frac{M}{Re}\left(\frac{\mu_a}{l_a}\frac{U_{3,a}}{U_{1,a}} + \frac{\mu_b}{l_b}\frac{U_{3,b}}{U_{1,b}}\right) - \left[C + \frac{4}{3}\frac{M}{Re}\left(\frac{\mu_a}{l_a} + \frac{\mu_b}{l_b}\right)\right]\left(\frac{\Delta t}{2}\ddot{w}^{j-1} + \dot{w}^{j-1}\right) \\ - K_p\left(\frac{\Delta t^2}{4}\ddot{w}^{j-1} + \Delta t\dot{w}^{j-1} + w^{j-1}\right) - D\frac{\partial^4 w}{\partial x^4} + (T_x + N_x)\frac{\partial^2 w}{\partial x^2}, \end{aligned}$$

$$p_a = (\gamma - 1)\left[U_{4,a} - \frac{1}{2U_{1,a}}\left(U_{2,a}^2 + U_{3,a}^2\right)\right],$$

$$p_b = (\gamma - 1)\left[U_{4,b} - \frac{1}{2U_{1,b}}\left(U_{2,b}^2 + U_{3,b}^2\right)\right].$$

By substitute Equations 4.23 and 4.29 into Equation 4.21, the normal pressure gradients are re-written as

$$\left(\frac{\partial p}{\partial y}\right)_a = -\frac{1}{l_a}\left[\frac{1}{1+B'}\left(-p_a + p_b + B'_0\right)\right], \quad \left(\frac{\partial p}{\partial y}\right)_b = \frac{U_{1,a}}{U_{1,b}}\left(\frac{\partial p}{\partial y}\right)_a. \tag{4.30}$$

By substitute the normal pressure gradients into the source term $\boldsymbol{Q}$, Equation 4.6, the complete coupled fluid-panel equation can be obtained. Since the fluid on both sides of the panel is considered, they are affecting each other simultaneously through the panel motion and their variables are dependent. Therefore two fluid elements have to be solved together with the panel. The solutions vector and the source term, for solving Equations 4.17 to 4.19, are combined as

$$\boldsymbol{U} = \left[U_{1,a},\ U_{2,a},\ U_{3,a},\ U_{4,a},\ U_{1,b},\ U_{2,b},\ U_{3,b},\ U_{4,b}\right]^{\intercal}, \tag{4.31}$$

$$\boldsymbol{Q} = \left[Q_{1,a},\ Q_{2,a},\ Q_{3,a},\ Q_{4,a},\ Q_{1,b},\ Q_{2,b},\ Q_{3,b},\ Q_{4,b}\right]^{\intercal}. \tag{4.32}$$

The Jacobian matrix of the source term is found as

$$\frac{\partial \boldsymbol{Q}}{\partial \boldsymbol{U}} = \left[\frac{\partial \boldsymbol{Q}}{\partial U_{1,a}} \quad \frac{\partial \boldsymbol{Q}}{\partial U_{2,a}} \quad \frac{\partial \boldsymbol{Q}}{\partial U_{3,a}} \quad \frac{\partial \boldsymbol{Q}}{\partial U_{4,a}} \quad \frac{\partial \boldsymbol{Q}}{\partial U_{1,b}} \quad \frac{\partial \boldsymbol{Q}}{\partial U_{2,b}} \quad \frac{\partial \boldsymbol{Q}}{\partial U_{3,b}} \quad \frac{\partial \boldsymbol{Q}}{\partial U_{4,b}} \right], \quad (4.33)$$

where

$$\frac{\partial \boldsymbol{Q}}{\partial U_{1,a}} = \begin{bmatrix} 0 \\ 0 \\ \dfrac{\partial Q'_a}{\partial U_{1,a}} \\ \dfrac{U_{3,a}}{U_{1,a}} \dfrac{\partial Q'_a}{\partial U_{1,a}} - \dfrac{U_{3,a}}{{U_{1,a}}^2} Q'_a \\ 0 \\ 0 \\ \dfrac{\partial Q'_b}{\partial U_{1,a}} \\ \dfrac{U_{3,b}}{U_{1,b}} \dfrac{\partial Q'_b}{\partial U_{1,a}} \end{bmatrix}, \qquad \frac{\partial \boldsymbol{Q}}{\partial U_{2,a}} = \begin{bmatrix} 0 \\ 0 \\ \dfrac{\partial Q'_a}{\partial U_{2,a}} \\ \dfrac{U_{3,a}}{U_{1,a}} \dfrac{\partial Q'_a}{\partial U_{2,a}} \\ 0 \\ 0 \\ \dfrac{\partial Q'_b}{\partial U_{2,a}} \\ \dfrac{U_{3,b}}{U_{1,b}} \dfrac{\partial Q'_b}{\partial U_{2,a}} \end{bmatrix},$$

$$\frac{\partial \boldsymbol{Q}}{\partial U_{3,a}} = \begin{bmatrix} 0 \\ 0 \\ \dfrac{\partial Q'_a}{\partial U_{3,a}} \\ \dfrac{U_{3,a}}{U_{1,a}} \dfrac{\partial Q'_a}{\partial U_{3,a}} + \dfrac{1}{U_{1,a}} Q'_a \\ 0 \\ 0 \\ \dfrac{\partial Q'_b}{\partial U_{3,a}} \\ \dfrac{U_{3,b}}{U_{1,b}} \dfrac{\partial Q'_b}{\partial U_{3,a}} \end{bmatrix}, \qquad \frac{\partial \boldsymbol{Q}}{\partial U_{4,a}} = \begin{bmatrix} 0 \\ 0 \\ \dfrac{\partial Q'_a}{\partial U_{4,a}} \\ \dfrac{U_{3,a}}{U_{1,a}} \dfrac{\partial Q'_a}{\partial U_{4,a}} \\ 0 \\ 0 \\ \dfrac{\partial Q'_b}{\partial U_{4,a}} \\ \dfrac{U_{3,b}}{U_{1,b}} \dfrac{\partial Q'_b}{\partial U_{4,a}} \end{bmatrix},$$

$$\frac{\partial \boldsymbol{Q}}{\partial U_{1,b}} = \begin{bmatrix} 0 \\ 0 \\ \dfrac{\partial Q'_a}{\partial U_{1,b}} \\ \dfrac{U_{3,a}}{U_{1,a}} \dfrac{\partial Q'_a}{\partial U_{1,b}} \\ 0 \\ 0 \\ \dfrac{\partial Q'_b}{\partial U_{1,b}} \\ \dfrac{U_{3,b}}{U_{1,b}} \dfrac{\partial Q'_b}{\partial U_{1,b}} - \dfrac{U_{3,b}}{{U_{1,b}}^2} Q'_b \end{bmatrix}, \qquad \frac{\partial \boldsymbol{Q}}{\partial U_{2,b}} = \begin{bmatrix} 0 \\ 0 \\ \dfrac{\partial Q'_a}{\partial U_{2,b}} \\ \dfrac{U_{3,a}}{U_{1,a}} \dfrac{\partial Q'_a}{\partial U_{2,b}} \\ 0 \\ 0 \\ \dfrac{\partial Q'_b}{\partial U_{2,b}} \\ \dfrac{U_{3,b}}{U_{1,b}} \dfrac{\partial Q'_b}{\partial U_{2,b}} \end{bmatrix},$$

$$\frac{\partial \boldsymbol{Q}}{\partial U_{3,b}} = \begin{bmatrix} 0 \\ 0 \\ \dfrac{\partial Q'_a}{\partial U_{3,b}} \\ \dfrac{U_{3,a}}{U_{1,a}} \dfrac{\partial Q'_a}{\partial U_{3,b}} \\ 0 \\ 0 \\ \dfrac{\partial Q'_b}{\partial U_{3,b}} \\ \dfrac{U_{3,b}}{U_{1,b}} \dfrac{\partial Q'_b}{\partial U_{3,b}} + \dfrac{1}{U_{1,b}} Q'_b \end{bmatrix}, \qquad \frac{\partial \boldsymbol{Q}}{\partial U_{4,b}} = \begin{bmatrix} 0 \\ 0 \\ \dfrac{\partial Q'_a}{\partial U_{4,b}} \\ \dfrac{U_{3,a}}{U_{1,a}} \dfrac{\partial Q'_a}{\partial U_{4,b}} \\ 0 \\ 0 \\ \dfrac{\partial Q'_b}{\partial U_{4,b}} \\ \dfrac{U_{3,b}}{U_{1,b}} \dfrac{\partial Q'_b}{\partial U_{4,b}} \end{bmatrix},$$

$$Q'_a = -\left(\frac{\partial p}{\partial y}\right)_a, \qquad Q'_b = -\left(\frac{\partial p}{\partial y}\right)_b$$

$$\frac{\partial Q'_a}{\partial U_{1,a}} = \frac{1}{l_a\left(1+B'\right)}\left(\frac{l_a B' Q'_a}{U_{1,a}} - \frac{\partial p_a}{\partial U_{1,a}}\right),$$

$$\frac{\partial Q'_b}{\partial U_{1,a}} = \frac{1}{U_{1,a}}\left[-Q'_b + \frac{1}{l_a\left(1+B'\right)}\left(l_a B' Q'_b - U_{1,b}\frac{\partial p_a}{\partial U_{1,a}}\right)\right],$$

$$\frac{\partial Q'_a}{\partial U_{2,a}} = -\frac{1}{l_a\left(1+B'\right)}\frac{\partial p_a}{\partial U_{2,a}}, \qquad \frac{\partial Q'_b}{\partial U_{2,a}} = -\frac{U_{1,b}}{l_a\left(1+B'\right)U_{1,a}}\frac{\partial p_a}{\partial U_{2,a}},$$

$$\frac{\partial Q'_a}{\partial U_{3,a}} = -\frac{1}{l_a\left(1+B'\right)}\frac{\partial p_a}{\partial U_{3,a}}, \qquad \frac{\partial Q'_b}{\partial U_{3,a}} = -\frac{U_{1,b}}{l_a\left(1+B'\right)U_{1,a}}\frac{\partial p_a}{\partial U_{3,a}},$$

$$\frac{\partial Q'_a}{\partial U_{4,a}} = -\frac{1}{l_a\left(1+B'\right)}\frac{\partial p_a}{\partial U_{4,a}}, \qquad \frac{\partial Q'_b}{\partial U_{4,a}} = -\frac{U_{1,b}}{l_a\left(1+B'\right)U_{1,a}}\frac{\partial p_a}{\partial U_{4,a}},$$

$$\frac{\partial Q'_a}{\partial U_{1,b}} = -\frac{1}{l_a\left(1+B'\right)}\left(\frac{l_b Q'_a}{U_{1,a}} - \frac{\partial p_b}{\partial U_{1,b}}\right),$$

$$\frac{\partial Q'_b}{\partial U_{1,b}} = \frac{Q'_b}{U_{1,b}} - \frac{1}{l_a\left(1+B'\right)U_{1,a}}\left(l_b Q'_b - U_{1,b}\frac{\partial p_b}{\partial U_{1,b}}\right),$$

$$\frac{\partial Q'_a}{\partial U_{2,b}} = \frac{1}{l_a\left(1+B''\right)}\frac{\partial p_b}{\partial U_{2,b}}, \qquad \frac{\partial Q'_b}{\partial U_{2,b}} = \frac{U_{1,b}}{l_a\left(1+B''\right)U_{1,a}}\frac{\partial p_b}{\partial U_{2,b}},$$

$$\frac{\partial Q'_a}{\partial U_{3,b}} = \frac{1}{l_a\left(1+B'\right)}\frac{\partial p_b}{\partial U_{3,b}}, \qquad \frac{\partial Q'_b}{\partial U_{3,b}} = \frac{U_{1,b}}{l_a\left(1+B'\right)U_{1,a}}\frac{\partial p_b}{\partial U_{3,b}},$$

$$\frac{\partial Q'_a}{\partial U_{4,b}} = \frac{1}{l_a\left(1+B'\right)}\frac{\partial p_b}{\partial U_{4,b}}, \qquad \frac{\partial Q'_b}{\partial U_{4,b}} = \frac{U_{1,b}}{l_a\left(1+B'\right)U_{1,a}}\frac{\partial p_b}{\partial U_{4,b}},$$

$$\frac{\partial p_a}{\partial U_{1,a}} = \frac{\gamma-1}{2{U_{1,a}}^2}\left({U_{2,a}}^2 + {U_{3,a}}^2\right), \qquad \frac{\partial p_b}{\partial U_{1,b}} = \frac{\gamma-1}{2{U_{1,b}}^2}\left({U_{2,b}}^2 + {U_{3,b}}^2\right),$$

$$\frac{\partial p_a}{\partial U_{2,a}} = -\left(\gamma-1\right)\frac{U_{2,a}}{U_{1,a}}, \qquad \frac{\partial p_b}{\partial U_{2,b}} = -\left(\gamma-1\right)\frac{U_{2,b}}{U_{1,b}},$$

$$\frac{\partial p_a}{\partial U_{3,a}} = -\left(\gamma-1\right)\frac{U_{3,a}}{U_{1,a}}, \qquad \frac{\partial p_b}{\partial U_{3,b}} = -\left(\gamma-1\right)\frac{U_{3,b}}{U_{1,b}},$$

$$\frac{\partial p_a}{\partial U_{4,a}} = \frac{\partial p_b}{\partial U_{4,b}} = \gamma - 1.$$

In the case of the fluid below the panel is stationary that gives $p_{\mathrm{panel},b} = p_0$ and $\tau_{yy,b} = 0$, only the fluid above the panel is requested to calculate and the normal pressure gradient can be simplified as

$$\left(\frac{\partial p}{\partial y}\right)_a = -\frac{U_{1,a}}{l_a U_{1,a} - B''}\left(-p_a + B''_0\right), \tag{4.34}$$

where

$$B'' = \rho_p h_p + \frac{\Delta t}{2}\left(C + \frac{4}{3}\frac{M}{Re}\frac{\mu_a}{l_a}\right) + \frac{\Delta t^2}{4}K_p,$$

$$B_0'' = \frac{4}{3}\frac{M}{Re}\frac{\mu_a}{l_a}\frac{U_{3,a}}{U_{1,a}} - \left(C + \frac{4}{3}\frac{M}{Re}\frac{\mu_a}{l_a}\right)\left(\frac{\Delta t}{2}\ddot{w}^{j-1} + \dot{w}^{j-1}\right) - K_p\left(\frac{\Delta t^2}{4}\ddot{w}^{j-1} + \Delta t\dot{w}^{j-1} + w^{j-1}\right) - D\frac{\partial^4 w}{\partial x^4} + (T_x + N_x)\frac{\partial^2 w}{\partial x^2} + p_0.$$

The solutions vector and the source term are remained as $\boldsymbol{U} = [U_1,\ U_2,\ U_3,\ U_4]^\intercal$ and $\boldsymbol{Q} = [Q_1,\ Q_2,\ Q_3,\ Q_4]^\intercal$ respectively, and the Jacobian matrix of the source term is

$$\frac{\partial \boldsymbol{Q}}{\partial \boldsymbol{U}} = \begin{bmatrix} 0 & 0 & 0 & 0 \\ 0 & 0 & 0 & 0 \\ \dfrac{\partial Q'}{\partial U_1} & \dfrac{\partial Q'}{\partial U_2} & \dfrac{\partial Q'}{\partial U_3} & \dfrac{\partial Q'}{\partial U_4} \\ \dfrac{U_3}{U_1}\dfrac{\partial Q'}{\partial U_1} - \dfrac{U_3}{{U_1}^2}Q' & \dfrac{U_3}{U_1}\dfrac{\partial Q'}{\partial U_2} & \dfrac{U_3}{U_1}\dfrac{\partial Q'}{\partial U_3} + \dfrac{1}{U_1}Q' & \dfrac{U_3}{U_1}\dfrac{\partial Q'}{\partial U_4} \end{bmatrix}, \tag{4.35}$$

where

$$Q' = -\left(\frac{\partial p}{\partial y}\right)_a,$$

$$\frac{\partial Q'}{\partial U_1} = \frac{1}{l_a U_1 - B''}\left[\frac{-B''Q'}{U_1} + U_1\left(-\frac{\partial p}{\partial U_1} + \frac{4}{3}\frac{\mu}{l_a}\frac{\partial v}{\partial U_1}\right)\right],$$

$$\frac{\partial Q'}{\partial U_2} = \frac{U_1}{l_a U_1 - B''}\left(-\frac{\partial p}{\partial U_2} + \frac{4}{3}\frac{\mu}{l_a}\frac{\partial v}{\partial U_2}\right),$$

$$\frac{\partial Q'}{\partial U_3} = \frac{U_1}{l_a U_1 - B''}\left(-\frac{\partial p}{\partial U_3} + \frac{4}{3}\frac{\mu}{l_a}\frac{\partial v}{\partial U_3}\right),$$

$$\frac{\partial Q'}{\partial U_4} = -\frac{U_1}{l_a U_1 - B'}\frac{\partial p}{\partial U_4},$$

$$\frac{\partial p}{\partial U_1} = \frac{\gamma - 1}{2{U_1}^2}\left({U_2}^2 + {U_3}^2\right), \qquad \frac{\partial p}{\partial U_2} = -\left(\gamma - 1\right)\frac{U_2}{U_1},$$

$$\frac{\partial p}{\partial U_3} = -\left(\gamma - 1\right)\frac{U_3}{U_1}, \qquad \frac{\partial p}{\partial U_4} = \gamma - 1.$$

4.2.3 Boundary conditions

The fluid motion is stopped by no-slip rigid surfaces when they are in contact, so that gives zero normal and tangential velocities $u = v = 0$. Other settings are same as the sliding boundary surfaces described in Section 2.3.1, i.e. isothermal condition $T = T_0$ for all solid surfaces. All solid surfaces also obey the tangency condition and the normal pressure gradient condition.

The near wall approach (Lam et al. 2014a) is applied to determine the ghost point setting, which assumed the fluid-panel interface is located at the ghost point. Therefore the normal velocities and pressure at the ghost point are set as same as that at the fluid-panel interface, so

$$u_G = 0, \qquad v_G = \dot{w}, \qquad p_G = p_{panel}. \tag{4.36}$$

The density can also be determined by isothermal condition,

$$\rho_G = \frac{\gamma p_G}{T_0}. \tag{4.37}$$

All tangential gradients are simply assumed same as in the corresponding boundary point,

$$\left(\frac{\partial \boldsymbol{U}}{\partial x}\right)_G = \frac{\partial \boldsymbol{U}}{\partial x}, \tag{4.38}$$

and all normal gradients are approximated as,

$$\left(\frac{\partial \boldsymbol{U}}{\partial y}\right)_G = \frac{\boldsymbol{U} - \boldsymbol{U}_G}{2\delta}. \tag{4.39}$$

In summary, no-slip flexible panel boundary condition is set as,

$$\begin{aligned}
&u_G = 0, && \left(\frac{\partial u}{\partial x}\right)_G = \frac{\partial u}{\partial x}, && \left(\frac{\partial u}{\partial y}\right)_G = \frac{u}{2\delta},\\
&v_G = \dot{w}, && \left(\frac{\partial v}{\partial x}\right)_G = \frac{\partial v}{\partial x}, && \left(\frac{\partial v}{\partial y}\right)_G = \frac{v - \dot{w}}{2\delta},\\
&p_G = p_{\text{panel}}, && \left(\frac{\partial p}{\partial x}\right)_G = \frac{\partial p}{\partial x}, && \left(\frac{\partial p}{\partial y}\right)_G = \frac{p - p_G}{2\delta},\\
&\rho_G = \frac{\gamma p_G}{T_0}, && \left(\frac{\partial \rho}{\partial x}\right)_G = \frac{\partial \rho}{\partial x}, && \left(\frac{\partial \rho}{\partial y}\right)_G = \frac{\rho - \rho_G}{2\delta}.
\end{aligned}$$

Table 4.1: Comparison of two approaches for third eigenmode vibration.

	f	D_f
Theory	1.4921	
Partitioned approach	1.4975	0.36 %
Monolithic approach	1.4916	0.03 %

To avoid error generated by any discontinuities, the rigid surfaces should be set by the same method by setting zero wall velocity $\dot{w} = 0$ and zero pressure difference $p - p_G = 0$. In addition, this ghost point setting method can also be applied for sliding boundary surface by setting $u_G = u$ and $(\partial u/\partial y)_G = 0$.

4.3 Comparisons of partitioned and monolithic approaches

The accuracy and computational time of both partitioned and monolithic approaches are tested and compared in this section. Three cases are selected and computed by both approaches for comparisons: a fluid loaded panel vibration case, and two acoustic-structural interaction cases with high and low transmission loss TL respectively. The most basic problem is the fluid loaded panel vibration that can test the ability for capturing structural response. The related theory can be referred in Section 2.5. Here the third eigenmode is selected for testing, the eigenmode frequencies f and the absolute differences to the theory D_f are shown and compared in Table 4.1. The result of monolithic approach is more accurate than the partitioned approach for the structural response.

Another two tests are the acoustic-structural interaction problems in a duct with membrane length $L_p/H = 5$ and 3.4, that can test the ability of

Table 4.2: Comparison of two approaches for acoustic-structural interaction in duct.

L_p/H	5			
	TL	ΔTL	T_{comp}	N_{iter}
Theory	15			
Partitioned scheme	14.8	0.2	0.03415 s	18
Monolithic scheme	14.7	0.3	0.01695 s	4
L_p/H	3.4			
	TL	ΔTL	T_{comp}	N_{iter}
Theory	2.5			
Partitioned scheme	1.8	0.7	0.03810 s	18
Monolithic scheme	2.7	0.2	0.01710 s	3

capturing acoustic response. The details of the cases setting and the result discussion can be referred to Section 3.1.1. The TL and its absolute differences $\Delta TL = |TL_{numerical} - TL_{theoretical}|$ of both cases are shown in Tables 4.2. The results show both approaches have similar accuracy for capturing high TL response. However, the monolithic approach has higher accuracy for capturing low TL response. These test cases concluded that the monolithic approach has higher accuracy for capturing both structural and acoustic responses in general. In addition, the time efficiency is also compared. For a fair comparison, only the computational time consumed for panel dynamic solver and coupling procedure in partitioned approach, and for the procedure of resolving fluid-panel coupled equation in monolithic approach are accounted. The computational time per time step T_{comp}, number of iteration steps per time step N_{iter} of two approaches are shown in Table 4.2. The number of iteration steps by monolithic approach

is much lesser. The time consumed is also only 50 % of that by the partitioned approach. The monolithic approach has double time efficiency compare to the partitioned approach. In summary, the monolithic approach is definitely superior to the partitioned approach in both accuracy and time efficiency.

Chapter 5

Aeroacoustic-Structural Interaction in Duct Carrying Viscous Flow

The capability of the numerical methodology is going to be assessed by comparing the results with the data of two experiments. The experimental study on aeroacoustic-structural interaction with acoustic excitation by Choy and Huang (2005) and study on flow-induced vibration by Liu (2011) are selected as canonical problems. The viscous effect and any responses cannot measure from the experiments are further discussed in detail.

5.1 Aeroacoustic-structural interaction

The numerical methodology is firstly validated its capability in capturing the acoustic and panel responses in the aeroacoustic-structural interaction. The experimental study of Choy and Huang (2005) on the drum-like silencer carrying a low Mach number flow is selected as the benchmark for the validation. They measured the transmission loss and the distribution of vibrating velocities that

can be used to validate the acoustic and panel responses. The drum-like silencer is a kind of duct silencer that developed based on the theoretical study of Huang (1999). Flexible duct segment constructed by membranes is utilized to reflect noise in the flow duct. There are two opposing side-branch cavities covered with flexible panels in the silencer design to improve the silencer performance and block the noise radiation to the duct exterior. This configuration is more complex than that in Figure 3.1 in Chapter 3, and presents a more stringent case for the validation of coupled aeroacoustic-structural interaction. The experiment is summarized in the following.

5.1.1 Summary of the experiment

The aim of the experiment was to measure the transmission loss resulted by the drum-like silencer. The setup of the experiment is illustrated in Figure 5.1 (from Choy and Huang 2005). The experiment was conducted in a closed-loop wind tunnel with acoustic linings to absorbed the noise generated by the fan. A 500 mm long drum-like silencer was installed in a straight duct that the length from the inlet (connected to the nozzle) to the outlet (connected to the diffuser) was 2370 mm and the cross-section was 100 mm by 100 mm. In the drum-like silencer, two membranes were flush-mounted in the duct the backed with 100 mm height cavities. A loudspeaker was flush-mounted at the silencer's upstream and produces pure tone sound from 20 to 1000 Hz with a frequency interval of 10 Hz. Four microphones, one pair in upstream and one pair in downstream, were used to measure the sound level and distinguish its travelling directions so to find the transmission loss. The tension of the membrane was measured by a strain gauge glued to its surface. A laser vibrometer was used to measure the membrane vibration through the transparent cavity walls. The vibration velocity was captured point by point in streamwise direction with an interval of 20 mm. The

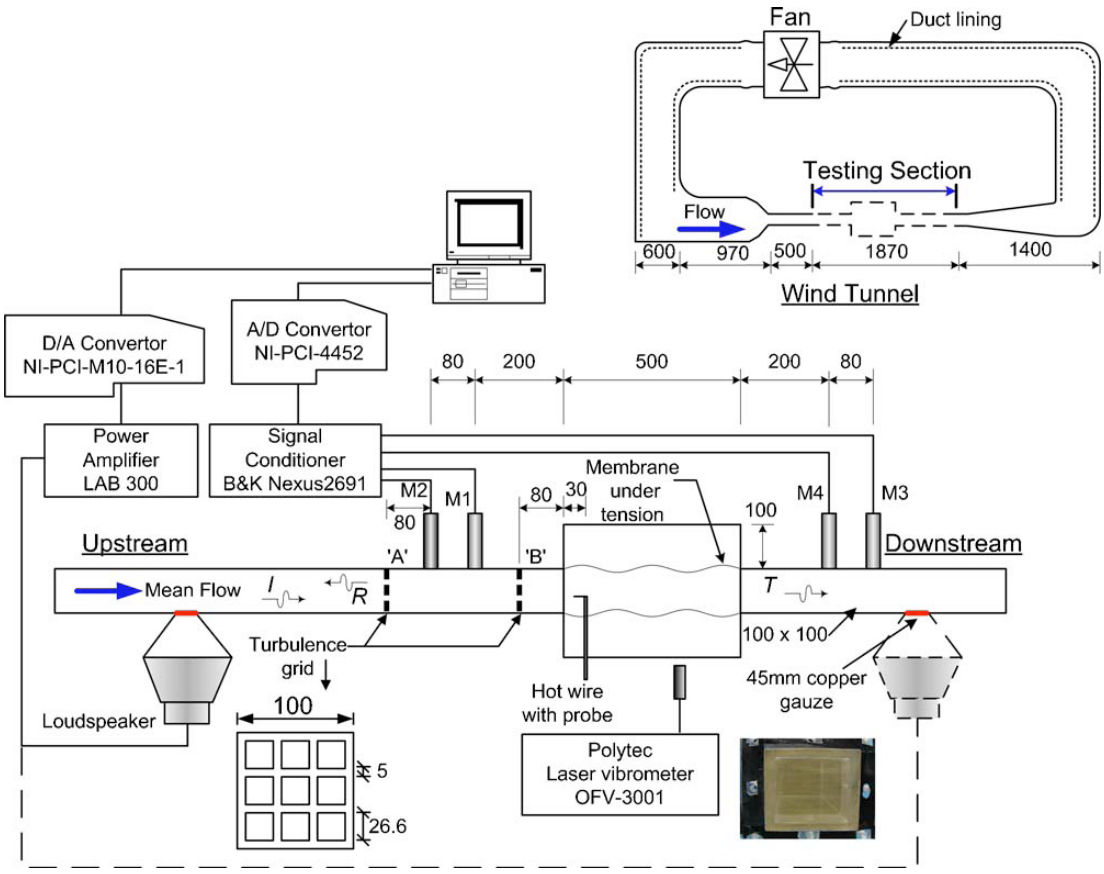

Figure 5.1: The schematic setup of the testing rig from Choy and Huang (2005). The upper right corner is the overview of the wind tunnel. The unit of the dimensions shown in the figure is mm.

distribution of the vibration velocity was than reconstructed by corrected phase. The turbulence grids in upstream and the loudspeaker at downstream were used for the other measurements that will not adopted in the following discussion, so they are not explained here.

5.1.2 Validation of the methodology

The same set of experiment parameters are taken for the calculation, i.e. the panel and cavity length $\hat{L}_p = 500$ mm, the duct width and cavity height $\hat{H} = 100$ mm, the upstream and downstream length are 1000 and 870 mm respectively and the

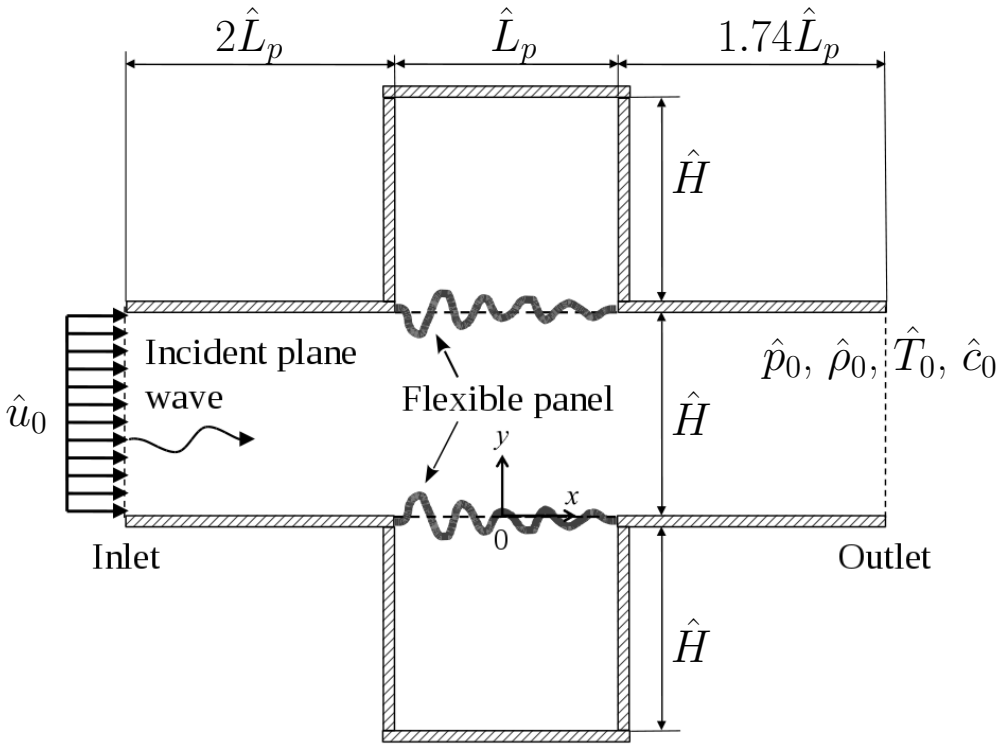

Figure 5.2: Schematic configuration of the drum-like silencer (not-to-scale).

panel mass per unit area $\hat{\rho}_p\hat{h}_p = 0.17$ kg/m^2. The range of testing frequencies is from 20 to 1000 Hz with an interval of 10 Hz. The panel tension and mean flow speed are case dependence, they will be mentioned with the results. $\hat{L}_0 =$ panel length $\hat{L}_p$, ambient acoustic velocity $\hat{c}_0 = 340$ m/s, time $\hat{t}_0 = \hat{L}_0/\hat{c}_0$, ambient density $\hat{\rho}_0 = 1.225$ kg/m^3, pressure $\hat{\rho}_0\hat{c}_0^2$, and ambient temperature $\hat{T}_0$ are chosen for the normalization of all flow and panel variables. The two-dimensional computational domain of the silencer geometry is shown in Figure 5.2. The ambient density, pressure, and temperature are fixed at the outlet. The no-slip condition is applied to all wall and flexible panel surfaces. A broadband incident acoustic plane wave covering 0.0294 to 1.4706 with a frequency resolution $\Delta f = 0.0147$ was introduced into the computational domain. The excitation

functions are written as,

$$p'_{inc} = p_A \sum_{n=1}^{99} \sin(2\pi t f_n + \theta_n), \tag{5.1}$$

$$u'_{inc} = p'_{inc}/\rho, \tag{5.2}$$

where $p_A = 4.5e^{-4}$ (110 dB), which is constant to all f_n, and θ_n is uniformly random phase. A uniform flow profile is applied at the inlet to let the boundary layer freely develop. A full rigid duct case is first calculated to develop the proper flow profile in the whole flow field. The steady solution is then used as the initial condition for the calculation with the flexible panels. The pressure in the duct is spatially decreasing along the duct. Since the cavities are located below/above the panels, the initial pressure in the cavities is set as the same as the pressure in the duct at the centre of the panels ($x = 0$). Therefore the pressure difference ($p_{ex} = 0$ at the centre of the panels) across the panels can be minimized initially. This is to simulate the experimental set-up and avoid large deflection of the panel by the static pressure that affects the later excited panel response. Zero mean flow velocity is also set in the cavities. In the mesh, uniform grid distribution is used for both x and y directions with $\Delta x = 0.02$ and $\Delta y = 0.0033$.

The instantaneous distribution of vibrating velocities of a tensioned panel with $T = 0.108$ (8213.38 N) excited by acoustic wave under flow $M = 0.026$ ($\hat{u}_0 = 9$ m/s) are measured in the experiment. Figure 5.3 shows the comparisons of numerical result with excitation frequencies $f = 0.294$ (200 Hz) and 0.618 (420 Hz) and the experimental data. The numerical results have good agreement with the experimental data at both frequencies. The maximum differences are 5.2% and 10.8% in the results of $f = 0.294$ and 0.618 respectively.

On the other hand, four comparisons of the calculated transmission loss TL and the experimental data with are illustrated in the following. First, Figure 5.4 shows the case with $T_x = 0.116$ (8821.78 N) and $M = 0.045$ ($\hat{u}_0 = 15$ m/s). An

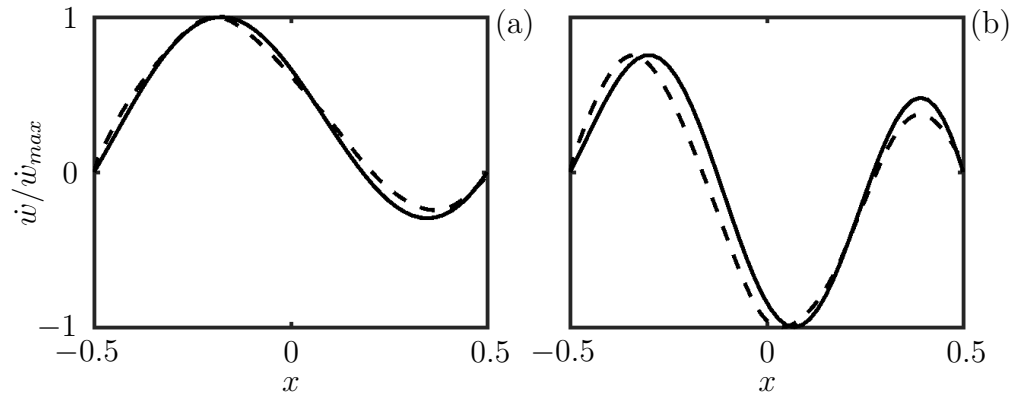

Figure 5.3: Comparison of instantaneous distribution of vibrating velocities with $T = 0.108$ and $M = 0.026$. (a), $f = 0.294$ (200 Hz). (b), $f = 0.618$ (420 Hz). ——, numerical result; – – –, experimental data (Choy and Huang 2005).

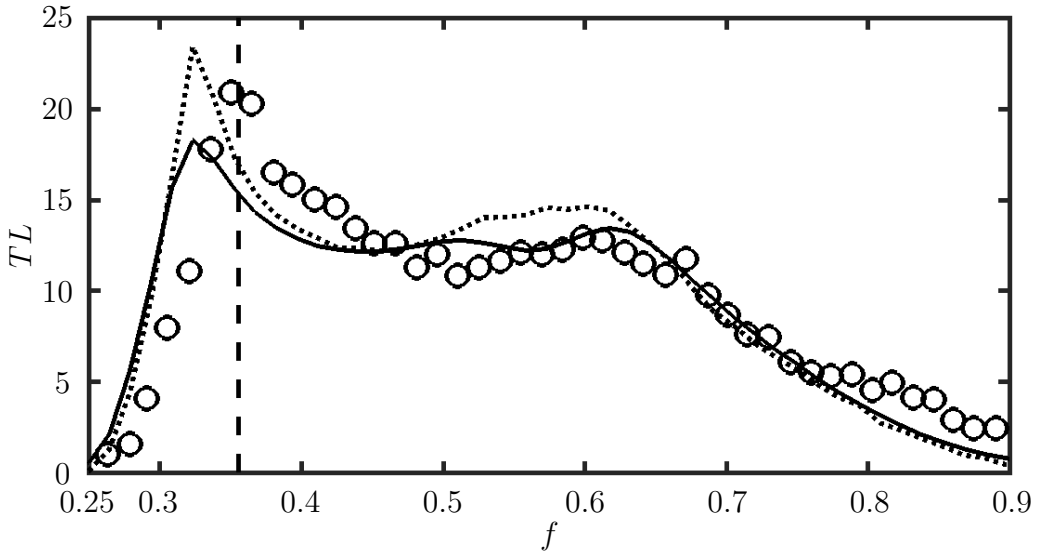

Figure 5.4: Comparison of the TL spectrum of numerical result to experimental data with $T = 0.116$ and $M = 0.045$. ——, numerical result with viscous flow; · · · · · ·, numerical result with inviscid flow; ◯, experimental data (Choy and Huang 2005). – – –, duct mode frequency $f_{2,0,0}$.

excellent agreement between the numerical results and the experimental data is found except the peak at $f = 0.36$. The numerical result is around 5 db lower. However the difference at this peak is found that may caused by a wind tunnel duct mode in a section with 2.74 (1.37 m) long that counted from the flexible panel leading edge to the duct outlet. In the experiment, the test section outlet is connected to a diffuser and acoustic reflection may be caused by the change of cross-section area. On the other hand, reflection may also be caused by the panel vibration at the leading edge. Therefore duct mode may occur within this section. The frequency of a duct mode can be found by the following equation,

$$f_{n_1,n_2,n_3} = \frac{c_0}{2}\left(\frac{{n_1}^2}{(l_1+2l'')^2} + \frac{{n_2}^2}{{l_2}^2} + \frac{{n_3}^2}{{l_3}^2}\right)^{\frac{1}{2}}, \tag{5.3}$$

where, c_0 is speed of sound, l_1, l_2 and l_3 are the lengths, hight and width of the duct respectively, n_1, n_2 and n_3 are the mode numbers of each directions respectively, and l'' is the end correction. When resonance occurs in a closed ends duct, the pressure is constant at its ends and the wavelength will be a factor of the physical length of the duct. However in an open ends duct, the air at the ends is oscillating and the pressure cannot be constant, so the effective length of the duct will be a bit longer than its physical length (Beranek 1993, Dowling and Ffowcs Williams 1983). Therefore the end correction is necessary for each ends to estimate the effective length. The end correction can be approximately determined as (Beranek 1993),

$$\hat{l}'' = 0.613\hat{a} \qquad \text{if } \hat{k}\hat{a} < 0.5, \tag{5.4}$$

where, $\hat{a} = \sqrt{\hat{S}/\pi}$ is the characteristic dimension of the cross section of the duct with the cross-sectional area $\hat{S}$, and $\hat{k} = 2\pi/\hat{\lambda}$. In the experiment, the cross-sectional area of duct $\hat{S} = 0.01$ m^2 and $\hat{a} = 0.0564$ m. Hence the end correction is $\hat{l}'' = 0.0346$ m. When $n_1 = 2$, the wavelength $\hat{\lambda} = 1.40$ m and $\hat{k}\hat{a} = 0.252 < 0.5$ that meets the condition. By Equation 5.3, the frequency of the second mode

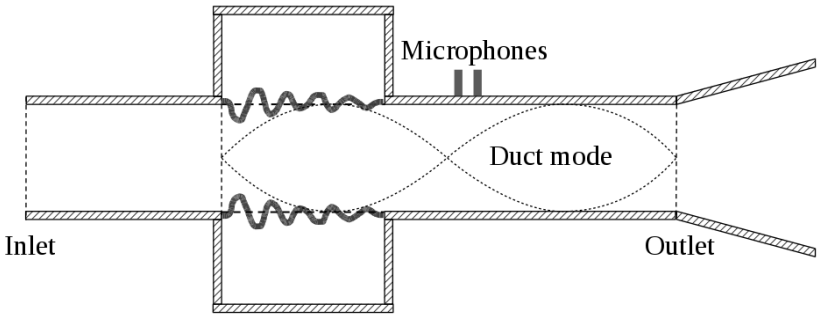

Figure 5.5: Illustration of the occurrence of second duct mode pressure distribution in the experiment.

$\hat{f}_{2,0,0} = 242$ Hz, i.e. $f_{2,0,0} = 0.36$. If the second mode occur in this section of the wind tunnel, the nodal point of this mode will be located at 15 mm away from the microphone at the downstream as shown as Figure 5.5. When the microphone is such close to the nodal point, the acoustic signal received will be much lesser then the actual acoustic wave transmitted to the downstream. The TL measured will also higher than the actual one. However, in the computational domain, the outlet is connected to a high numerical dissipative section that ensure there is no acoustic reflection, so no duct mode will be formed. Therefore the numerical result is not affected by this duct mode problem. Since $f_{2,0,0}$ is exactly agrees with the peak of the TL spectrum as shown as Figure 5.4, this may be a possible reason that the TL level at $f = 0.36$ measured in the experiment is higher than the numerical result.

Figure 5.6 shows the TL spectra of the cases with $T_x = 0.108$ (8213.38 N) and $M = 0$, 0.03 ($\hat{u}_0 = 10$ m/s) and 0.045 ($\hat{u}_0 = 15$ m/s). They also show very good agreement between the numerical results and the experimental data. Similar to the aforementioned case, some peaks (or dips) are not captured by the calculations but they are probably caused by wind tunnel duct modes. The peak at around $f_{2,0,0}$ is measured in all three cases but not found in the calculations

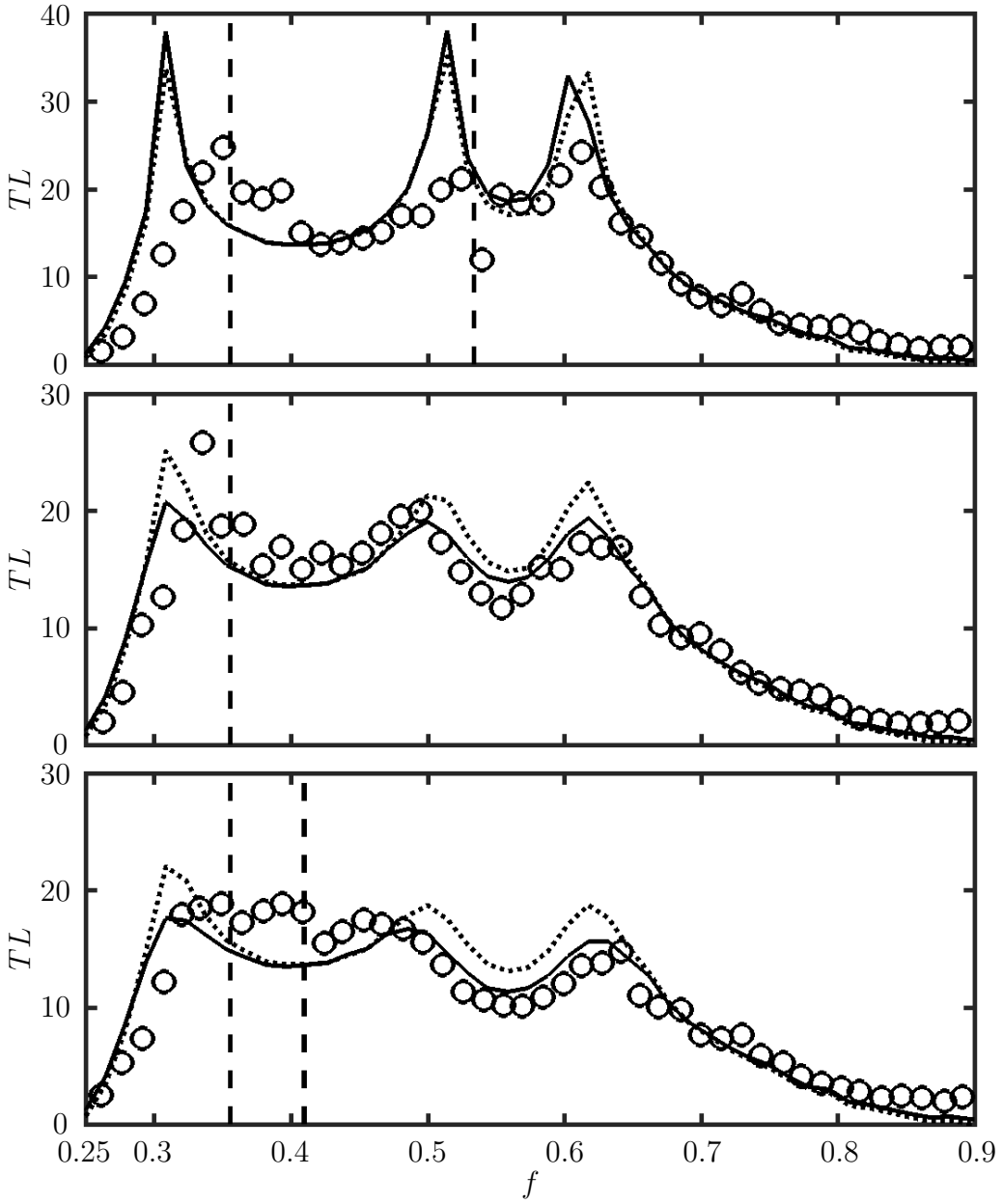

Figure 5.6: Comparisons of the TL spectra of numerical result to experimental data with $T = 0.108$. (a), $M = 0$; – – –, duct mode frequency $f_{2,0,0}$ and $f_{3,0,0}$. (b), $M = 0.03$; – – –, duct mode frequency $f_{2,0,0}$. (c), $M = 0.045$; – – –, duct mode frequency $f_{2,0,0}$ and $f_{4,0,0}$. ——, numerical result with viscous flow; $\cdots\cdots$, numerical result with inviscid flow; ◯, experimental data (Choy and Huang 2005).

which may be caused by the mode of duct section counted from the flexible panel leading edge to the duct outlet. For $M = 0$, the dip at $f = 0.53$ is also match with the third duct mode $f_{3,0,0}$ of the same duct section. The anti-nodal point of this third mode is located at 15 mm away from the microphone at the downstream. Contrary to the second mode, the acoustic signal received will be much larger than the actual transmitted. Therefore the TL measured will be lower and a dip is found at $f_{3,0,0}$ in the experimental TL spectrum. For $M = 0.045$, the experimental data are 4.5 db higher than the numerical result at $f = 0.41$. It is match with the fourth mode of another section with 4.74 (2.37 m) long that counted from the duct inlet to outlet. With the length of 4.74, the frequency of forth mode $f'_{4,0,0} = 0.41$. It's last nodal point is located at 2.5 mm away from the microphone at the downstream. Similar to the mode at $f_{2,0,0}$, the TL measured is, therefore, higher than the numerical result.

Except for the influence of the duct modes, the other difference in the TL levels might be attributed to two reasons. One is due to the fact that the present two-dimensional calculation might not approximate fully the three-dimensionality of the experiment. Some three-dimensional panel vibration and duct acoustic modal behaviors might not be properly included. Another is that the mesh is not fine enough to capture the turbulence, any acoustic reactive response caused by the panel vibration driven by flow instability in the experiment might be excluded. In general, the numerical results are agreed with the experimental data very well. These excellent agreement in the spectral variation of TL firmly establishes the capability of the present numerical methodology in capturing aeroacoustic-structural interaction correctly.

To study the viscous effect, the same setting but with inviscid flow is calculated. Euler equation and sliding wall condition for all walls and panels are employed. Figures 5.4 and 5.6 show the comparison of acoustic response of

viscous and inviscid solutions and also the experimental data. When the flow is absent $M = 0$ (Figure 5.6 (a)), two solutions almost overlap which shows the viscous effect is not strong. When the flow is presented to $M = 0.03$ (Figure 5.6 (b)), their overall trend is similar but the inviscid solution have obvious over prediction at around $f = 0.5$ to 0.6 and the peak at $f = 0.32$. This problem is worse in higher flow velocity $M = 0.045$ (Figures 5.4 and 5.6 (c)). Especially at the peak, for example in Figure 5.4, the difference between the inviscid solution and the experimental data is 5.7 db that is much larger than that of viscous solution which is 0.5 db only. The better agreement with the experiment shows that including the viscous effect can provide a more accurate solution for the aeroacoustic-structural interaction.

5.1.3 Aeroacoustic-structural response

Since the aeroacoustic-structural interaction with the acoustic excitation is discussed deeply in Chapter 3, this section will focus on the effect of cavities on the interaction. An additional case without cavities is calculated for reference. The duct external pressure distribution is set as identical to the internal pressure in the steady state with a fully rigid duct. This assumption is to avoid the panels deflection by the static pressure difference and causing any effect to the aeroacoustic-structural response.

An overview of panel response is shown in Figure 5.7 for both cases with and without cavities. Figures 5.7(a) and (b) show the panel response is dominated by the first five in-vacuo modes. The effect of cavities mainly suppresses the response of first three modes, the differences of other modes are not large relatively. In the frequency spectrum as shown as Figure 5.7(c), the response without cavity is dominated at a narrow band around $f = 1$. Two close peaks $f = 1.016$ and 1.059 are found. When the panels are backed by cavities, the

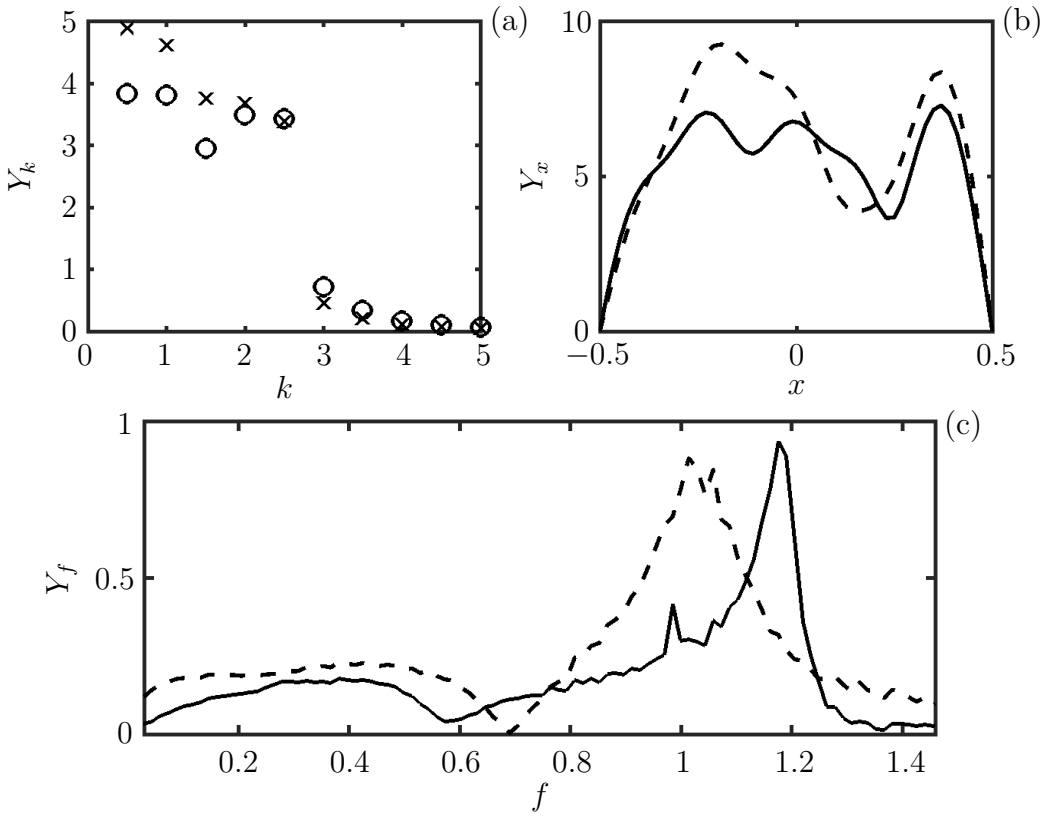

Figure 5.7: Panel responses with $T = 0.116$ and $M = 0.045$. (a), the modal spectrum of panel mobility Y_k. (b), the distributions of panel mobility amplitude Y_x. (c), the averaged frequency spectrum of panel mobility Y_f on the whole panel. ◯ and ——, with cavities; × and – – –, without cavities.

strongest response is shifted to $f = 1.176$ and only a small peak is found at $f = 0.985$. The relationship between the wavenumber and frequency for both cases are shown in the Figure 5.8. Both subsonic and supersonic responses are found in both cases. For the case that with cavities, the subsonic response almost covers all excitation frequency ($f = 0.0294$ to 1.4706). However, the supersonic response mainly appears when $f > 0.9$. By compare Figures 5.8(a) and 5.7(c), the response at $f = 1.18$ is mainly contributed by the supersonic response. The wavenumber of this strongest peak is around $k = 0.2$, the phase speed of the panel wave is $c_B = 5.9$. Since the wavenumber is very close to zero, the panel is almost vibrating with a flat shape. For the subsonic upstream and downstream travelling waves, the strongest responses are at $f = 1.19$ and 1.22 respectively. In addition, the response level of the downstream travelling wave is generally larger than the upstream. This may be because of the directions of flow and the upstream travelling wave are in the opposite. The force applied by the flow was resisting the upstream travelling wave, in contrast, the downstream travelling wave was enhanced. For the case without cavities, the supersonic response mainly appears when $f > 0.77$. Both wavenumbers of two strongest responses at $f = 1.016$ and 1.059 are $k \approx 0$, they are vibrating with flat shapes. For $f < 0.77$, the downstream travelling wave is dominated. By compare Figures 5.8(a) and 5.8(b), some effects of cavities are observed. First, it amplified the upstream travelling wave but attenuated the downstream travelling wave at low frequency. Second, it makes the subsonic response in high frequency dominated in the narrow band around $f = 1.2$. Besides, the dominant frequency of supersonic response also shifted to around $f = 1.2$.

The acoustic responses with and without cavities are shown in Figure 5.9. The result shows that the most effective silencing frequency range is around $1 < f < 1.4$ when cavities were removed. However, when the panel is backed by the

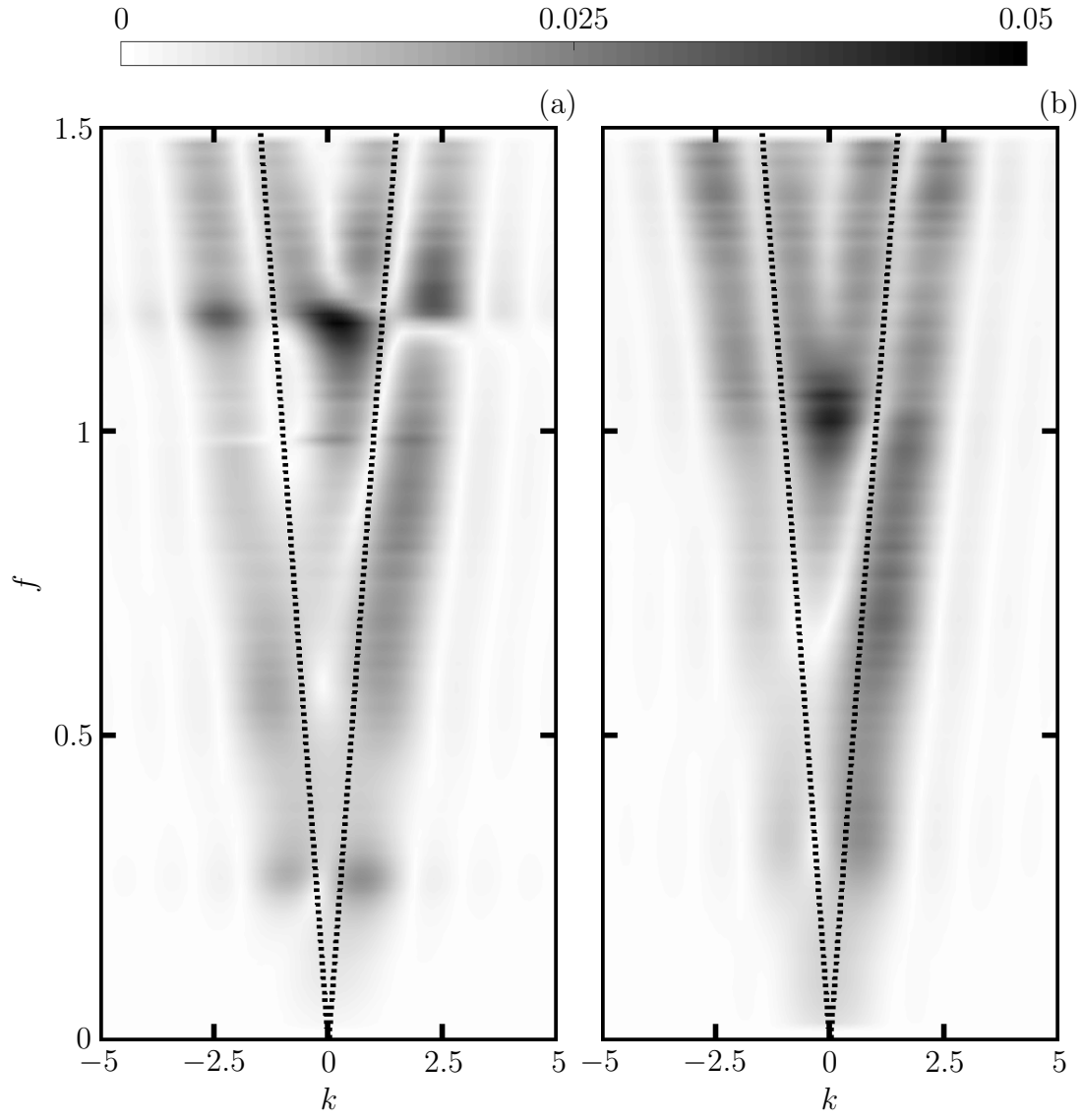

Figure 5.8: Frequency-wavenumber spectrum of $Y_{f,k}$. (a), with cavities. (b), without cavities. ·····, acoustic wave speed in fluid.

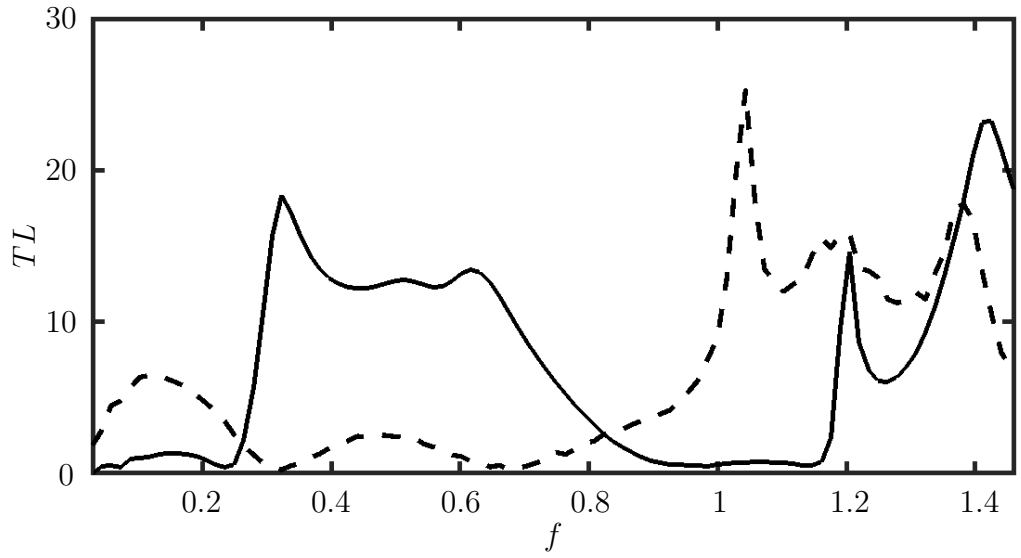

Figure 5.9: Spectral variation of TL. ——, with cavities; – – –, without cavities.

cavities, the effective silencing frequency range is found at around $0.3 < f < 0.7$ and $f > 1.2$. The cavities definitely enhanced the TL at low frequency and change the effective silencing frequency range. However, there is no strong relationship between the acoustic and structural responses is found.

5.2 Flow-induced structural instability

In the case of Section 5.1, the panel vibration is mainly driven by the acoustic wave. To rigorously validate the interaction between flow and panel, the experimental study by Liu (2011) on the instability of flexible panel in drum-like silencer carrying a low Mach number flow is selected as the benchmark for the validation. It is a further study based on the drum-like silencer of Choy and Huang (2005).

5.2.1 Summary of the experiment

The target of the experiment was to investigate the occurrence of the instability of the membrane in drum-like silencer induced by flow. The same closed-loop

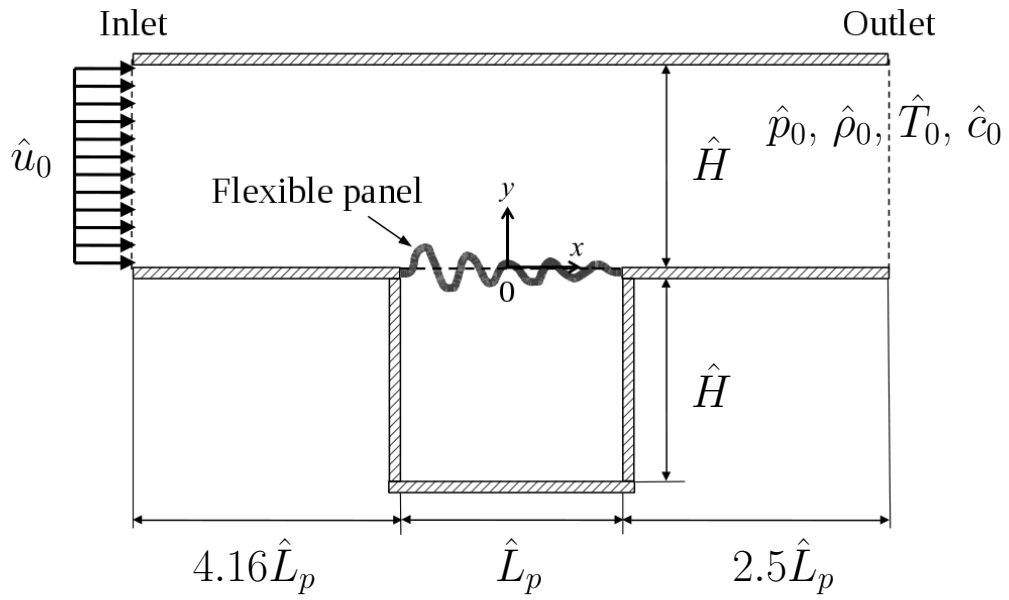

Figure 5.10: Schematic configuration of the experimental setting of Liu (2011) (not-to-scale).

wind tunnel illustrated in Figure 5.1 was used in this experiment. However, two openings, each with dimension 50 mm by 50 mm, were made at the upstream and downstream of the test section so as to simulate a mean pressure drop along the duct similar to those commonly observed in practical ventilating systems. The drum-like silencer here was 300 mm long with only one membrane made of stainless steel and backed by a cavity. The occurrence of the instability was first found by recording the growth of the vibration velocity at the center point of the membrane with flow speed. Then the spectrum of the vibration velocity of the whole membrane during instability was scanned by a vibrometer.

5.2.2 Validation of the methodology

A case with the presence of structural instability is selected for the computation. The computational domain is shown in Figure 5.10. The same set of experiment parameters are taken for the calculation, i.e. the panel and cavity length $\hat{L}_p =$

300 mm, the duct width and cavity height $\hat{H} = 100$ mm, the upstream and downstream length are 1250 and 750 mm respectively, the panel density $\hat{\rho}_p = 7800$ kg/m^3, the panel thickness $\hat{h}_p = 0.025$ mm, the Young's modulus $\hat{E}_p = 193$ GPa, the bending stiffness $\hat{D} = 0.0002762$ Nm, the panel tension $\hat{T}_x = 40$ N and the mean flow speed $\hat{u}_0 = 35$ m/s. There had not any excitation applied on the flexible panel such as acoustic wave, so the vibration was only induced by the flow. The normalization and other setting are same as the last case in Section 5.1. Uniform mesh is used for both x and y directions with $\Delta x = 0.02$ and $\Delta y = 0.0067$. The nonlinearity term N_x in the panel dynamic equation is included in this calculation because the structural instability must induce large deflection. The result in the following sections confirmed that the maximum displacement to thickness ratio $w/h_p = 28 \gg 0.2$ that is over the limit of the small-deflection theory, so N_x cannot be ignored.

It is important to confirm the accuracy of the aeroacoustic model for capturing the background mean velocity profile of the duct flow because the panel vibration is highly affected by the wall normal stress which related to the velocity profile under the action of fluid viscosity. Since Liu (2011) did not provide the data of velocity mean profile at $\hat{u} = 35$ m/s, the experimental data with the closest mean flow speed $\hat{u} = 30$ m/s is selected for comparison. An additional case with $\hat{u} = 30$ m/s have be calculated and compared with the experimental data as shown as Figure 5.11. The Reynolds numbers of the experiment are $Re_H = 2.4 \times 10^5$ and $Re_\delta = 2.3 \times 10^4$ based on duct width and the boundary layer thickness as reference length respectively. The entrance length to become fully developed is 3.4 m (White 1998) which is much longer than the whole test section (2.3 m). Therefore the turbulent flow had not developed in the test section and the boundary layer is laminar. The figure shows the numerical velocity profile agree favorably well with experimental data. The velocity boundary layer

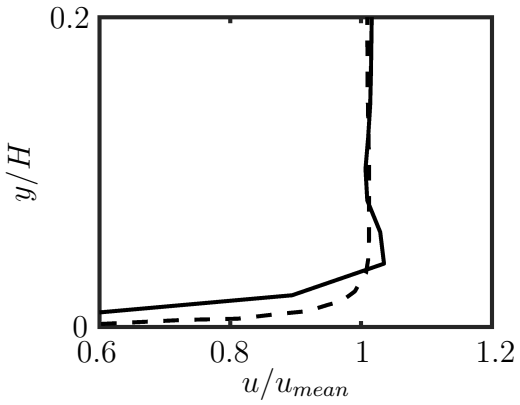

Figure 5.11: Velocity mean profile at the inlet. ——, numerical result. – – –, experimental data (Liu 2011).

thickness in the experiment reported is 11 mm, that is 0.037 in normalized value. The numerical result is 0.039 which is 5% different from the experimental data only. Two profiles also overlap fully in the very close proximity to duct wall, $y/H \leq 0.02$. This comparison provides further support that the aeroacoustic model is able to generate correct mean velocity profile for initiating the correct panel response.

Dynamic instability, known as flutter (Dowell 1975), was observed in the experiment and the frequency spectrum of vibration velocity is reported by Liu (2011). When the panel deformation is large enough, the post-flutter oscillation, that also called limit cycle oscillation, will occur (Dowell 1975). That is because the nonlinear tension will increase with the panel deformation, and that increases the effective panel stiffness. When it balances the fluid forces that excite the panel, the oscillation will keep at a constant level. The time traces of strain ϵ, kinetic energy $KE = (1/2)\rho_p h_p \int_{-0.5}^{0.5} \dot{w}^2 dx$, and vibrating velocity at two locations in the numerical result, one third ($x = -0.17$) and center ($x = 0$) of the panel, are selected as references and shown in Figure 5.12 to illustrate the development of the structural instability. The vibration was excited by the flow at the beginning

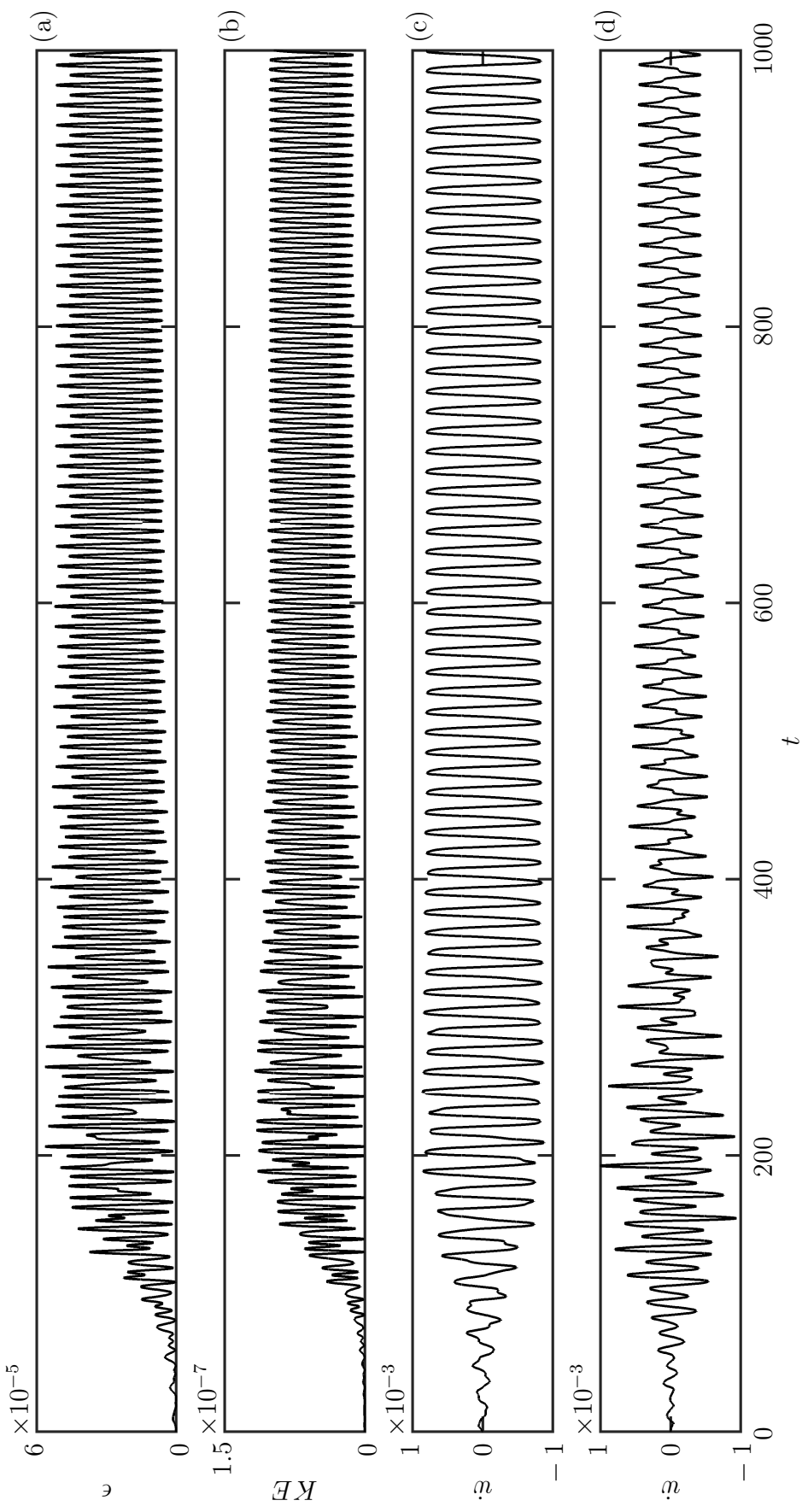

Figure 5.12: Time traces of panel response. (a), strain. (b), kinetic energy. (c) & (d), vibrating velocity at $x = -0.17$ and 0 respectively.

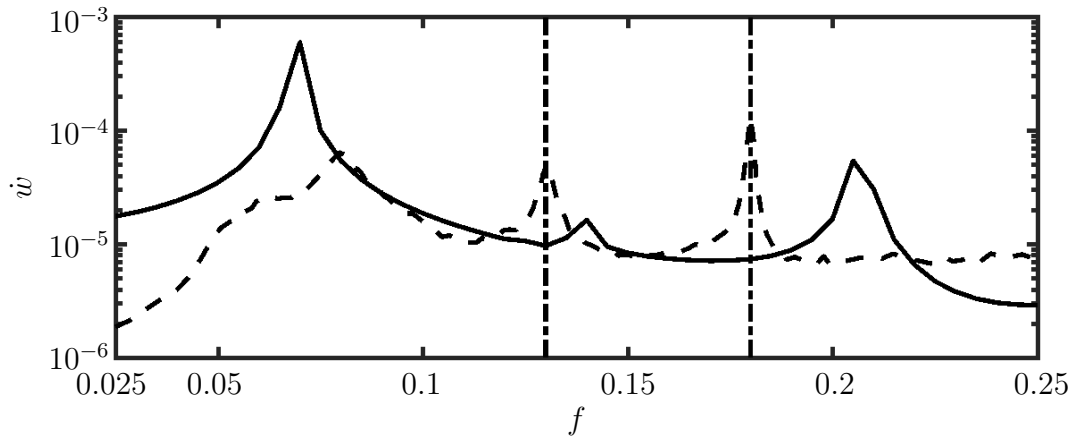

Figure 5.13: Averaged frequency spectrum of the vibration velocity on the whole panel. ——, numerical result; – – –, experimental data (Liu 2011). $- \cdot - \cdot -$, duct mode frequencies.

and the amplitude increases continuously until $t \approx 200$. Then the amplitude started to decrease and tends to keep at a certain level. At last, it enters the time stationary state after $t \approx 800$, and the limit cycle oscillation occurs. Therefore, the following analysis is based on the result in the time stationary state.

The averaged frequency spectrum of the vibration velocity on the whole panel is then compared with the experimental data in Figure 5.13. It shows the favorable agreement of numerical result with the experimental data. The first peak of the numerical result at frequency $f_0 = 0.07$ have -13.5% frequency shift compare to the experiment. The difference may be attributed to the three-dimensionality of the experiment might not be completely approximated by the present two-dimensional calculation. The missing the tension of spanwise direction will reduce the frequencies, that cause the frequency shifted to a lower value. The amplitude in spanwise direction may not be equally distributed that cause the difference in amplitude. Besides, another two peaks of the numerical result are the first and second harmonics of the first peak, where $f = 2f_0$ and $3f_0$. On the other hand, there are another two peaks measured in the experiment but

they are not found in the calculation. However, they may be induced by two different wind tunnel duct modes. If the acoustic wave accumulated and from a duct mode, that may excite the panel to vibrate with the corresponding frequency. First, the length of the duct from the nozzle to the diffuser is 7.67. By Equations 5.3 and 5.4, the frequency of the second mode is found as $f_{2,0,0} = 0.13$ that exactly matches with the second peak in the experimental data. In the numerical calculation, both inlet and outlet are connected to no acoustic reflection section, so no duct mode will be formed. Second, there are two small holes, that the dimensions are $50\ \text{mm} \times 50\ \text{mm}$, located at both upstream and downstream of the flexible panel in the test section in the experiment. Liu (2011) claim they are to simulate the open inlet and discharge condition in a realistic ventilation system. However, they may introduce acoustic reflection and duct mode. The length of the test section is 6 so the length between two holes is approximately around 5.56. The frequency of the second mode is found as $f_{2,0,0} = 0.18$ that exactly matches with the third peak in the experimental data. In the numerical calculation, these holes are neglected in order to maintain the two-dimensional assumption and to identify the pure panel response induced by the flow. Since the width of holes is only half of the duct width, the effect of the holes must be three-dimensional. It is difficult to account this effect in the two-dimensional calculation. In addition, the focus of the present study is the vibration purely induced by the flow, so the effect of holes should be eliminated in the calculation. Because of the aforementioned two possible reasons, the last two peaks measured in the experiment not found in the calculation.

The viscous effect is also highlighted in this case. Figure 5.14 shows the comparison of panel response of viscous and inviscid solutions. The inviscid solution obviously has a worse agreement with the experiment. The first peak $f = 0.065$ is -19.8% difference to the experimental data that is much larger

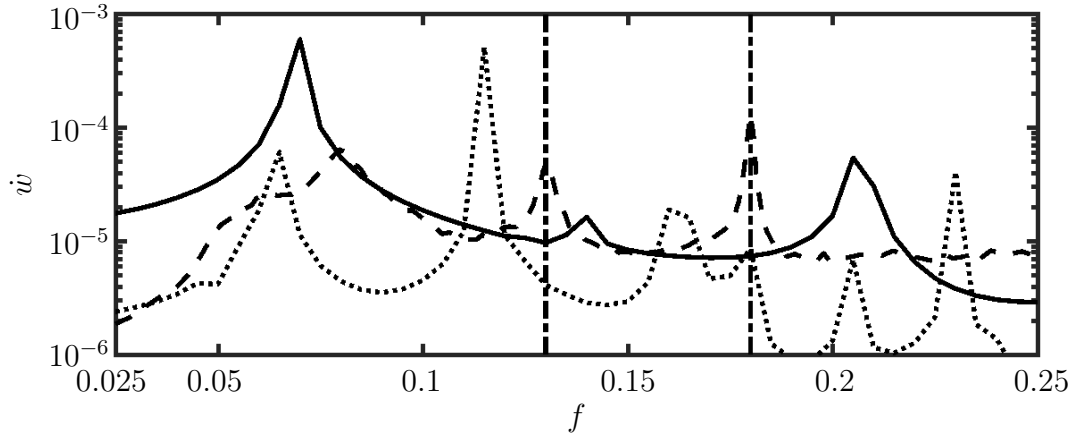

Figure 5.14: Comparison of frequency spectrum of the vibration velocity with viscous and inviscid flow. ——, numerical result with viscous flow; · · · · · ·, numerical result with inviscid flow; – – –, experimental data (Liu 2011). – · – · –, duct mode frequencies.

than the viscous solution. Besides, some unrealistic peaks are found in higher frequency in the inviscid solution, which cannot be agreed with the experimental data. The uniform profile in the inviscid calculation provided an approximation that seems close to the real velocity profile in the experiment, but the sharp change of velocity in the boundary layer cannot be captured. Since the fluid volume atop the panel will be deformed by the panel deflection, the viscous force in normal direction within the fluid should provides a counter force to the panel. This is a kind of fluid damping effect because the energy should be diffused by the viscosity. However, this force is absent in the inviscid flow solution. These viscous effects may play an important role in the flow-induced vibration problem that cannot be neglected.

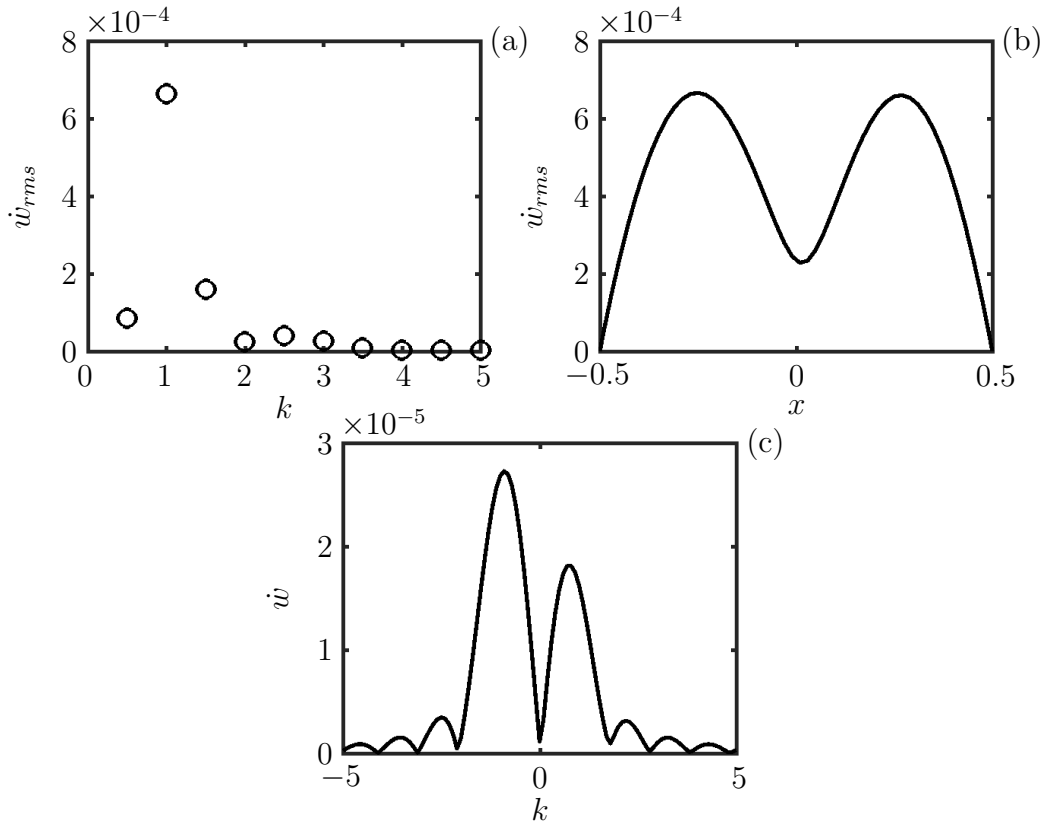

Figure 5.15: Panel spatial response. (a), the modal spectrum of panel velocity. (b), the distributions of panel velocity amplitude. (c), the wavenumber spectrum of panel velocity at $f = 0.07$.

5.2.3 Aeroacoustic-structural response

By the axial mode analysis, the modal spectrum of vibrating velocity and its spatial distribution is shown as Figure 5.15(a) and (b). It is found that the panel response is dominated by the second in-vacuo mode. The wavenumber spectrum of panel velocity at the dominate frequency $f = 0.07$ is also shown in Figure 5.15(c) to illustrate the upstream and downstream travelling panel waves. The wavenumbers of the upstream and downstream travelling waves are around -0.9 and 0.8 respectively, and the corresponding wave speeds are around -0.078 and 0.088 respectively. Besides, the amplitude of the upstream travelling wave is

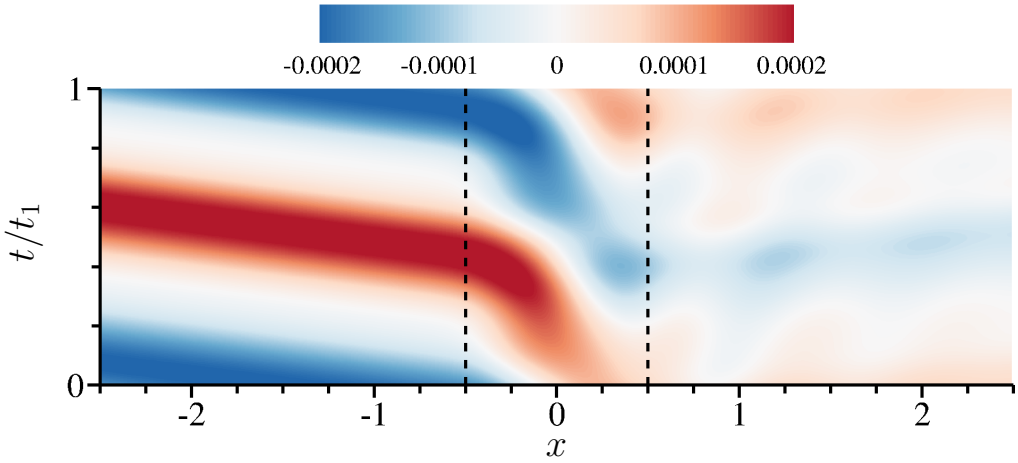

Figure 5.16: Pressure fluctuation along the duct centreline within one period of the dominate vibrating frequency, $t_1 = 1/f_0$.

150% of the downstream travelling wave.

The panel vibration then also re-radiates acoustic waves to upstream and downstream. The pressure fluctuation along the duct centreline within one period of the dominate vibrating frequency, $t_1 = 1/f_0 = 14.3$, is shown in Figure 5.16. The upstream radiation is a simple plane wave and it is much stronger than the downstream radiation. In the downstream, there are not pure acoustic wave propagation. Since the fluid on the flexible panel has to move up and down periodically together with the panel vibration, this motion of the fluid has the same frequency with the vibration and travels with the flow to the downstream. When the fluid impinge the lower wall and is forced to turn its direction from negative to positive y, for example at $x \approx 1.3$ in Figure 5.17(a), an high pressure zone is created as shown as same location in Figure 5.17(b). In opposite, a low pressure zone is created on the wall following the fluid motion of toward the wall, for example at $x \approx 1$. This pressure distribution together with the fluid motion is propagating with speed of flow. Combining with the acoustic wave, which propagates with speed of sound, the staggered pattern in the downstream

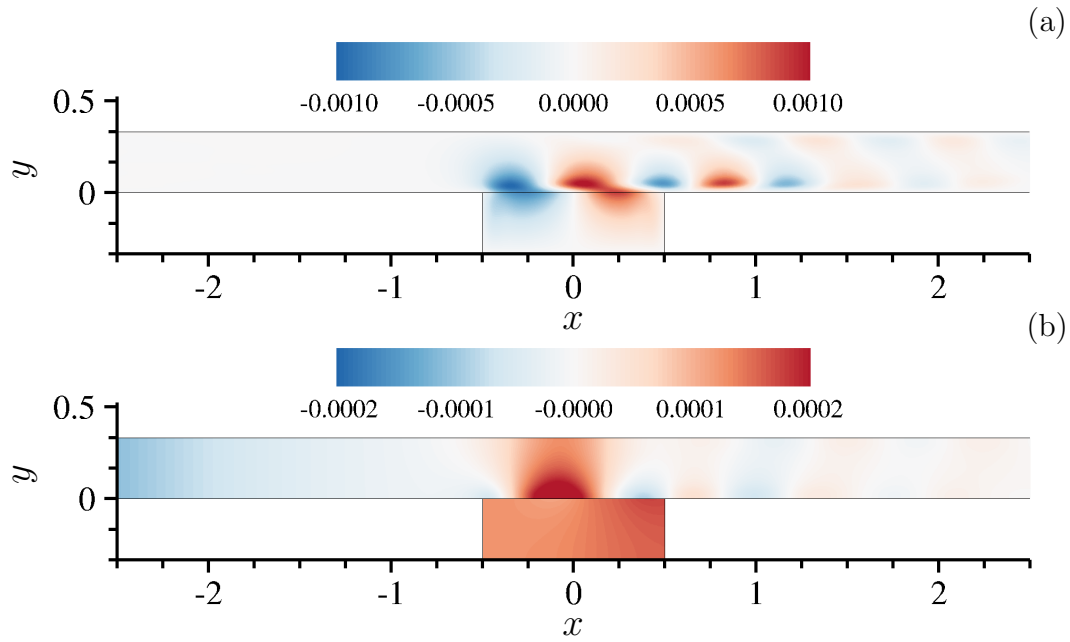

Figure 5.17: Snapshot at $t/t_1 = 0.2$. (a), velocity fluctuation in y-direction. (b), pressure fluctuation.

in Figure 5.16 is produced.

The power radiated by the panel can be determined as the acoustic intensity in x-direction (Rienstra and Hirchberg 2015),

$$I' = \frac{1}{H}\int_0^H \left(\bar{\rho}u' + \frac{p'\bar{u}}{c_0^2}\right)\left(\frac{p'}{\bar{\rho}} + \bar{u}u' + \bar{v}v'\right) dy, \tag{5.5}$$

where $\bar{\rho}$, $\bar{u}$ and $\bar{v}$ are the mean values of density and velocities in x- and y-directions respectively, p', u' and v' are the fluctuation of pressure and velocities in x- and y-directions respectively. The average acoustic intensities over a period t_1 in upstream and downstream are -4.4×10^{-9} (at $x = -2.5$) and 1.1×10^{-9} (at $x = 2.5$) respectively. The energy radiated to upstream is 5.9 db larger than the downstream. Total acoustic intensity radiated is 5.5×10^{-9}. The total intensity of the flow can be determined as (Rienstra and Hirchberg 2015)

$$I = \frac{1}{H}\int_0^H u\left(\rho E + p\right) dy. \tag{5.6}$$

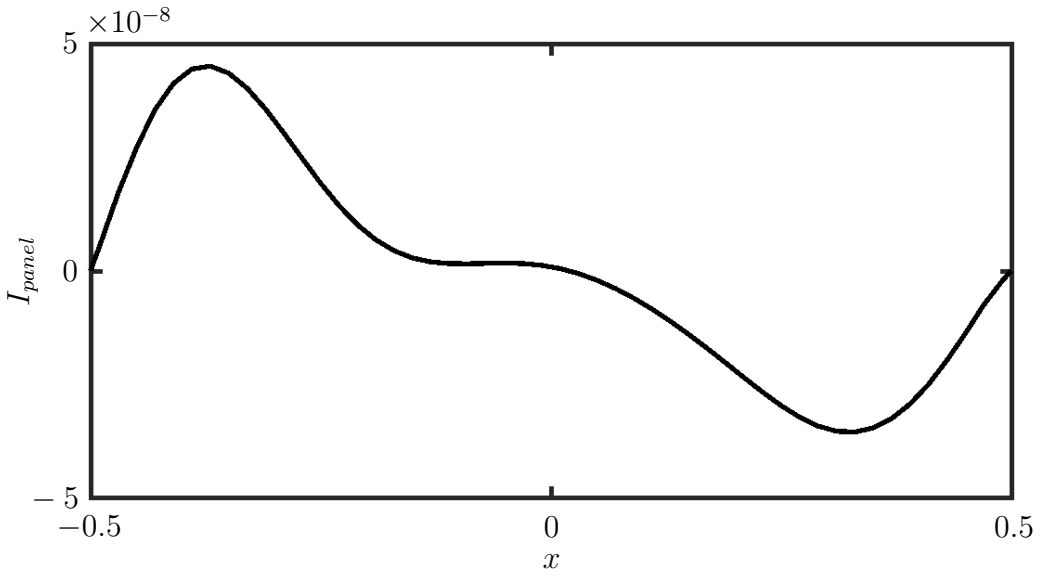

Figure 5.18: Distribution of average intensity of the panel over a period $t_1 = 1/f_0$.

and $I = 0.086$ in a fully rigid duct. Therefore $6.4 \times 10^{-6}\%$ of flow energy is converted to acoustic energy through the aeroacoustic-structural interaction. The distribution of average intensity of the panel over a period t_1 is shown in Figure 5.18, where the intensity of the panel $I_{panel} = -p_{ex}\dot{w}$. Over a period, the energy is radiated from the first half of the panel to the fluid since I_{panel} shows positive. On the contrary, another half of the panel is mainly absorbing energy from the fluid since I_{panel} shows negative. That may be the reason why the upstream radiation is much larger than the downstream.

When the cavity is removed, the aeroacoustic-structural response becomes another story. Figure 5.19 and 5.21 show the overviews of the panel response without cavity backed. Compared to the result with cavity in Figure 5.12, the growth of vibration amplitude is much slower as shown as Figure 5.19. It is because the initial pressure distribution is uniform in the cavity but non-uniform in the duct, there has an initial pressure difference that excites the panel with the

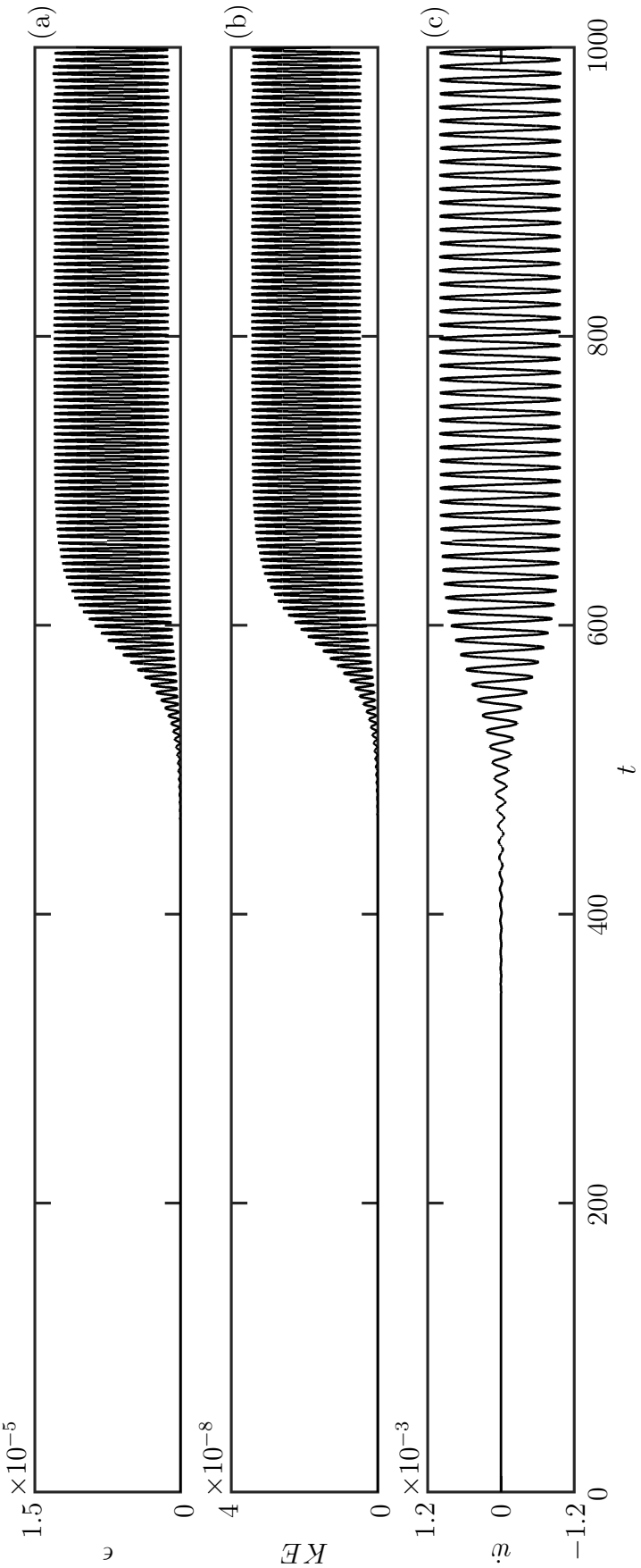

Figure 5.19: Time traces of panel response without cavity backed. (a), strain. (b), kinetic energy. (c), vibrating velocity at $x = 0$.

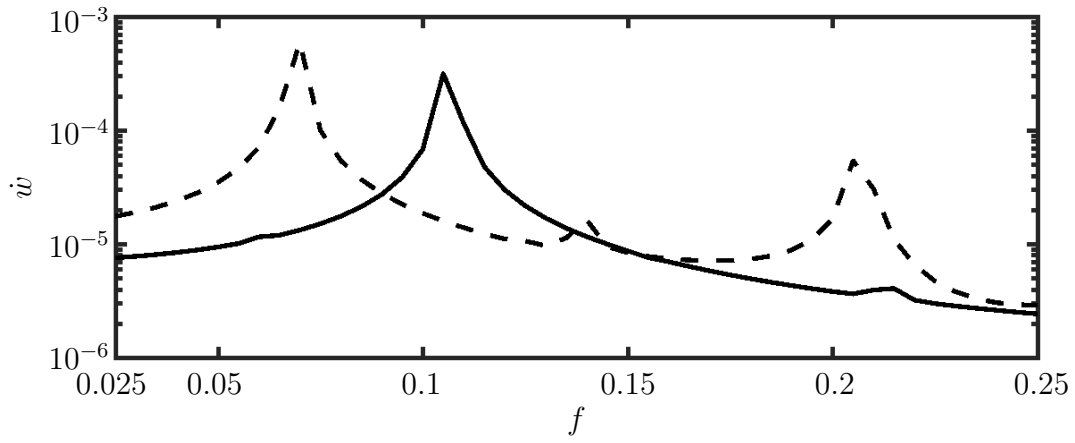

Figure 5.20: Averaged frequency spectrum of the vibration velocity. ——, without cavity backed. – – –, with cavity backed.

cavity at $t = 0$. On the other hand, there is no initial pressure difference in the case without cavity, so vibration is not strongly excited at $t = 0$. Nevertheless, both cases take more or less same duration of growth to time stationary state and become limit cycle oscillation. This represents the panel instability is independent of the cavity, and the growth of instability may also independent of the cavity or the initial pressure difference. The frequency spectra with and without cavity are compared in Figure 5.20. When there is no cavity, the response is dominated at $f = 0.105$. The dominant frequency is shifted 33% lower to $f_0 = 0.07$ that the panel is backed by the cavity. This shifting is related to the change of vibration modes. As Figure 5.21(a) and (b) show the panel vibration without cavity is dominated by the third in-vacuo mode. The dominant mode is reduced to the second mode when the cavity is used, that is directly proportional to the change of the dominant frequency. This change of mode is caused by the higher fluid inertia loading induced by the bounded fluid in the cavity. The volume of the cavity will be constant for even in-vacuo modes shape because half of the cavity is compressed by the deformed panel but half of it is expanded at the same time. However, it is either compressed or expanded for odd in-vacuo modes shape that induces

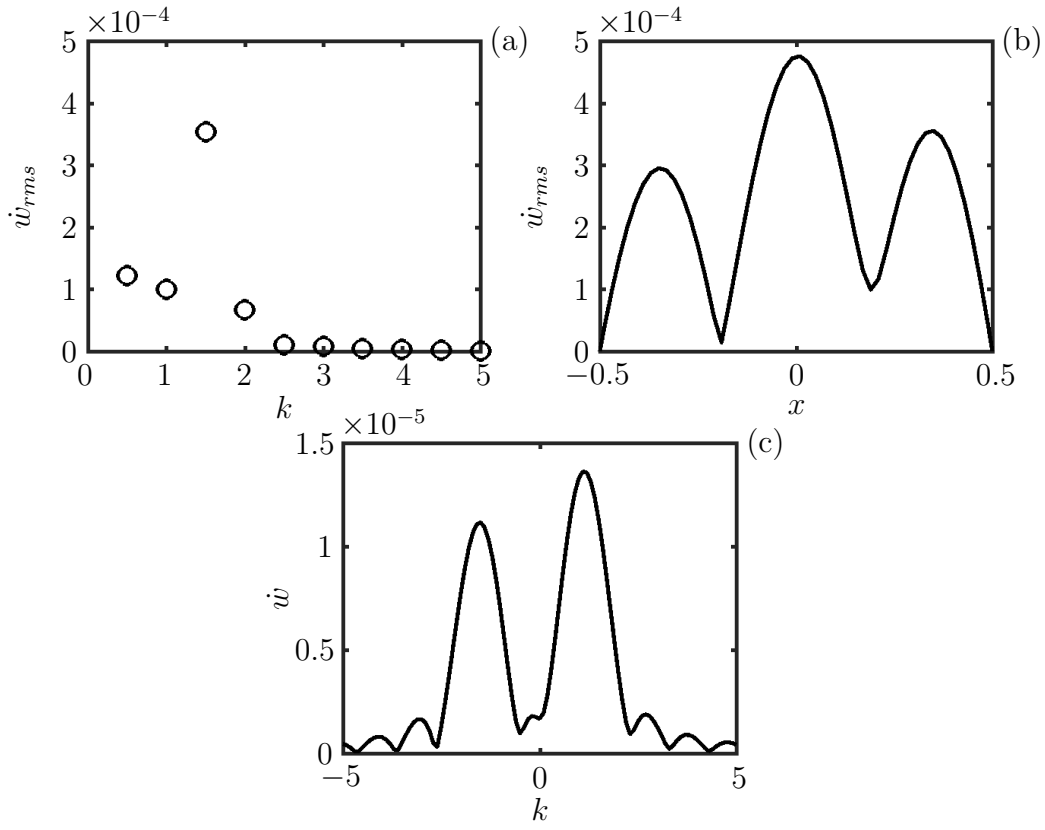

Figure 5.21: Panel spatial response without cavity backed. (a), the modal spectrum of panel velocity. (b), the distributions of panel velocity amplitude. (c), the wavenumber spectrum of panel velocity at $f = 0.105$.

pressure change and resistance to the panel motion. Even though spatial variation of modal amplitude is permitted, odd modes without a change of cavity volume should still not be accommodated. A mode with spatial variation of amplitudes is actually the superposition of more than one in-vacuo modes. For example, superposition of first and third in-vacuo modes may produce the amplitude of the centre is larger than the other two anti-nodes. Therefore the cavity volume can be unchanged if this mode sharp is maintained. However, different in-vacuo modes should vibrate with different frequencies based on the characteristic of the panel. The mode sharp cannot be maintained. Therefore the panel is hard to vibrate in odd modes and prefers in even modes when it is backed by the cavity. This is the reason why the vibration mode shifted from third to second. The upstream and downstream travelling panel waves at the dominate frequency $f_0 = 0.105$ are also illustrated in Figure 5.21(c). The wavenumbers of the upstream and downstream travelling waves are around -1.5 and 1.1 respectively, and the corresponding wave speeds are around -0.07 and 0.096 respectively. The upstream and downstream wave speeds are enhanced 11.4% and slowed down 8.3% respectively when the cavity is used. The effect of the cavity on the panel wave speed is opposite to the effect of flow which accelerates the downstream wave but decelerates the upstream wave. It is because the fluid in the cavity generates higher fluid inertia loading to the panel than the flowing fluid in the main duct. Therefore the effect of fluid inertia is changed. In addition, the amplitude of the upstream travelling wave is 82% of the downstream travelling wave which is totally unlike the behavior that with the cavity.

The aeroacoustic response is described in Figure 5.22, where the period $t_1 = 1/f_0 = 9.5$. The amplitudes of the waves in both directions are very close. Except this, the overall behaviour is similar to the case with the cavity. The acoustic intensities in upstream and downstream are -7.2×10^{-10} and 6.9×10^{-10}

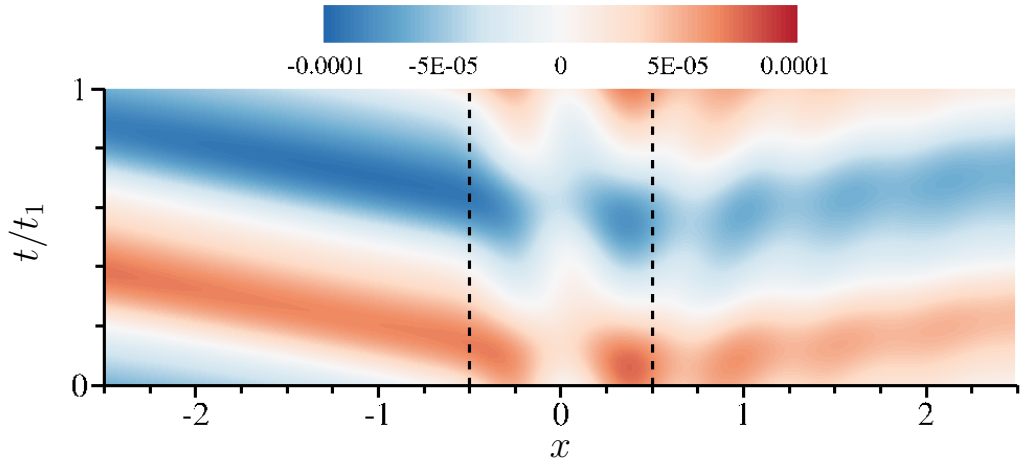

Figure 5.22: Pressure fluctuation along the duct centreline within one period of the dominate vibrating frequency, $t_1 = 1/f_0$.

respectively. The difference is much smaller than that with cavity, the energy radiated to upstream is only 0.18 db larger than the downstream. The total acoustic intensity is 1.4×10^{-9} that is $1.6 \times 10^{-6}\%$ of total flow intensity. It is 5.9 db less than that with cavity. The cavity enhanced the energy conversion from flow to acoustic and also prefers the upstream radiation. On the other hand, the distribution of average intensity of the panel over a period is also shown in Figure 5.23. Three peaks of radiation and two peaks of absorption are found. Both peaks of radiation and absorption near the trailing are larger than the others. The major difference to that with cavity is both leading and trailing edges are mainly radiating energy to fluid. Although the radiation near the trailing edge is lager than the leading edge, the absorption is also lager. Therefore it balanced the energy radiation to upstream and downstream and results in same level of intensity in two directions.

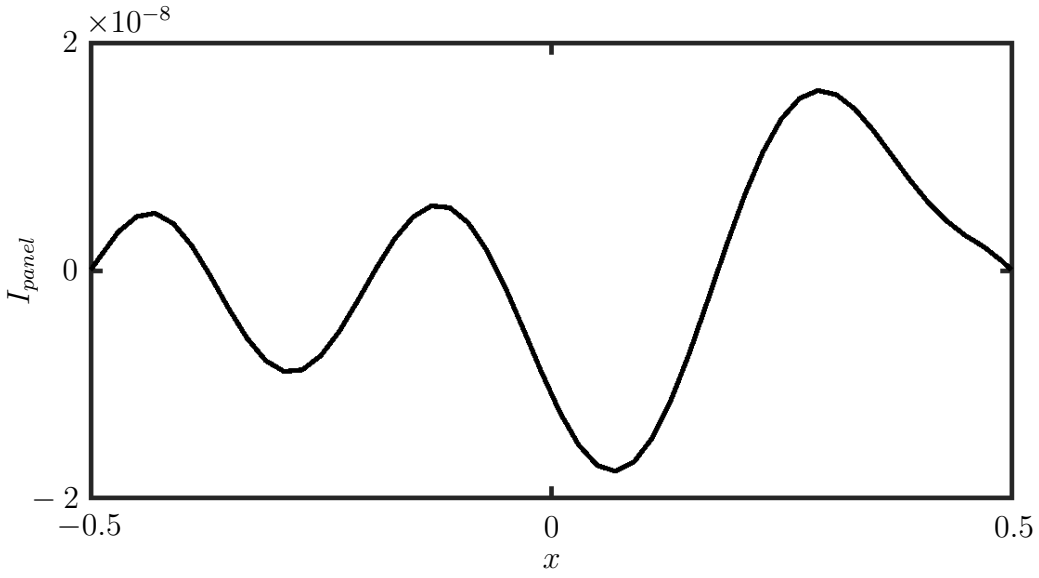

Figure 5.23: Distribution of average intensity of the panel over a period $t_1 = 1/f_0$.

Chapter 6

Conclusions

For the better understanding of aeroacoustic-structural interaction in the internal flow, the interaction with the inviscid and the viscous flow are investigated numerically. The numerical methodology by using partitioned approach is first introduced in Chapter 2. The aeroacoustics of the fluid and the dynamic response of the panel are modeled separately, and they communicate through a coupling strategy. The aeroacoustic model is governed by the two-dimensional compressible Navier-Stokes equations together with the ideal gas law. It is solved by the direct aeroacoustic simulation solver based on the conservation element and solution element method. On the other hand, the panel dynamic model is governed by the nonlinear one-dimension plate equation and solved by the standard finite-difference procedures. Two common coupling strategies, staggered and iterative coupling schemes, are tested and compared. In the staggered coupling scheme, aeroacoustics and panel dynamics are solved once and one by one in each time step in the time marching. The iterative coupling scheme solves the dynamics repeatedly in a time step to correct the error caused by the lagging of information from one solver to another. For the fluid loaded eigenmode vibration, two coupling schemes have similar results and agree well with the theory for zero mean flow.

In Chapter 3, the capabilities in capturing acoustic and structural responses of acoustic-induced structure vibration and their interaction are validated for both coupling schemes. By comparing with the theoretical solution of a duct silencer with damped and undamped flexible panel excited by single frequency incident acoustic wave, the iterative scheme has better agreement with the theory. Therefore the iterative scheme is employed for all subsequent inviscid fluid calculations. The results indicated the methodology is able to capture acoustic and structural responses accurately. The effect of flow and the aeroacoustic-structural responses are studied by introducing a uniform mean flow in the duct. The transmission loss TL is suppressed by the mean flow velocity M that TL is reverse proportional to M until sonic mean flow $M = 1$. Higher-order acoustic mode and multiple reflections of oblique shock waves emerge in supersonic flow. Besides, the bimodal pattern of panel response is observed and it indicates the panel response is combined by two types of bending waves, upstream and downstream travelling waves. The downstream travelling velocity and the amplitude of mobility appear to grow significantly with M as it aligns with the mean flow direction. Meanwhile, the upstream travelling wave slows down and weaken slightly with M. The result indicates that the linear theory cannot predict the bimodal bending wave pattern correctly when $M > 0.3$. The effect of fluid compressibility is a significant factor that triggers the bimodal pattern.

The structural and near field fluid responses with broadband excitation are also discussed. Subsonic and supersonic bending waves are observed in the structural response, but the supersonic mode emerges at high frequency only. The effect of mean flow increases the downstream travelling speed but reduces the upstream one to both subsonic and supersonic modes, and their variation with frequency is not linear. In addition, low TL are accompanied with the bending waves that travelling in near sonic speed, whether subsonic or supersonic

modes. It implies that near sonic bending waves is beneficial the transmission of the incident acoustic wave since the difference of their phase speeds is small. In the duct section above the flexible panel, almost only supersonic wave can be observed. The characteristics of near field response is consistent with the structural response. It can be deduced that none of incident waves can transmit to the downstream directly with acoustic speed in free field. The acoustic waves are transformed as the subsonic surface waves and the leaky waves though the aeroacoustic-structural interaction, and redistributed to upstream and downstream. In addition, another possibility is a portion of incident acoustic waves are reflected directly at the panels leading edge.

The effect of fluid viscosity on the aeroacoustic-structural interaction is further studied. However, the partitioned approach is powerless to handle the problem with viscous flow. It is because of the incorrect estimation of the viscous effect during the communication between the aeroacoustics and structural dynamics. Therefore another methodology based on monolithic approach is introduced in Chapter 4. The governing equations describing both aeroacoustics, structural dynamics and their interaction is derived and solved by Newton's method. This approach allows complete information interchange between aeroacoustics and structural dynamics since they are inherently coupled in the governing equations. It is compared with the partitioned approach in the benchmarks cases reported in Chapter 3. The monolithic approach has higher accuracy and double time efficiency than the partitioned approach.

The numerical methodology by monolithic approach is also validated its capability in capturing the aeroacoustic-structural interaction in viscous flow by studying two problems based on experimental studies in Chapter 5. The capability of capturing aeroacoustic and panel responses induced by acoustic excitation is firstly validated with the experiment of a drum-like silencer carrying a low

Mach number flow. The result has an excellent agreement with the experimental data which firmly confirm the capability of the methodology. The result also indicates that the inclusion of the viscous effect can provide a more accurate solution for the aeroacoustic-structural response. The effect of cavities which backing the flexible panel is further investigated. For the structural response, the cavities amplify the upstream travelling wave but attenuate the downstream one at low frequency. For the acoustic response, the cavities enhance the TL at low frequency and change the effective silencing frequency range.

In the second problem, the capability of the methodology in capturing the instability of flexible panel induced by flow is examined. Favourable agreement with the experimental data is obtained, that validate the nonlinear interaction between flow and panel can be truly resolved by the methodology. The result indicates that the viscous effect is significantly important in this case, the inviscid assumption is totally invalid. That is consistent with the result in the previous problem. In addition, the result shows the occurrence of panel instability is independent of the cavity. The role of the cavity is to reduce the vibration frequency due to higher fluid inertia loading and change the vibration mode from third to second in-vacuo mode. This change also enhances the energy conversion from flow to acoustics and causes the acoustic wave is re-radiated to upstream mainly. Both viscous problems show the importance of involving the fluid viscosity which provides more accurate results, and the backing cavity directly impacts the aeroacoustic-structural response.

6.1 Limitations and future works

The thesis introduced the numerical methodologies that validated can accurately resolve the aeroacoustic-structural interaction problem. However, they still have some limitations have to improve or extend. First of all, the convective terms for

the sliding flexible wall condition are ignored that make the model only able to fully resolve the interaction with low flow speed. The effect of flow curvature on the wall dynamics are effectively absent. When the flow speed is high, such effect can be strong and transfer mean-flow kinetic energy to the flexible panel to create instability, such as divergence and Kelvin-Helmholtz instability (Carpenter and Garrad 1986). In the further study of the inviscid flow problem, the convective terms must be included in the boundary condition to capture the complete picture of the fluid-structure interaction.

Another limitation is the flexible panel deformation cannot larger than the distance between the undeformed panel surface and the layer of the nearest solution points in the fluid domain. This is because the fluid and the panel is deformed simultaneously, but we do not apply a proper approach to account large deformation of the fluid, such as mesh deformation. Based on the present approach, the aeroacoustic-structural interaction is directly solved at the solution points on the fluid-panel interface. The effect of the panel displacement is weakly accounted which reflected on the calculation of spatial gradient which is based on the distance between a solution point to the interface. If the deformation is larger than the limitation, the fluid solution point should not physically exist at this moment. Its role will become a virtual solution point that applies the effect of the aeroacoustic-structural interaction to the fluid domain through linear projection. However the effect of large deformation is definitely nonlinear, so the present method will induce significant error and produce an incorrect result. Therefore we have to develop a proper approach to account the fluid deformation for any further study on the aeroacoustic-structural interaction problem with large deformation.

In addition, the two-dimensional assumption also is a limitation. For some real applications, the three-dimensional effect may be strong such as in turbulent flow. Besides in a duct with narrow spanwise spacing, the boundary

effect in spanwise direction will be large so the two-dimensional assumption is not applicable in this situation. Therefore the development of three-dimensional calculation is necessary for better understanding of the aeroacoustic-structural interaction in these situations.

On the other hand, some phenomenon and mechanisms of aeroacoustic-structural interaction of flexible panels in internal flow are not completely understood yet. Further studies on different aspects have to be carried on. First, the character of near field fluid response is found that consistent with the panel response which travelling with speed different to the speed of sound in far field. Nevertheless, the mechanism of transformation from these responses, involve surface wave and leaky wave, to acoustic wave is still a question. Second, the study on the aeroacoustic-structural response with acoustic excitation is based on fixed panel material properties or size of the cavity. The effect of these parameters is not cleared yet. On the analysis of the flow-induced structural instability, the effect of panel material properties and the duct width on the onset of flutter and it aeroacoustic response are not studied. For a complete understanding, the parametric studies on panel material properties, sizes of duct and cavity should be carried out in future. Finally, all the reported cases focus on a single panel or one flexible duct segment. However, the structure constructed by a series of flexible panel is often found in real applications. The study of the effect from one to a neighboring panel is also a possible extension of the present study.

There are many research extensions can be performed for many practical engineering problems. Pinned and clamped end conditions for the flexible panel are presented in the thesis. However, the free end condition can be further developed for studying the cantilever structures such as for snoring problem, vibration of wings or blades, and energy harvesting application. Besides, an elastic structure model for thick structure can be developed. More problems,

such as vibration of bridge in civil engineering, can be resolved by the present fluid-structure coupling methodology.

References

Abrahams, I. D. (1983), "Scattering of Sound by an Elastic Plate with Flow," *Journal of Sound and Vibration*, Vol. 89, No. 2, pp. 213–231.

Abrahams, I. D. and Wickham, G. R. (2001), "On Transient Oscillations of Plates in Moving Fluids," *Wave Motion*, Vol. 33, No. 1, pp. 7–23.

Aginsky, Z. and Gottlieb, O. (2012), "Nonlinear Bifurcation Structure of Panels Subject to Periodic Acoustic Fluid-Structure Interaction," *AIAA Journal*, Vol. 50, No. 9, pp. 1979–1992.

Aginsky, Z. and Gottlieb, O. (2013), "Nonlinear Fluid-Structure Interaction of an Elastic Panel in an Acoustically Excited Two-Dimensional Inviscid Compressible Fluid," *Physics of Fluids*, Vol. 25, No. 7, pp. 076104–1–35.

Anderson, D. A., Tannehill, J. C., and Pletcher, R. H. (1984), *Computational Fluid Mechanics and Heat Transfer*. McGraw-Hill, New York, 2nd ed., pp. 156–157.

Anderson, J. D. (2011), *Fundamentals of Aerodynamics*. McGraw-Hill, New York, 5th ed., pp. 131, 146, 903–915.

Arzoumanian, S. (2011), *Stability of Fluid-Loaded Structures*, Ph.D. thesis, University of Cambridge, pp. 1–3.

Benjamin, T. B. (1960), "Effects of a Flexible Boundary on Hydrodynamic Stability," *Journal of Fluid Mechanics*, Vol. 9, No. 04, pp. 513–532.

Benjamin, T. B. (1963), "The Threefold Classification of Unstable Disturbances in Flexible Surfaces Bounding Inviscid Flows," *Journal of Fluid Mechanics*, Vol. 16, No. 3, pp. 436–450.

Beranek, L. L. (1993), *Acoustics*. Acoustical Society of America, New York, p. 133.

Blevins, R. D. (1979), *Formulas for Natural Frequency and Mode Shape*. Van Nostrand Reinhold Company, New York, Cincinnati, Atlanta, Dallas, San Francisco, London, Toronto, Melbourne, pp. 252–261.

Brazier-Smith, P. and Scott, J. (1984), "Stability of Fluid Flow in the Presence of a Compliant Surface," *Wave Motion*, Vol. 6, pp. 547–560.

Carpenter, P. W. and Garrad, A. D. (1986), "The Hydrodynamic Stability of Flow over Kramer-Type Compliant Surfaces. Part 2. Flow-Induced Surface Instabilities," *Journal of Fluid Mechanics*, Vol. 170, pp. 199–232.

Chang, S. C. (1995), "The Method of Space-Time Conservation Element and Solution Element–A New Approach for Solving the Navier-Stokes and Euler Equations," *Journal of computational physics*, Vol. 119, pp. 295–324.

Choi, S. and Kim, Y.-H. (2002), "Sound-Wave Propagation in a Membrane-Duct," *The Journal of the Acoustical Society of America*, Vol. 112, No. 5, pp. 1749–1752.

Choy, Y. S. and Huang, L. (2005), "Effect of Flow on the Drumlike Silencer," *The Journal of the Acoustical Society of America*, Vol. 118, No. 5, pp. 3077–3085.

Cisonni, J., Lucey, A. D., Elliott, N. S. J., and Heil, M. (2017), "The Stability of a Flexible Cantilever in Viscous Channel Flow," *Journal of Sound and Vibration*, Vol. 396, pp. 186–202.

Clark, R. L. and Frampton, K. D. (1997), "Aeroelastic Structural Acoustic Coupling: Implications on the Control of Turbulent Boundary-Layer Noise Transmission," *The Journal of the Acoustical Society of America*, Vol. 102, No. 3, pp. 1639–1647.

Crighton, D. G. (1981), "Acoustics as a Branch of Fluid Mechanics," *Journal of Fluid Mechanics*, Vol. 106, pp. 261–298.

Crighton, D. G. (1984), "Transmission of Energy Down Periodically Ribbed Elastic Structures under Fluid Loading," *Proceedings of the Royal Society A: Mathematical, Physical and Engineering Sciences*, Vol. 394, pp. 405–436.

Crighton, D. G. (1989), "The 1988 Rayleigh Medal Lecture: Fluid Loading – The Interaction between Sound and Vibration," *Journal of Sound and Vibration*, Vol. 133, No. 1, pp. 1–27.

Crighton, D. G. and Oswell, J. E. (1991), "Fluid Loading with Mean Flow. I. Response of an Elastic Plate to Localized Excitation," *Philosophical Transactions of the Royal Society A: Mathematical, Physical and Engineering Sciences*, Vol. 335, No. 1639, pp. 557–592.

Cummings, A. (2001), "Sound Transmission through Duct Walls," *Journal of Sound and Vibration*, Vol. 239, No. 4, pp. 731–765.

Davies, C. and Carpenter, P. W. (1997a), "Instabilities in a Plane Channel Flow between Compliant Walls," *Journal of Fluid Mechanics*, Vol. 352, pp. 205–243.

Davies, C. and Carpenter, P. W. (1997b), "Numerical Simulation of the Evolution

of Tollmien-Schlichting Waves over Finite Compliant Panels," *Journal of Fluid Mechanics*, Vol. 335, pp. 361–392.

de' Michieli Vitturi, M., Esposti Ongaro, T., Neri, A., Salvetti, M. V., and Beux, F. (2007), "An Immersed Boundary Method for Compressible Multiphase Flows: Application to the Dynamics of Pyroclastic Density Currents," *Computational Geosciences*, Vol. 11, No. 3, pp. 183–198.

Djojodihardjo, H. (2008), "Unified BE-FE Aerodynamic-Acoustic-Structure Coupling Scheme for Acoustic," *Proceedings of the 26th International Congress of the Aeronautical Sciences*, pp. 1–19.

Djojodihardjo, H. (2015), "Vibro-Acoustic Analysis of the Acoustic-Structure Interaction of Flexible Structure due to Acoustic Excitation," *Acta Astronautica*, Vol. 108, pp. 129–145.

Doak, P. E. (1973), "Excitation, Transmission and Radiation of Sound from Source Distributions in Hard-Walled Ducts of Finite Length (I): The Effects of Duct Cross-Section Geometry and Source Distribution Space-Time Pattern," *Journal of Sound and Vibration*, Vol. 31, No. 1, pp. 1–72.

Dowell, E. H. (1970), "Panel Flutter: A Review of the Aeroelastic Stability of Plates and Shells," *AIAA Journal*, Vol. 8, No. 3, pp. 385–399.

Dowell, E. H. (1975), *Aeroelasticity of Plates and Shells*. Noordhoff International Publishing, Leyden, pp. 35–38.

Dowell, E. H. and Hall, K. C. (2001), "Modeling of Fluid-Structure Interaction," *Annual Review of Fluid Mechanics*, Vol. 33, No. 1, pp. 445–490.

Dowling, A. P. and Ffowcs Williams, J. E. (1983), *Sound and Sources of Sound*. Ellis Horwood Limited, Chichester, p. 134.

Dugundji, J., Dowell, E. H., and Perkin, B. (1963), "Subsonic Flutter of Panels on Continuous Elastic Foundations," *AIAA Journal*, Vol. 1, No. 5, pp. 1146–1154.

Fahy, F. and Gardonio, P. (2007), *Sound and Structural Vibration: Radiation, Transmission and Response*. Elsevier, Amsterdam, Boston, Heidelberg, London, New York, Oxford, Paris, San Diego, San Francisco, Singapore, Sydney, Tokyo, pp. 1–2.

Felippa, C., Park, K., and Farhat, C. (2001), "Partitioned Analysis of Coupled Mechanical Systems," *Computer Methods in Applied Mechanics and Engineering*, Vol. 190, pp. 3247–3270.

Ffowcs Williams, J. E. and Hill, D. C. (1987), "On the Scattering of Evanescent Waves into Sound," *Journal of Fluid Mechanics*, Vol. 184, pp. 101–121.

Frendi, A., Maestrello, L., and Ting, L. (1995), "An Efficient Model for Coupling Structural Vibrations with Acoustic Radiation," *Journal of Sound and Vibration*, Vol. 182, pp. 741–757.

Gaster, M. (1987), "Is the Dolphin a Red Herring?" *Turbulence Managment and Relaminarisation: Proceedings of the IUTAM Symposium, Bangalore, India, 1987*, edited by Liepmann, H. W. and Narasimha, R., Vol. 1, Springer-Verlag, Berlin, Heidelberg, New York, London, Paris, Tokyo, pp. 285–304.

Greenshields, C. J. and Weller, H. G. (2005), "A Unified Formulation for Continuum Mechanics Applied to Fluid-Structure Interaction in Flexible Tubes," *International Journal for Numerical Methods in Engineering*, Vol. 64, No. 12, pp. 1575–1593.

Hamdan, F. H. and Dowling, P. J. (1995), "Fluid-Structure Interaction: Application to Structures in an Acoustic Fluid Medium, Part 1: An Introduction to Numerical Treatment," *Engineering Computations*, Vol. 12, pp. 749–758.

Hayek, S. I. (2011), *Advanced Mathematical Methods in Science and Engineering*. CRC Press, Boca Raton, London, New York, 2nd ed., pp. 599–600.

Heil, M. (2004), "An Efficient Solver for the Fully Coupled Solution of Large-Displacement FluidStructure Interaction Problems," *Computer Methods in Applied Mechanics and Engineering*, Vol. 193, pp. 1–23.

Heil, M. and Hazel, A. L. (2011), "Fluid-Structure Interaction in Internal Physiological Flows," *Annual Review of Fluid Mechanics*, Vol. 43, pp. 141–162.

Herrmann, J., Junge, M., and Gaul, L. (2012), "Vibroacoustic Response of Flexible Car Components," *Computer Modeling in Engineering & Sciences*, Vol. 86, No. 6, pp. 487–504.

Howell, R. M. and Lucey, A. D. (2012), "The Fluid-Structure Interaction of a Spring-Mounted Cantilevered-Free Flexible Plate in a Uniform Flow," *Proceedings of the 10th International conference on Flow-Induced Vibration (& Flow-Induce Noise)*, edited by Meskell, C. and Bennett, G., Dublin, pp. 219–226.

Huang, L. (1999), "A Theoretical Study of Duct Noise Control by Flexible Panels," *The Journal of the Acoustical Society of America*, Vol. 106, No. 4, pp. 1801–1809.

Huang, L. (2001a), "A Theoretical Study of Passive Control of Duct Noise Using Panels of Varying Compliance," *The Journal of the Acoustical Society of America*, Vol. 109, No. 6, pp. 2805–2814.

Huang, L. (2001b), "Viscous Flutter of a Finite Elastic Membrane in Poiseuille Flow," *Journal of Fluids and Structures*, Vol. 15, pp. 1061–1088.

Huang, L., Quinn, S. J., Ellis, P. D., and Ffowcs Williams, J. E. (1995), "Biomechanics of Snoring," *Endeavour*, Vol. 19, No. 3, pp. 96–100.

Huang, L. and Zhang, C. (2013), "Modal Analysis of Cantilever Plate Flutter," *Journal of Fluids and Structures*, Vol. 38, pp. 273–289.

Huang, X. Y. (1987), "Active Control of Aerofoil Flutter," *AIAA Journal*, Vol. 25, No. 8, pp. 1126–1132.

Ishihara, D. and Yoshimura, S. (2005), "A Monolithic Approach for Interaction of Incompressible Viscous Fluid and an Elastic Body Based on Fluid Pressure Poisson Equation," *International Journal for Numerical Methods in Engineering*, Vol. 64, No. 2, pp. 167–203.

Jadic, I., So, R. M. C., and Mignolet, M. P. (1998), "Analysis of Fluid-Structure Interactions Using a Time-Marching Technique," *Journal of Fluids and Structures*, Vol. 12, No. 6, pp. 631–654.

Jaiman, R., Geubelle, P., Loth, E., and Jiao, X. (2011), "Combined Interface Boundary Condition Method for Unsteady Fluid-Structure Interaction," *Computer Methods in Applied Mechanics and Engineering*, Vol. 200, pp. 27–39.

John, J. E. and Keith, T. G. (2006), *Gas Dynamics*. Pearson Prentice Hall, Upper Saddle River, New Jersey, 3rd ed., pp. 189–228.

Kamakoti, R. and Shyy, W. (2004), "Fluid-Structure Interaction for Aeroelastic Applications," *Progress in Aerospace Sciences*, Vol. 40, No. 8, pp. 535–558.

Ko, S. H. (1994), "Sound Wave Propagation in a Two-Dimensional Flexible Duct in the Presence of an Inviscid Flow," *Journal of Sound and Vibration*, Vol. 175, No. 2, pp. 279–287.

Korobkin, A., Pru, E. I., and Vanden-Broeck, J.-M. (2011), "The Mathematical Challenges and Modelling of Hydroelasticity," *Philosophical transactions. Series A, Mathematical, physical, and engineering sciences*, Vol. 369, No. 1947, pp. 2803–2812.

Lam, G. C. Y. (2011), *Aeroacoustics of Merging Flows at Duct Junctions*, Ph.D. thesis, The Hong Kong Polytechnic University, pp. 14–28, 39–43.

Lam, G. C. Y., Leung, R. C. K., Seid, K. H., and Tang, S. K. (2014a), "Validation of CE/SE Scheme for Low Mach Number Direct Aeroacoustic Simulation," *International Journal of Nonlinear Sciences and Numerical Simulation*, Vol. 15, No. 2, pp. 157–169.

Lam, G. C. Y., Leung, R. C. K., and Tang, S. K. (2013), "Aeroacoustics of T-Junction Merging Flow," *Journal of the Acoustical Society of America*, Vol. 133, No. 2, pp. 697–708.

Lam, G. C. Y., Leung, R. C. K., and Tang, S. K. (2014b), "Aeroacoustics of Duct Junction Flows Merging at Different Angles," *Journal of Sound and Vibration*, Vol. 333, pp. 4187–4202.

Landahl, M. T. (1962), "On the Stability of a Laminar Incompressible Boundary Layer over a Flexible Surface," *Journal of Fluid Mechanics*, Vol. 13, No. 4, pp. 609–632.

Leung, R. C. K., So, R. M. C., Wang, M. H., and Li, X. M. (2007), "In-Duct Orifice and Its Effect on Sound Absorption," *Journal of Sound and Vibration*, Vol. 299, pp. 990–1004.

Li, K. H. (2015), *Silencing Performance and Aeroacoustic-Structural Responses of Flexible Panel Silencer*, Master's thesis, The Hong Kong Polytechnic University, pp. 41–61.

Liu, Y. (2011), *Flow Induced Vibraion and Noise Control with Flow*, Ph.D. thesis, The Hong Kong Polytechnic University, pp. 62–77.

Loh, C. Y. (2005), "Computation of Tone Noise from Supersonic Jet Impinging on Flat Plates," NASA/CR–2005-213426, AIAA-2005-0418.

Lucey, A. D. (1998), "The Excitation of Waves on a Flexible Panel in a Uniform Flow," *Philosophical Transactions of the Royal Society A: Mathematical, Physical and Engineering Sciences*, Vol. 356, No. 1749, pp. 2999–3039.

Lucey, A. D., Cafolla, G. J., Carpenter, P. W., and Yang, M. (1997), "The Nonlinear Hydroelastic Behaviour of Flexible Walls," *Journal of Fluids and Structures*, Vol. 11, No. 7, pp. 717–744.

Lucey, A. D. and Carpenter, P. W. (1992), "A Numerical Simulation of the Interaction of a Compliant Wall and Inviscid Flow," *Journal of Fluid Mechanics*, Vol. 234, pp. 121– 146.

Luo, X. Y. and Pedley, T. J. (1998), "The Effects of Wall Inertia on Flow in a Two-Dimensional Collapsible Channel," *Journal of Fluid Mechanics*, Vol. 363, pp. 253–280.

Maestrello, L., Frendi, A., and Brown, D. E. (1992), "Nonlinear Vibration and Radiation from a Panel with Transition to Chaos," *AIAA Journal*, Vol. 30, No. 11, pp. 2632–2638.

Maestrello, L. and Grosveld, F. W. (1992), "Transition Control of Instability Waves over an Acoustically Excited Flexible Surface," *AIAA Journal*, Vol. 30, No. 3, pp. 665–670.

Maidanik, G. and Kerwin, E. M. (1966), "Influence of Fluid Loading on the Radiation from Infinite Plates below the Critical Frequency," *The Journal of the Acoustical Society of America*, Vol. 40, No. 5, pp. 1034–1038.

Nagai, K., Toshimitsu, K., and Namba, M. (1996), "Active Control of Cascade Flutter by Means of Sound Waves from Duct Wall Sources," *JSME International Journal Series B Fluids and Thermal Engineering*, Vol. 39, No. 3, pp. 608–614.

Paidoussis, M. P. (2004), *Fluid-Structure Interactions: Slender Structures and Axial Flow, Volume 2*. Elsevier, Amsterdam, Boston, Heidelberg, London, New York, Oxford, Paris, San Diego, San Francisco, Singapore, Sydney, Tokyo, p. 1137.

Peake, N. (2004), "On the Unsteady Motion of a Long Fluid-Loaded Elastic Plate with Mean Flow," *Journal of Fluid Mechanics*, Vol. 507, pp. 335–366.

Pitman, M. W. and Lucey, A. D. (2009), "On the Direct Determination of the Eigenmodes of Finite Flow-Structure Systems," *Proceedings of the Royal Society A: Mathematical, Physical and Engineering Sciences*, Vol. 465, pp. 257–281.

Rao, J. S. (1999), *Dynamics of Plates*. Narosa Publishing House, New Delhi, p. 227.

Rienstra, S. W. and Hirchberg, A. (2015), *An Introduction to Acoustics*. Eindhoven University of Technology, Eindhoven, pp. 29–32.

Rugonyi, S. and Bathe, K.-J. (2000), "On the Analysis of Fully Coupled Fluid Flows with Structural Interactions: A Coupling and Condensation Procedure," *International Journal for Computational Civil and Structural Engineering*, Vol. 1, pp. 29–41.

Rugonyi, S. and Bathe, K.-J. (2001), "On Finite Element Analysis of Fluid Flows Fully Coupled with Structural Interactions," *Computer Modeling in Engineering & Sciences*, Vol. 2, No. 2, pp. 195–212.

Schäfer, F., Müller, S., Uffinger, T., Becker, S., Grabinger, J., and Kaltenbacher, M. (2010), "Fluid-Structure-Acoustic Interaction of the Flow Past a Thin Flexible Structure," *AIAA Journal*, Vol. 48, No. 4, pp. 738–748.

Shankar, V. (2015), "Stability of Fluid Flow through Deformable Tubes and Channels: An Overview," *Sādhanā*, Vol. 40, pp. 925–943.

So, R. M. C., Liu, Y., and Lai, Y. G. (2003), "Mesh Shape Preservation for Flow-Induced Vibration Problems," *Journal of Fluids and Structures*, Vol. 18, pp. 287–304.

Stewart, P. S., Heil, M., Waters, S. L., and Jensen, O. E. (2010), "Sloshing and Slamming Oscillations in Collapsible Channel Flow," *Journal of Fluid Mechanics*, Vol. 662, pp. 288–319.

Sucheendran, M. M., Bodony, D. J., and Geubelle, P. H. (2014), "Coupled Structural-Acoustic Response of a Duct-Mounted Elastic Plate with Grazing Flow," *AIAA Journal*, Vol. 52, No. 1, pp. 178–194.

Szilard, R. (2004), *Theories and Applications of Plate Analysis: Classical, Numerical and Engineering Methods*. John Wiley & Sons, Inc., Hoboken, New Jersey, pp. 5–6, 614–617.

Tang, L., Païdoussis, M. P., and Jiang, J. (2009), "Cantilevered Flexible Plates in Axial Flow: Energy Transfer and the Concept of Flutter-Mill," *Journal of Sound and Vibration*, Vol. 326, pp. 263–276.

Tang, S. K., Leung, R. C. K., and So, R. M. C. (2007), "Vortex Sound due to a Flexible Boundary Backed by a Cavity in a Low Mach Number Mean Flow," *The Journal of the Acoustical Society of America*, Vol. 121, No. 3, pp. 1345–1352.

Visbal, M. R. and Gordnier, R. E. (2004), "Numerical Simulation of the Interaction of a Transitional Boundary Layer with a 2-D Flexible Panel in the Subsonic Regime," *Journal of Fluids and Structures*, Vol. 19, pp. 881–903.

White, F. M. (1998), *Fluid Mechanics*. McGraw-Hill, Boston, Burr Ridge, IL, Dubuque, IA, Madison, WI, New York, San Francisco, St. Louis, Bangkok,

Bogotá, Caracas, Lisbon, London, Madrid, Mexico City, Milan, New Delhi, Seoul, Singapore, Sydney, Taipei, Toronto, 4th ed., p. 572.